SAPIENZA
UNIVERSITÀ DI ROMA

Faculty of Civil and Industrial Engineering

Department of Civil, Constructional and Environmental Engineering
PhD in Environmental and Hydraulic Engineering

Thesis For The Degree Of Doctor Of Philosophy

Turbulence models under breaking waves: a new two-equation model based on turbulent kinetic energy and specific dissipation rate

Thesis Advisors
Prof. Giovanni Cannata
Prof. Francesco Gallerano

Candidate
Benedetta Iele
1600611

Academic Years MMXIX-MMXXII (XXXV cycle)

This PhD thesis written in LaTeXby Benedetta Iele (Rome, 31^{st} January 2023)

Ὅμοιον εἶναι τῇ ἄκρᾳ, ᾗ διηνεκῶς τὰ κύματα προσρήσσεται· ἡ δὲ ἔστηκε καὶ περὶ αὐτὴν κοιμίζεται τὰ φλεγμήναντα τοῦ ὕδατος.

Be like the cliff against which the waves continually break; but it stands firm and tames the fury of the water around it.

(Marco Aurelio)

To my Family

Abstract

In this thesis, a new model for the simulation of the breaking waves is proposed. This model is based on the solution of the three-dimensional equations of motion expressed in contravariant formulation. These equations are in integral form and are expressed in terms of the conserved variables H and $H\vec{u}$ (H is the total water depth and $\vec{u}$ is fluid velocity vector).

The three-dimensional ensemble-averaged motion equations are solved by a new high-order shock-capturing numerical scheme. The elements of novelty in this new numerical scheme are two. The first element of novelty consists in the proposal of a new reconstruction technique of the point values of the conserved variables on the cell faces of the computational grid (starting from the cell-averaged values of the same variables). This reconstruction technique is named Wave-Targeted Essentially Non-Oscillatory (WTENO) and it is specifically designed for the three-dimensional simulation of breaking waves. The second element of novelty consists in the use of an exact solution for the Riemann problem to advancing in time the point values of the conserved variables at the cell faces.

In this thesis, two turbulence models, which belong to the context of the Unsteady Reynolds-Averaged Navier-Stokes Equations (URANS) models, $k-l$ and $k-\omega$ (k is the turbulent kinetic energy, l is the mixing length and ω is the specific dissipation rate) are proposed.

In the new $k-l$ turbulence model, the k-equation is expressed in a new integral contravariant form on a generalized time-dependent curvilinear coordinate system. In this model, the equations of motion are solved also in the buffer layer, while the k-equation is solved starting from the buffer layer in the proximity of the viscous sublayer. Outside the oscillating wave boundary layer, a new formula for the mixing length is proposed as a function of the first and second spatial derivatives of the local maximum water surface elevation. In the oscillating wave boundary layer, the mixing length is calculated by the hypothesis of the balance between production and dissipation of turbulent kinetic energy.

In the new $k-\omega$ turbulence model, the k and ω equations are written in a new integral contravariant form on a generalized time-dependent curvilinear coordinate system. The new $k-\omega$ turbulence model admits the possibility to assign the boundary condition for the specific dissipation rate directly at the

bottom. In this model, the equations of motion are solved starting from the buffer layer and the k and ω-equations are solved in the buffer layer at the border with the viscous sublayer. The production of turbulent kinetic energy in the zone between the breaking wave fronts and the oscillating wave boundary layer is reduced by introducing a dynamic coefficient for the dissipation of ω and a limiter in the eddy viscosity.

In this thesis, the new $k-\omega$ turbulence model is used to directly simulate the unsteady quasi-periodic vortex structures due to the interaction between breaking waves and coastal works.

Keywords: three-dimensional model, shock-capturing numerical scheme, WTENO reconstructions, turbulence models, URANS models, oscillating wave boundary layer, Smagorinsky, new $k-l$ turbulence model, new $k-\omega$ turbulence model, boundary conditions, unsteady quasi-periodic vortex structures, wave-structure interaction.

Contents

List of Figures

List of Tables

Nomenclature

$\alpha, \alpha_\omega, \beta, \beta^*, \beta_\omega, \beta_{\omega 1}, \zeta, \sigma, \sigma^*, \sigma_d, \sigma_{d0}, \sigma_k, \sigma_\omega, \sigma_{\omega'}, \sigma_{\omega' 0}, B_c, C_{lim}, C_\mu, C_{\omega 2}, C_\omega, l_2, k_1, k_2$ Coefficients of the turbulence models [-]

$(\quad)^*$ Predictor value of the conserved variable

$(\quad)^c$ Conserved value of the conserved variable

$(\quad)^{+/-}_{i+/-\frac{1}{2},j,k}$ Point value of the conserved variables on the right and left side of the computational grid cells in i-direction $i, j, k = 1, 2, 3$

$(\quad)_{i,j,k}$ Generic value defined at the center of the computational cell $i, j, k = 1, 2, 3$

$(\widehat{\ })$ Line-averaged value of a generic variable

$(\widetilde{\ })$ Surface-averaged value of a generic variable

α Beach slope [°]

β_p Smoothness indicator [-]

$\cdot$ Scalar product

$\Delta A(t)$ Boundary surface of the moving control volume $[m^2]$

$\Delta A_0^{\alpha+}$ and $\Delta A_0^{\alpha-}$ Control volume boundary surfaces of ΔV_0 in the transformed space ($\alpha = 1, 2, 3$) [-]

$\Delta A_1^\alpha(\tau)$ Surface boundary of the time-varying control volume in curvilinear coordinate $[m^2]$

$\Delta V(t)$ Moving control volume $[m^3]$

ΔV_0 Control volume in the transformed space [-]

$\Delta V_1(\tau)$ Time-varying control volume in curvilinear coordinate $[m^3]$

$\Delta x, \Delta y, \Delta z$ Spatial discretization in x, y, z-direction $[m]$

Δx^l Spatial discretization in transformed space $l = 1, 2, 3$ [-]

Δ Length scale $[m]$

δ^{lm} Kronecker symbol [-]

δ_p Cut-off functions $p = -1, 0, 1$ [-]

$\dot{\omega}_p$ Non-linear weights $p = -1, 0, 1$ [-]

η Free-surface elevation $[m]$

$\eta_{max}(\xi^1)$ Local maximum water surface elevation (over time) $[m]$

$\eta_{min}(\xi^1)$ Local minimum water surface elevation (over time) $[m]$

$\frac{\partial \eta_{max}(\xi^1)}{\partial \xi^1}$ First spatial derivative of the local maximum water surface elevation [-]

$\frac{\partial \eta}{\partial t}$ Local time rate of change of the free-surface elevation $[ms^{-1}]$

$\frac{\partial^2 \eta_{max}(\xi^1)}{\partial (\xi^1)^2}$ Second spatial derivative of the local maximum water surface elevation [-]

Γ_p Normalized regularity function $p = -1, 0, 1$ [-]

γ_p Regularity functions $p = -1, 0, 1$ [-]

$\hat{n}$ outward-normal unit vector [-]

κ von Kàrmàn constant $[m]$

λ_m $m - th$ covariant component of $\tilde{\vec{g}}^{(l)}$ $[m^{-1}]$

$\lambda_{max}(\xi^1)$ Local water height point $[m]$

$\left(\frac{\partial \eta}{\partial t}\right)^*$ Threshold value of $\partial \eta / \partial t$

μ Dynamic viscosity $[kgs^{-1}m^{-1}]$

$\mu, \epsilon, C, d, B_l, B_h$ WTENO coefficients [-]

∇ Nabla operator

ν Kinetic viscosity $[m^2 s^{-1}]$

ν_T Eddy viscosity $[m^2 s^{-1}]$

ω Dissipation of turbulent kinetic energy per unit of turbulent kinetic energy or specific dissipation rate $[s^{-1}]$

Ω^{lm} Contravariant components of the vorticity tensor $\underline{\Omega}$ $(l, m = 1, 2, 3)$ $[s^{-2}]$

$\otimes$ Tensor product

$\overline{\Theta}(t)$ Generic hydrodynamic quantity related to the time periodicity $[-]$

$\overline{u}_i$ Cartesian Reynolds averaged components of the velocity vector $\vec{u}$(i=1,2,3)$[ms^{-1}]$

Ψ Scalar potential $[m^2 s^{-1}]$

ρ Fluid density $[kgm^{-3}]$

$\sqrt{g_0}$ Factor of the Jacobian of the transformation $[m^2]$

$\sqrt{g}$ Jacobian of the transformation $[m^3]$

τ Time in curvilinear coordinate system $[s^{-1}]$

τ_w Tangential stresses near the bottom $[kgm^{-1}s^{-2}]$

$\Theta'(t)$ Turbulent fluctuation of the generic hydrodynamic quantity $[-]$

$\Theta(t)$ Generic instantaneous hydrodynamic quantity $[-]$

$\theta, \quad \theta_2$ WTENO functions [-]

$\tilde{\omega}, \tilde{\tilde{\omega}}$ Comparison values of dissipation of turbulent kinetic energy per unit of turbulent kinetic energy $[s^{-1}]$

$\tilde{\Theta}(t)$ Generic hydrodynamic quantity related to the quasi-periodicity of the vortex structures $[-]$

$\underline{\Omega}$ Vorticity tensor $[s^{-1}]$

$\underline{E}$ Surface forces $[kgs^{-2}m^{-1}]$

$\underline{I}$ Identity tensor [-]

$\underline{R}$ Viscous stress tensor $[kgs^{-2}m^{-1}]$

$\underline{S}$ Strain rate tensor $[s^{-1}]$

$\underline{T}$ Turbulent stress tensor $[kgm^{-1}s^{-2}]$

ε Dissipation of turbulent kinetic energy $[m^2s^{-3}]$

$\vec{\lambda}$ Physical direction on which project the momentum balance equation [-]

$\vec{f}$ External body forces per unit of vector $[kgs^{-2}m^{-1}]$

$\vec{g}^l$ $l-th$ contravariant component of the base vector $(l = 1, 2, 3)$ $[m^{-1}]$

$\vec{g}_l$ $l-th$ covariant component of the base vector $(l = 1, 2, 3)$ $[m]$

$\vec{u}$ Cartesian fluid velocity vector $[ms^{-1}]$

$\vec{w_g}$ Cartesian velocity vector of the moving coordinate $[ms^{-1}]$

$\wedge$ Vector product

ξ^l Curvilinear coordinates $(l = 1, 2, 3)$ [-]

ξ_b Iribarren number [-]

$a_{(p)i,j,k}, \quad b_{(p)i,j,k}, \quad c_{(p)i,j,k}$ Coefficient of the polynomials $p = -1, 0, 1$; $l, i, j, k = 1, 2, 3$ [-]

C_p Linear weights $p = -1, 0, 1$, $l, i, j, k = 1, 2, 3$ [-]

C_S Smagorinsky coefficient [-]

C_T Dynamic threshold [-]

$F_{i,j,k}(\xi^l)$ Polynomial functions defined at the center of the computational grid cell $I_{i,j,k}$ $i, j, k, l = 1, 2, 3$

G Acceleration due to the gravity $[ms^{-2}]$

g^{lm} Contravariant metric tensor $(l, m = 1, 2, 3)$ $[m^{-2}]$

g_{lm} Covariant metric tensor $(l, m = 1, 2, 3)$ $[m^2]$

H Total water depth $[m]$

h Still water depth $[m]$

H_b Total water depth at the breaking point $[m]$

H_b Wave height at the breaking point $[m]$

H_s Wave height $[m]$

Hu^l Conserved variable $[ms^{-1}]$

$I^{+/-}_{i+/-\frac{1}{2},j,k}$ Faces of a generic hexahedral computational cell in i-direction $i, j, k = 1, 2, 3$ [-]

I^{lm} Contravariant components of the identity tensor $(l, m = 1, 2, 3)$ [-]

$I_{i,j,k}$ Generic hexahedral computational cell $i, j, k = 1, 2, 3$ [-]

k Turbulent kinetic energy $[m^2s^{-2}]$

l Mixing length $[m]$

L_0 Wavelenght $[m]$

n Exponent of the dynamic threshold

P Total pressure $[kgs^{-2}m^{-1}]$

P_k Production of turbulent kinetic energy $[m^2s^{-3}]$

$P_{(p)i,j,k}(\xi^l)$ Second-order polynomials $p = -1, 0, 1$, $l, i, j, k = 1, 2, 3$ [-]

p_{dyn} Dynamic pressure $[kgs^{-2}m^{-1}]$

Q Second invariant of the velocity gradient [-]

R^{lm} Contravariant components of the viscous stress tensor $\underline{R}$ $(l, m = 1, 2, 3)$ $[s^{-2}]$

S^{lm} Contravariant components of the strain rate tensor $\underline{S}$ $(l, m = 1, 2, 3)$ $[s^{-1}m^{-2}]$

S_C Bottom roughness $[m]$

S_C^+ Dimensionless bottom roughness [-]

T Wave period $[s]$

t Time in Cartesian coordinate system $[s]$

T_{ij}^{dev} Cartesian components of the deviatoric part of the turbulent stress tensor $(i, j = 1, 2, 3)$ $[kgm^{-1}s^{-2}]$

T^{lm} Contravariant components of the turbulent stress tensor $\underline{T}$ $(l, m = 1, 2, 3)$ $[s^{-2}]$

T_s Simulation time $[s]$

T_{ij} Cartesian components of the turbulent stress tensor $(i, j = 1, 2, 3)$ $[kgm^{-1}s^{-2}]$

$tr(\ )$ Trace of a square matrix

u_i' Turbulent fluctuations of the velocity (i=1,2,3) $[ms^{-1}]$

u, v, w Cartesian component of the fluid velocity vector $[ms^{-1}]$

u^* Friction velocity $[ms^{-1}]$

u^l Contravariant component of the fluid velocity $(l = 1, 2, 3)$ $[s{-}1]$

u_B Velocity boundary condition $[ms^{-1}]$

v^l Contravariant component of a generic vector $\vec{v}$ $(l = 1, 2, 3)$ [-]

v_l Covariant component of a generic vector $\vec{v}$ $(l = 1, 2, 3)$ [-]

w_g^l Contravariant component of the velocity of the moving coordinate $(l = 1, 2, 3)$ $[s^{-1}]$

x^l Cartesian coordinates $(l = 1, 2, 3)$ $[m]$

y^+ Dimensionless wall distance [-]

z Vertical distance from the wall $[m]$

Acronyms

KLN New $k-l$ turbulence model

KLS Standard $k-l$ turbulence model

MPI Message Passing Interface

PDEs partial differential equations

TENO Targeted Essentially Non-Oscillatory

TVD Total Variation Diminishing

URANS Unsteady Reynolds-Averaged Navier-Stokes Equations

VOF Volume of Fluid

WTENO Wave-Targeted Essentially Non-Oscillatory

Chapter 1

Introduction

1.1

The hydrodynamic phenomena in the proximity of coastlines are very complex: in particular, the interaction between waves and coastal works induces fully three-dimensional velocity fields. One of the complex phenomena is the undertow, that consists in a nearshore circulation current in which the velocities near the free surface are onshore directed, while the velocities near the bottom are offshore directed.

The numerical models used for the simulations of free-surface flows that solve the three-dimensional equations of motion and take into account the dynamic pressure component, are able to simulate the velocity field in deep water, in intermediate water and in the surf zone. These models, differently from the depth-averaged models based on the Boussinesq equations [11, 16, 24, 53, 66], can simulate the wave breaking without using an *a priori* criterion to localize the point where the breaking zone starts.

1.2

Several models present in the literature [3, 6, 28] use Volume of Fluid (VOF) methodology for the three-dimensional simulations of free-surface flows.

This methodology is based on the simulations of a two-phase flow (air-water): the simulation of the fluid motion uses continuity equations for the two phases

and a momentum balance equation for the mixture. The volume fraction of the air is calculated by a continuity equation for the above-mentioned fraction, while the continuity equation for the fluid phase is the null divergence of the velocity. In the cells occupied by the water, the volume fraction of the air phase is null, while the volume fraction of the water is one; it is vice-versa for the cells occupied by air. The location of the free surface is in the cells where the volume fraction of the water changes from zero to one. The free surface does not correspond with a cell boundary and, therefore, it is difficult to correctly assign the pressure boundary condition and the kinematic condition exactly at the free surface [43]. By using this methodology, a small spatial discretization step and a considerable number of grid points (that limits the applicability for real-scale numerical simulations) is needed to correctly simulate the wave breaking.

An alternative numerical procedure (for the three-dimensional simulation of wave motion), which overcomes the above-mentioned VOF drawbacks, is defined in the context of the shock-capturing numerical schemes and is based on a vertical coordinate (called σ [55]) which varies in time in order to follow the free-surface evolution [7, 8, 47]. By using this σ-coordinate transformation, the time-varying physical domain is transformed in a regular, fixed and prismatic computational domain whose upper boundary corresponds to the free surface. By this approach, the zero pressure condition can be imposed exactly on the free surface, without any approximation. In the σ-coordinate models present in the literature, the horizontal coordinates are the Cartesian ones and the motion equations are expressed in terms of Cartesian-based variables.

1.3

The study of the three-dimensional wave motion in domains characterized by complex geometries can be carried out by models that are a generalization of the σ-coordinate models. The above-mentioned generalization was carried out by Ogawa et al [50] and Luo et al [46] which proposed a complete contravariant formulation of the differential Navier-Stokes equations in a time-dependent curvilinear coordinate system.

The numerical integration of the differential motion equations for the simulation of a shock wave can produce numerical solution with shock waves that have erroneous propagation speeds. An erroneous propagation speed of the shock does not allow to correctly determine the position of the discontinuity at a given time. In the numerical simulation of shock waves, the numerical scheme should be able to preserve the properties of the continuum system, as the conservation of global quantities and the conservation of the invariants across a discontinuity.

As underlined by Toro [67], in the numerical integration of the differential equations of motion, the convective terms that are not written in the divergence form do not allow the formulation of the equations of motion in conservative form. The discretization of a non-conservative form of the equations of motion does not guarantee the convergence of the numerical schemes to the correct weak solution in presence of discontinuities and does not guarantee the correct simulation of the shock propagation speed. The use of the conservative form of the equations of motion is a necessary but not sufficient condition for the convergence of the numerical scheme to the correct weak solution.

The equations of motion expressed in contravariant form include the covariant derivatives of the contravariant vector components. These covariant derivatives involve the presence of the Christoffel symbols which, as known [1], are due to the space variability of the base vectors. The discretization of these symbols introduces computational errors associated with the non-uniformities of the calculation grid cells that can compromise the accuracy of the numerical solution. Moreover, the presence of the Christoffel symbols does not allow the convective terms of the equations of motion to be expressed in conservative form. The numerical methods for the simulation of the conservation laws, in which the convective terms are expressed in non-conservative form, do not guarantee, as already written, the convergence to the correct weak solution [67].

As emphasized by Toro [67], the equations of motion written in conservative form, but expressed in terms of primitive variables (H, total water depth and $\vec{u}$, Cartesian vector of fluid velocity), can produce shock waves with erroneous propagation speeds. The integral form of the equations of motion expressed in terms of conservative variables (H and $H\vec{u}$) allows the formulation of conservative

numerical schemes that can converge to the correct weak solution.

In this thesis, a new numerical model for the simulation of the breaking waves is presented. This model is based on the solution of the three-dimensional equations of motion expressed in integral contravariant form. These equations are collocated in a context of complete generality, are devoid of the Christoffel symbols and are expressed in terms of conservative variables, H and $H\vec{u}$

1.4

Some considerations on the numerical methods for the solution of the equations of motion in breaking wave simulations should be done. The wave breaking increases the turbulent agitations and, consequently, produces an increment of the dissipation of the kinetic energy of the ensemble-averaged motion, in which only the complete spectrum of the stochastic turbulent motion is not directly simulated.

In [9, 11, 12, 20, 23, 25, 31, 33, 47, 52], the breaking waves are simulated as shock waves and the three-dimensional equations of motion are numerically integrated by a finite-volume shock-capturing numerical scheme that adopt a 2^{nd}-order Total Variation Diminishing (TVD) reconstruction technique and an approximate Riemann solver.

In the above models, the adopted low-order shock-capturing numerical schemes take the task of dissipating most of the kinetic energy of the ensemble-averaged motion in the surf zone, although this task should be performed by the turbulence models.

It has been demonstrated by [13, 26, 51] that the breaking wave simulation carried out by such low-order numerical scheme (2^{nd}-order TVD reconstructions and approximate Riemann solver) are affected by some drawbacks: the increase of the wave height during shoaling is underestimated, the wave breaking point is not correctly evaluated and the decrease of the wave height in the surf zone is not well predicted. The latter drawback produces an underestimation of the wave-induced currents in the surf zone. The above-mentioned drawbacks can be overcome (even by using TVD numerical schemes and approximate Riemann solvers) by adopting fine grids (especially in the horizontal direction) with small spacial discretization

steps. The use of the fine grids limits the application of these schemes mainly to laboratory-scale case studies.

In this thesis, in order to overcome the above-listed drawbacks of the low-order shock-capturing numerical schemes, a new high-order shock-capturing numerical scheme for the solution of the three-dimensional ensemble-averaged motion equations is presented. The elements of novelty in this new numerical scheme are two. The first element of novelty consists in the proposal of a new reconstruction technique of the point values of the conserved variables on the cell faces of the computational grid (starting from the cell-averaged values of the same variables). This reconstruction technique is named Wave-Targeted Essentially Non-Oscillatory (WTENO) and it is specifically designed for three-dimensional simulations of breaking waves. The second element of novelty consists in the use of an exact solution for the Riemann problem to advance in time the point values of the conserved variables at the cell faces.

1.5

As mentioned above, the low-order shock-capturing numerical schemes [6, 20, 47] leave to the numerical scheme the task of dissipating the kinetic energy of the ensemble-averaged motion in the surf zone: indeed, in the above-mentioned shock-capturing numerical schemes, a Smagorinsky turbulence model (with low value of the Smagorinsky coefficient) is used to introduce a minimal dissipation of the kinetic energy of the ensemble-averaged motion, in order to remove the spurious oscillations that can arise in the numerical solution. Instead, by using high-order shock-capturing numerical schemes, the dissipation of the kinetic energy of the ensemble-averaged motion introduced by the numerical scheme is limited and the task of dissipating this energy is left to a turbulence model. For this reason, it is necessary to develop more innovative turbulence models that are able to adequately represent the turbulent phenomena at the wave breaking, at the bottom and in the proximity of the walls of coastal works.

1.6

In presence of coastal works, their interaction with the waves produces hydrodynamic fields characterized by unsteady quasi-periodic vortex structures and stochastic turbulent fluctuations. The quasi-periodic vortex structures are unsteady phenomena that arise from the interaction between the fluid and the coastal works. The stochastic turbulent fluctuations are superimposed on the unsteady quasi-periodic motion of the vortex structures.

By following the suggestion of Bosh and Rodi [5], the generic instantaneous hydrodynamic quantity $\Theta(t)$ is separated into three components. The first component is represented by the value of the hydrodynamic quantity $\overline{\Theta}(t)$, whose time periodicity is related only to the wave periodicity. The second component $\tilde{\Theta}(t)$ is related to the quasi-periodicity of the vortex structures produced by the interaction between fluid and coastal works. The third component $\Theta'(t)$ is the turbulent fluctuation. In accordance with Bosh and Rodi [5], the sum of $\overline{\Theta}(t)$, related to the periodicity of the wave, and $\tilde{\Theta}(t)$, related to the quasi-periodicity of the vortex structures, gives rise to the ensemble-averaged component, which is calculated by numerically solving the ensemble-averaged motion equations. In this context, the complete spectrum of the stochastic turbulent motion is represented by a turbulence model. The numerical models coherent with the above-mentioned approach are named, in the literature, URANS (Unsteady Reynolds-Averaged Navier-Stokes Equations) models.

It is necessary recalling the fact that the product between the ensemble-averaged velocity and the divergence of the Reynolds stress tensor represents the dissipation of kinetic energy of the ensemble-averaged motion. An overestimation of the Reynolds stress tensor (that is the unknown tensor of the ensemble-averaged Navier-Stokes equations) produces an excess of dissipation of the kinetic energy of the ensemble-averaged motion.

In the literature, the turbulent closure relations for the Reynolds stress tensor in breaking wave simulations are expressed by different turbulence models, like the Smagorinsky model, one-equation or two-equation turbulence models.

In recent papers [44, 47, 73], the Smagorinsky turbulence model is calibrated for three-dimensional numerical simulations of wave propagation from deep-water

to the coastline.

It should however be recalled that the existing numerical models, that use the Smagorinsky turbulence model [47], are collocated in the context of low-order of accuracy shock-capturing numerical schemes. In these schemes, the reconstructions of point values of the conserved variables are made by a 2^{nd} order TVD scheme and the Riemann problem is solved by an approximate Riemann solver. These models leave the task of dissipating the kinetic energy of the ensemble-averaged motion in the surf zone to the shock-capturing numerical scheme and use the Smagorinsky turbulence model with low values of the Smagorinsky coefficient, in order to eliminate some spurious oscillations. In the cases in which 2^{nd} order shock-capturing numerical schemes are used, the breaking wave height is underestimated and the wave breaking point is shifted offshoreward.

In order to reduce the dissipation of the kinetic energy of the ensemble-averaged motion introduced by the low-order numerical schemes and leave the task of dissipating this kinetic energy only to the turbulence model, it is necessary to develop a new high-order numerical scheme and adequate turbulence models.

Some considerations should be done about the use of the Smagorinsky turbulence model with high-order shock-capturing numerical schemes. As it is well known, in these models, the turbulent stress tensor is related to the strain rate tensor through the Smagorinsky coefficient and the spatial discretization step of the calculation grid. As it is demonstrated in this thesis, by using high-order numerical schemes, high values of the Smagorinsky coefficient can produce an overestimation of the eddy viscosity in the shoaling zone, in the region around the wave breaking point and in the surf zone. The same overestimation can be produced by adopting too large spatial discretization steps. High values of this geometrical parameter increment the eddy viscosity and thus overestimate the dissipation of the kinetic energy of the ensemble-averaged motion in the region around the wave breaking point and in the surf zone. The strong influence of the Smagorinsky coefficient and the grid dimension on the numerical solution can produce numerical results very different from each other. Furthermore, the Smagorinsky turbulence model does not give any information about the turbulent kinetic energy distribution in the domain; for this reason, it is not possible

to validate the model in terms of turbulent kinetic energy.

1.7

To overcome the Smagorinsky turbulence model drawbacks, many authors [6, 18, 19] used a one-equation turbulence model called $k-l$ (k is the turbulence kinetic energy and l is the mixing length), in which a partial differential equation for the turbulent kinetic energy is solved and the closure relation for the turbulent stress tensor is a function of the turbulent kinetic energy and the mixing length.

Some synthetic considerations should be done about the turbulent structures in the surf zone. The turbulent structures in the surf zone are very complex. Outside the surf zone, the production of turbulent kinetic energy is limited to the oscillating bottom boundary layer, called oscillating wave boundary layer; inside the surf zone, the production of turbulent kinetic energy is mainly located in the oscillating wave boundary layer and near the breaking wave fronts. A part of the turbulent kinetic energy produced at the wave breaking point and in the oscillating wave boundary layer is dissipated in the intermediate zone, between the oscillating wave boundary layer and the wave fronts. In the existing $k-l$ turbulence models [6, 18, 19], the dissipation of turbulent kinetic energy is represented in the same way both before and after the wave breaking point. In particular, these models do not take into account the differences between the turbulent phenomena in the shoaling zone, the region around the wave breaking point and the surf zone. In the papers present in the literature [6, 18, 19, 47] concerning breaking wave simulations that adopt the Smagorinsky or the $k-l$ turbulence model, the equations of motion are not solved in the zone nearest to the bottom.

As it is known, the oscillating wave boundary layer can be divided into three regions: the viscous sublayer, the buffer layer and the turbulent core. In order to simulate the turbulent phenomena and their effects on turbulent kinetic energy in the oscillating wave boundary layer (inside the turbulent core and the buffer layer) and in the proximity of the free surface inside the breaking zone, it is necessary implement an adequate $k-l$ turbulence model.

1.8

In order to reduce the dissipation of the kinetic energy of the ensemble-averaged motion due to the numerical scheme and leave the task of dissipating this energy only to the turbulence model, in this thesis (as already written above), a new 5^{th}-order shock-capturing numerical scheme is used. In this thesis, two turbulence models, $k-l$ and $k-\omega$ (ω is the dissipation of the turbulent kinetic energy per unit of turbulent kinetic energy, hereinafter called specific dissipation rate), are proposed. These models are collocated in the context of the URANS models and intervene in the ensemble-averaged momentum equation, in order to directly simulate the unsteady quasi-periodic vortex structures, leaving the task of dissipating the complete spectrum of the stochastic turbulent motion to the turbulence model.

In order to take into account the turbulent phenomena that occur before and after the wave breaking point and in the oscillating wave boundary layer, a new $k-l$ turbulence model is proposed. The k-equation is written in a new integral contravariant form on a generalized time-dependent curvilinear coordinate system. In this model, a new formula of the mixing length outside the oscillating wave boundary layer is proposed. The mixing length is calculated as a function of the first and second spatial derivatives of the local maximum water surface elevation. In the oscillating wave boundary layer, the mixing length is calculated by assuming the hypothesis of balance between production and dissipation of turbulent kinetic energy in all the turbulent core. The first calculation point in which the equations of motion are solved is placed in the buffer layer, while the first calculation point in which the turbulent kinetic energy equation is solved is placed in the buffer layer, in the proximity of the viscous sublayer.

In order to obtain an adequate representation of the turbulent phenomena both in the oscillating wave boundary layer and on the wave breaking fronts, it is necessary take into account the considerable variability of the production and dissipation of the turbulent kinetic energy along the water column and in the surf zone. For this reason, it is clear that it is necessary an adequate and laborious calibration of the mixing length with the $k-l$ turbulence model. The definition of

the mixing length in the oscillating wave boundary layer leads to the assumption that the balance between production and dissipation of turbulent kinetic energy holds true in all the turbulent core. The above-mentioned balance strictly holds true at the interface between the turbulent core and the buffer layer [10]. Given the need to scrupulously represent the effects that the turbulent phenomena have in the dissipation of the kinetic energy of the ensemble-averaged motion in the proximity of the bottom, in the definition of the mixing length, it is necessary to remove the hypothesis of the balance between production and dissipation of turbulent kinetic energy in all the turbulent core. Hence, it is necessary to develop a more general two-equation turbulence model ($k-\omega$), which is able to overcome the drawbacks of the new $k-l$ turbulence model and take into account the effects of the turbulent phenomena in the oscillating wave boundary layer, till the border between the buffer layer and the viscous sublayer.

1.9

In the direct simulation of the quasi-periodic vortex structures, mainly due to the interaction between the waves and coastal works, it is necessary to solve the equations of motion also inside the turbulent core and the buffer layer (with small spatial discretization steps in the proximity of the obstacle walls) and to adequately represent the turbulent phenomena in the proximity of the walls.

Franke and Rodi [21] have shown that the occurrence and quality of the vortex structures prediction depend strongly on the used turbulence model. From a general point of view, traditionally, one-equation and two-equation turbulence models [6, 18–20, 41, 42, 44, 45, 47, 58, 72, 73] were found to severely underpredict the strength of the vortex structures, mainly because of excessive production of turbulent kinetic energy. When the production of turbulent kinetic energy is too high, the Reynolds stress tensor is overestimated. The product between the ensemble-averaged velocity and the divergence of the stress tensor represents the dissipation of the kinetic energy of the ensemble-averaged motion. An overestimation of the Reynolds stress tensor produces an excess of dissipation of the kinetic energy of the ensemble-averaged motion. Consequently, by using turbu-

lence models that produce an excessive production of turbulent kinetic energy, the unsteady quasi-periodic vortex structures (beside all of the stochastic turbulent fluctuations) are expelled from the direct simulations of the ensemble-averaged motion.

From the previous considerations, it is necessary to develop turbulence models that is collocated in the context of the URANS model and intervene in the ensemble-averaged momentum equation in order to expel from the simulation of the fluid velocity field just the stochastic turbulent fluctuations. In this way, it is possible to properly evaluate, without overestimate, the Reynolds stress tensor and adequately and directly simulate the wave breaking, the wave fields, the velocity fields and the unsteady quasi-periodic vortex structures due to the interaction between waves and coastal works.

In the context of the URANS model, two-equations $k-\omega$ turbulence model [49, 70, 71], is able to represent the turbulent phenomena, so that the numerical models can directly simulate the unsteady quasi-periodic vortex structures, is also able to give correct boundary conditions at the bottom and does not need to define a specific mixing length. The turbulent kinetic energy dissipation ε (in the $k-\varepsilon$ turbulence model [20, 41, 42, 45, 58, 72]) does not admit boundary conditions at the bottom; the specific dissipation rate ω admits bottom boundary condition [49, 70, 71].

One of the first $k-\omega$ turbulence model present in the literature is the one proposed by Wilcox [70] and it is used to simulate compressible flow around a airfoil. Wilcox proposed a boundary condition for the specific dissipation rate ω that incorporates the effects of the surface roughness. As underlined by several authors [49, 71], the Wilcox model has the tendency to overestimate the eddy viscosity when the production of turbulent kinetic energy is significantly increased and the specific dissipation rate is not able to reduce the growth of turbulent kinetic energy.

Wilcox proposed a new $k-\omega$ model [71] in which the eddy viscosity is limited. Furthermore, a cross-diffusion term is added in ω-equation to enhance ω production in order to increase the dissipation of turbulent kinetic energy.

Mayer and Madsen [48] have used the Wilcox $k-\omega$ turbulence model [70] in the simulation of the breaking waves. They have demonstrated that this $k-\omega$ turbulence model produces an excessive production of turbulent kinetic energy in the zone between the breaking wave fonts and the oscillating wave boundary layer. This excessive production of turbulent kinetic energy induces an overestimation of the Reynolds stress tensor. In the numerical simulations of the wave and velocity fields, the overestimation of the Reynolds stress tensor produces an excessive reduction of the wave height and the wave breaking point is shifted offshoreward.

In this thesis, a new $k-\omega$ turbulence model is proposed for the simulation of the breaking waves and the interaction between waves and coastal works at the wave breaking. The k and ω equations are formulated in a new integral contravariant form on a generalized time-dependent curvilinear coordinate system.

It is necessary to recall that, in $k-\omega$ turbulence model, the eddy viscosity is the ratio of turbulent kinetic energy to specific dissipation rate. In order to limit the production of the turbulent kinetic energy in the zone between the breaking wave fronts and the oscillating wave boundary layer, in the new $k-\omega$ turbulence model, the denominator of the eddy viscosity is calculated as the maximum value between three terms: the first one is directly calculated by the ω-equation; the second one is a function of absolute value of the strain rate tensor and the absolute value of the vorticity tensor; the third value is calculated by the product between the absolute value of the strain rate tensor and a coefficient that is activated as a function of the zone in which it is calculated. This coefficient is determined by the local maximum water depth and is increased in the surf zone, where the local maximum water depth is reduced. In such a way, the behaviour of the model before and after the wave breaking point is differentiated.

In order to further reduce the production of the turbulent kinetic energy in the zone between the breaking wave fronts and the oscillating wave boundary layer, in the new $k-\omega$ turbulence model, a dynamic coefficient for the dissipation of ω is added by following the line proposed by Yakhot [72]. In the new $k-\omega$ turbulence model proposed in this thesis, a dynamic procedure (which is a function of the strain rate tensor) to calculate this coefficient is introduced. For high values of the strain rate tensor, the coefficient that multiplies the dissipation of ω decreases, by further reducing the production of turbulent kinetic energy.

The velocity boundary condition is calculated without using logarithmic laws and it is placed at the border between the buffer layer and the viscous sublayer. The boundary condition for the turbulent kinetic energy is null directly at the bottom. The boundary condition for the dissipation rate is placed at the bottom and it is a function of the bottom roughness and the friction velocity (the friction velocity is calculated by the viscous stress at the border between the viscous sublayer and the buffer layer). The k and ω equations are solved starting from the border between the viscous sublayer and the buffer layer. Since the turbulent equations are solved near the bottom, it is possible to directly simulate the unsteady quasi-periodic vortex structures due to the interaction between breaking waves and coastal works.

In summary in this thesis, a new model for the simulation of breaking waves is presented. In this model, the three-dimensional equations of motion, expressed in terms of conserved variables H and $H\vec{u}$, are written in integral contravariant form on a time-dependent curvilinear coordinate system. These equations are solved by using a 5^{th}-order shock-capturing numerical scheme that employs a new method for the reconstructions of the point values of the conserved variables at the center of the cell faces, called WTENO and an exact Riemann solver.

Two turbulence models collocated in the context of the URANS are proposed in this thesis.

In the new $k-l$ turbulence model, a new k-equation is proposed in contravariant formulation. In this model, the equations of motion are solved also in the buffer layer, while the turbulent kinetic energy equation is solved also in the buffer layer, in the proximity of the viscous sublayer. In the oscillating wave boundary layer, the mixing length is calculated by the hypothesis of the balance between production and dissipation of turbulent kinetic energy. Outside the oscillating wave boundary layer, a new formula for the mixing length is proposed as a function of the first and second spatial derivatives of the local maximum water surface elevation. In this way, the turbulence model is able to take into account the different turbulent phenomena that occur before and after the wave breaking point.

In the new $k-\omega$ turbulence model, two new equations for k and ω in contravariant formulation are proposed. This model gives the possibility to assign the bottom boundary condition for ω directly at the bottom. By using the new turbulence model, the production of turbulent kinetic energy in the zone between the breaking wave fronts and the oscillating wave boundary layer is reduced, because the eddy viscosity is limited and a dynamic coefficient for the dissipation of ω is introduced. By using the new $k-\omega$ turbulence model, it is possible to directly simulate the unsteady quasi-periodic vortex structures due to the interaction between breaking waves and coastal works.

The thesis is organized as follow: in Chapter 2, the integral form of the contravariant equations of motion on a time-dependent generalized curvilinear coordinate system is presented; in Chapter 3, the new 5^{th}-order shock-capturing numerical scheme is presented; in Chapters 4, 5 and 6, the existing Smagorinsky, $k-l$ and $k-\omega$ turbulence models and the new two $k-l$ and $k-\omega$ turbulence models, proposed in this thesis, are presented; in Chapter 7, the numerical results of the interaction between breaking waves and an emerged barrier, obtained by the new $k-\omega$ turbulence model, are presented.

Chapter 2

Motion Equations

In this Section the three-dimensional equations of motion written in integral contravariant form on a time-dependent curvilinear coordinate system and the Poisson-like equation (that is the Laplacian of a scalar potential) are presented. The equations of motion and the Poisson-like equation are written in terms of conserved variables (the total water depth H and the product between the total water depth and the fluid velocity vector $H\vec{u}$).

2.1 Conserved Variables

The propagation speed of a shock wave produced by a numerical simulation can be incorrect. An erroneous propagation speed of the shock wave do not allow to correctly locate the position of the discontinuities. In the simulation of the shock waves, the numerical schemes should be able to preserve the properties of the continuum system, as the conservation of the global quantities and the conservation of the invariants across a discontinuity.

In the numerical integration of the differential equations of motion, the discretization of the convective terms do not allow the formulation of a conservative schemes, if these terms are not written in the form of the divergence, as underlined by Toro [67]. Non conservative numerical schemes do not to guarantee the convergence to the correct weak solution with discontinuity and do not allow to correctly simulate the propagation speed of the shock wave. The use of conservative schemes is necessary but not sufficient so that the numerical scheme converges to the correct weak solution with discontinuity. Indeed, conservative numerical

schemes in which the convective terms are written in divergence form, if applied to equations of motion expressed in terms of primitive variables (total water depth H and fluid velocity vector $\vec{u}$), can produce shock waves with erroneous propagation speed. On the contrary, the integral form of the equations of motion in which the conserved variables (H and $H\vec{u}$) are used allows the formulation of conservative schemes that can converge to the correct weak solution.

For this reason, in this thesis, the equations of motion and the Poisson equation are written in terms of the conserved variables (H and $H\vec{u}$).

2.2 Equations of motion

The three-dimensional integral contravariant form of the incompressible Navier-Stokes equations written in a time-dependent curvilinear coordinate system are the equations of motion of the proposed numerical model. These equations are derived from the integral form of the mass conservation and momentum balance equations expressed on a moving control volume.

In the Cartesian the coordinate system (x^1, x^2, x^3, t), the integral form of the mass conservation equation on a moving control volume for an incompressible flow reads

$$\frac{d}{dt}\int_{\Delta V(t)} dV + \int_{\Delta A(t)} (\vec{u} - \vec{w}_g) \cdot \hat{n} dA = 0 \tag{2.1}$$

where $\Delta V(t)$ and $\Delta A(t)$ are the moving control volume and its boundary surface; $\vec{u}$ and $\vec{w}_g$ are the Cartesian fluid velocity vector and the velocity vector of boundary surface control volume; $\hat{n}$ is the outward-normal unit vector; the symbol $\cdot$ is the scalar product between vectors and between vectors and second-order tensor.

The equations of motion in contravariant form contain covariant derivatives of contravariant vectors. These derivatives involve the presence of the Christoffel symbols due to the variability of the base vectors. The discretization of the Christoffel symbols introduces computational errors related to the non uniform grid cells that can compromise the accuracy of the numerical solution. Furthermore the presence of the Christoffel symbols do not allow that the convective terms of the equations of motion are expressed in conservative form. As stated in Section 2.1 and in [1, 67], the numerical schemes do not guarantee the convergence to the correct weak solution with discontinuity, if the convective terms in

the conservation laws are expressed in non conservative form.

In order to avoid the Christoffel symbols, the integral form of the momentum balance equation must be projected onto a physical direction $\vec{\lambda}$. This physical direction is the direction of a constant and parallel vector field: in the Cartesian coordinate system, this vector field has constant and uniform components; while in curvilinear coordinate systems, its covariant components are not uniform, but space-varying along the curvilinear coordinates. In the Cartesian coordinate system, the projection of the integral form of the momentum balance equation in the physical direction $\vec{\lambda}$ reads

$$\begin{aligned} &\frac{d}{dt}\int_{\Delta V(t)} \vec{\lambda}\cdot\vec{u}dV + \int_{\Delta A(t)} \vec{\lambda}\cdot(\vec{u}\otimes(\vec{u}-\vec{w}_g)\cdot\hat{n})dA \\ &+\int_{\Delta A(t)} \left(G\eta + \frac{p_{dyn}}{\rho}\right)\vec{\lambda}\cdot(\underline{I}\cdot\hat{n})dA - \int_{\Delta A(t)} \frac{1}{\rho}\vec{\lambda}\cdot(\underline{R}\cdot\hat{n})dA = 0 \end{aligned} \tag{2.2}$$

where G is the acceleration due to the gravity, ρ is the fluid density, the tensors $\underline{I}$ and $\underline{R}$ are the identity tensor and the viscous stress tensor ($\underline{R} = 2\nu\underline{S}$ in which $\underline{S}$ is the strain rate tensor) that does not take into account the dynamic pressure p_{dyn}. H is the total water depth and it is given by the sum of the undisturbed water depth h and the free-surface elevation η: $H = h + \eta$ (see Fig. 2.1); the symbol $\otimes$ is the tensor product between vectors. The total pressure P is given by the sum of the dynamic pressure p_{dyn} and the hydrostatic pressure $\rho G(\eta - x^3)$

$$P = p_{dyn} + \rho G(\eta - x^3) \tag{2.3}$$

In order to write the Navier-Stokes equations in contravariant form on a time-dependent curvilinear coordinate system $(\xi^1, \xi^2, \xi^3, \tau)$, a particular time-dependent coordinate transformation is chosen. The particular time-dependent transformation from the Cartesian coordinate system to a curvilinear one is

$$\xi^1 = \xi^1(x^1, x^2, x^3) \quad \xi^2 = x^2(x^1, x^2, x^3) \quad \xi^3 = \frac{x^3 + h(x^1, x^2)}{H(x^1, x^2, t)} \quad \tau = t \tag{2.4}$$

ξ^1 and ξ^2 are the horizontal coordinates and are chosen to obtain a lateral boundary conforming grid. ξ^3 is the vertical coordinate that varies over time as a function of H; $\xi^3 = 1$ at the moving free surface and $\xi^3 = 0$ at the bottom. The

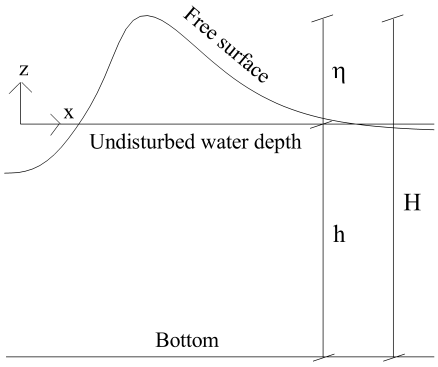

Figure 2.1: Reference coordinate system.

covariant and contravariant base vectors are given by

$$\vec{g}_{(l)} = \frac{\partial \vec{x}}{\partial \xi^l} \qquad \vec{g}^{(l)} = \frac{\partial \xi^l}{\partial \vec{x}} \qquad (l = 1, 2, 3) \tag{2.5}$$

The covariant and contravariant metric tensors are given by

$$g_{lm} = \vec{g}_{(l)} \cdot \vec{g}_{(m)} \qquad g^{lm} = \vec{g}^{(l)} \cdot \vec{g}^{(m)} \tag{2.6}$$

For this particular transformation, the Jacobian of the transformation is given by $\sqrt{g} = H\sqrt{g_0}$ where $\sqrt{g_0} = \vec{g}_{(1)} \cdot (\vec{g}_{(1)} \wedge \vec{g}_{(2)})$ (the symbol $\wedge$ is the vector product).

The Cartesian components of a generic vector $\vec{v}$ are related to the corresponding covariant and contravariant components in the curvilinear coordinate system [1] by

$$v_l = \vec{g}_{(l)} \cdot \vec{v} \qquad \vec{v} = v_l \vec{g}^{(l)} \qquad v^l = \vec{g}^{(l)} \cdot \vec{v} \qquad \vec{v} = v^l \vec{g}_{(l)} \tag{2.7}$$

In this coordinate transformation, the Cartesian components of the velocity vector of the moving coordinates is given by

$$\vec{w}_g = \frac{\partial \vec{x}}{\partial \tau} \tag{2.8}$$

In order to determine the $l - th$ contravariant component of vector $\vec{w}_g$, let start from the time partial derivative of the generic curvilinear coordinate

$$\frac{\partial \xi^l}{\partial \tau} = \frac{\partial \xi^l}{\partial t} + \frac{\partial \xi^l}{\partial \vec{x}} \cdot \frac{\partial \vec{x}}{\partial \tau} \tag{2.9}$$

In Eq. 2.9 the derivative $\partial \xi^l / \partial \tau = 0$, because ξ^l is not a function of τ ($\xi^l =$

$\xi^l(x^1, x^2, x^3, t)$). By considering Eq. 2.6, $\partial\xi^l/\partial\vec{x} = \vec{g}^{(l)}$ and that the scalar product in Eq. 2.8 produces w_g^l, the $l-th$ contravariant components of the moving coordinate velocity vector reads

$$w_g^l = -\frac{\partial \xi^l}{\partial t} \tag{2.10}$$

By using Eqs. 2.3 - 2.9, Eqs. 2.1 and 2.2 can be expressed in integral contravariant form as follow

$$\frac{d}{d\tau}\int_{\Delta V_1(\tau)} dV + \int_{\Delta A_1(\tau)} (u^m - w_g^m) n_m dA = 0 \tag{2.11}$$

$$\begin{aligned} &\frac{d}{d\tau}\int_{\Delta V_1(\tau)} u^l \lambda_l dV + \int_{\Delta A_1(\tau)} u^l (u^m - w_g^m)\lambda_l n_m dA \\ &+ \int_{\Delta A_1(\tau)} \left(G\eta + \frac{P_{dyn}}{\rho}\right) \underline{I}^{lm} \lambda_l n_m dA - \frac{1}{\rho}\int_{\Delta A_1(\tau)} \underline{R}^{lm} \lambda_l n_m dA = 0 \end{aligned} \tag{2.12}$$

In Eqs. 2.11 and 2.12, $\Delta V_1(\tau)$ is the time-varying control volume which at every instant τ coincides with the fluid material volume and $\Delta A_1(\tau)$ is the boundary surface of this control volume.

In this thesis, vector $\vec{\lambda}$ is given by the $l-th$ contravariant base vector at the center of the control volume, indicated by $\tilde{\vec{g}}^{(l)}$. The $m-th$ covariant component of $\tilde{\vec{g}}^{(l)}$, in Eq. 2.12, is given by

$$\lambda_m = \tilde{\vec{g}}^{(l)} \cdot \vec{g}_{(m)} \tag{2.13}$$

The identity tensor $\underline{I}^{lm}$ can be expressed by the contravariant metric coefficients as follow

$$\underline{I}^{lm} = g^{lm} \tag{2.14}$$

In curvilinear coordinate system, the time-varying control volume and its boundary surface, that lies on the coordinate surface in which ξ^α is constant, are expressed by

$$\begin{aligned} \Delta V_1(\tau) &= \int_{\Delta V_0} \sqrt{g} d\xi^1 d\xi^2 d\xi^3 \\ \Delta A_1^\alpha(\tau) &= \int_{\Delta A_0^\alpha} |\vec{g}_{(\beta)} \wedge \vec{g}_{(\gamma)}| d\xi^\beta d\xi^\gamma \end{aligned} \tag{2.15}$$

where ΔV_0 indicates the corresponding volume in the transformed space and ΔA_0^α is the corresponding area in the transformed space, which is defined as $\Delta A_0^\alpha =$

$\Delta\xi^\beta\Delta\xi^\gamma$ $(\alpha,\beta,\gamma = 1,2,3)$. Both the quantities are not time dependent.

The $m-th$ covariant component of the product between the unit vector which is normal to the infinitesimal surface on which ξ^α is constant and its area is given by

$$n_m dA = \vec{g}_{(m)} \cdot \vec{g}^{(\alpha)} H\sqrt{g_0} d\xi^\beta d\xi^\gamma \tag{2.16}$$

where α,β,γ are cyclic.

It is possible to write the Eqs. 2.11 and 2.12 in terms of conserved variables.

$$(Hu^m) \quad and \quad (H) \tag{2.17}$$

By using Eqs. 2.13-2.17 in Eqs. 2.11 and 2.12, the mass conservation equation and the momentum balance equation expressed in integral contravariant form on a time-dependent curvilinear coordinate system in terms of conserved variables H and Hu^m become

$$\begin{aligned} &\frac{d}{d\tau}\int_{\Delta V_0} H\sqrt{g_0} d\xi^1 d\xi^2 d\xi^3 \\ &+\sum_{\alpha=1}^{3}\left\{\int_{\Delta A_0^{\alpha+}} (Hu^\alpha - H\omega_g^\alpha)\sqrt{g_0} d\xi^\beta d\xi^\gamma - \right. \\ &\left.\int_{\Delta A_0^{\alpha-}} (Hu^\alpha - H\omega_g^\alpha)\sqrt{g_0} d\xi^\beta d\xi^\gamma\right\} = 0 \end{aligned} \tag{2.18}$$

$$
\begin{aligned}
&\frac{d}{d\tau}\int_{\Delta V_0}\tilde{\vec{g}}^{(l)}\cdot\vec{g}_{(m)}Hu^m\sqrt{g_0}d\xi^1d\xi^2d\xi^3\\
&+\sum_{\alpha=1}^{3}\left\{\int_{\Delta A_0^{\alpha+}}\tilde{\vec{g}}^{(l)}\cdot\vec{g}_{(m)}\left[Hu^m\left(\frac{Hu^\alpha}{H}-\omega_g^\alpha\right)\right]\sqrt{g_0}d\xi^\beta d\xi^\gamma-\right.\\
&\left.\int_{\Delta A_0^{\alpha-}}\tilde{\vec{g}}^{(l)}\cdot\vec{g}_{(m)}\left[Hu^m\left(\frac{Hu^\alpha}{H}-\omega_g^\alpha\right)\right]\sqrt{g_0}d\xi^\beta d\xi^\gamma\right\}\\
&+\sum_{\alpha=1}^{3}\left\{\int_{\Delta A_0^{\alpha+}}\tilde{\vec{g}}^{(l)}\cdot\vec{g}_{(m)}\left[g^{m\alpha}\left(G\eta+\frac{p_{dyn}}{\rho}\right)\right]H\sqrt{g_0}d\xi^\beta d\xi^\gamma-\right.\\
&\left.\int_{\Delta A_0^{\alpha-}}\tilde{\vec{g}}^{(l)}\cdot\vec{g}_{(m)}\left[g^{m\alpha}\left(G\eta+\frac{p_{dyn}}{\rho}\right)\right]H\sqrt{g_0}d\xi^\beta d\xi^\gamma\right\}\\
&-\frac{1}{\rho}\sum_{\alpha=1}^{3}\left\{\int_{\Delta A_0^{\alpha+}}\tilde{\vec{g}}^{(l)}\cdot\vec{g}_{(m)}R^{\alpha m}H\sqrt{g_0}d\xi^\beta d\xi^\gamma-\right.\\
&\left.\int_{\Delta A_0^{\alpha+}}\tilde{\vec{g}}^{(l)}\cdot\vec{g}_{(m)}R^{\alpha m}H\sqrt{g_0}d\xi^\beta d\xi^\gamma\right\}=0
\end{aligned}
\tag{2.19}
$$

In Eq. 2.19, $R^{\alpha m}=2\mu S^{\alpha m}$ are the contravariant components of the stress tensor without the pressure term: $S^{\alpha m}$ are the contravariant components of the strain rate tensor and μ is the dynamic viscosity.

Let define the cell-averaged values in the transformed space

$$
\begin{aligned}
\overline{H}&=\frac{1}{\Delta A_0^3\sqrt{g_0}}\int_{\Delta A_0^3}H\sqrt{g_0}d\xi^1d\xi^2\\
\overline{Hu^l}&=\frac{1}{\Delta V_0\sqrt{g_0}}\int_{\Delta V_0}\tilde{\vec{g}}^{(l)}\cdot\vec{g}_{(m)}Hu^m\sqrt{g_0}d\xi^1d\xi^2d\xi^3
\end{aligned}
\tag{2.20}
$$

By using Eqs. 2.20 and by substituting $\eta(x^1,x^2,t)=H(x^1,x^2,t)-h(x^1,x^2)$ in Eq. 2.19, Eqs. 2.18 and 2.19 become

$$
\begin{aligned}
&\frac{\partial\overline{H}}{\partial\tau}=\\
&-\frac{1}{\Delta A_0^3\sqrt{g_0}}\left\{\int_0^1\int_{\Delta\xi_0^{1+}}Hu^1d\xi^2d\xi^3-\int_0^1\int_{\Delta\xi_0^{1-}}Hu^1d\xi^2d\xi^3\right.\\
&+\int_0^1\int_{\Delta\xi_0^{2+}}Hu^2d\xi^1d\xi^3-\int_0^1\int_{\Delta\xi_0^{2-}}Hu^2d\xi^1d\xi^3\\
&+\left(\int\int_{\Delta A_0^3}(Hu^3-Hw_g^3)\sqrt{g_0}d\xi^1d\xi^2\right)_{\xi^3=1}\\
&\left.-\left(\int\int_{\Delta A_0^3}(Hu^3-Hw_g^3)\sqrt{g_0}d\xi^1d\xi^2\right)_{\xi^3=0}\right\}
\end{aligned}
\tag{2.21}
$$

$$
\begin{aligned}
&\frac{\partial \overline{Hu^l}}{\partial \tau} = \\
&-\frac{1}{\Delta V_0 \sqrt{g_0}} \sum_{\alpha=1}^{3} \left\{ \int_{\Delta A_0^{\alpha+}} \tilde{\vec{g}}^{(l)} \cdot \vec{g}_{(m)} \left[Hu^m \left(\frac{Hu^\alpha}{H} - \omega_g^\alpha \right) \right] \sqrt{g_0} d\xi^\beta d\xi^\gamma - \right. \\
&\left. \int_{\Delta A_0^{\alpha-}} \tilde{\vec{g}}^{(l)} \cdot \vec{g}_{(m)} \left[Hu^m \left(\frac{Hu^\alpha}{H} - \omega_g^\alpha \right) \right] \sqrt{g_0} d\xi^\beta d\xi^\gamma \right\} \\
&-\frac{1}{\Delta V_0 \sqrt{g_0}} \sum_{\alpha=1}^{3} \left\{ \int_{\Delta A_0^{\alpha+}} \tilde{\vec{g}}^{(l)} \cdot \vec{g}^{(\alpha)} G(H-h) H \sqrt{g_0} d\xi^\beta d\xi^\gamma - \right. \\
&\left. \int_{\Delta A_0^{\alpha-}} \tilde{\vec{g}}^{(l)} \cdot \vec{g}^{(\alpha)} G(H-h) H \sqrt{g_0} d\xi^\beta d\xi^\gamma \right\} \\
&-\frac{1}{\rho \Delta V_0 \sqrt{g_0}} \sum_{\alpha=1}^{3} \left\{ \int_{\Delta A_0^{\alpha+}} \tilde{\vec{g}}^{(l)} \cdot \vec{g}^{(\alpha)} p_{dyn} H \sqrt{g_0} d\xi^\beta d\xi^\gamma - \right. \\
&\left. \int_{\Delta A_0^{\alpha-}} \tilde{\vec{g}}^{(l)} \cdot \vec{g}^{(\alpha)} p_{dyn} H \sqrt{g_0} d\xi^\beta d\xi^\gamma \right\} \\
&+\frac{1}{\rho \Delta V_0 \sqrt{g_0}} \sum_{\alpha=1}^{3} \left\{ \int_{\Delta A_0^{\alpha+}} \tilde{\vec{g}}^{(l)} \cdot \vec{g}_{(m)} R^{\alpha m} H \sqrt{g_0} d\xi^\beta d\xi^\gamma - \right. \\
&\left. \int_{\Delta A_0^{\alpha+}} \tilde{\vec{g}}^{(l)} \cdot \vec{g}_{(m)} R^{\alpha m} H \sqrt{g_0} d\xi^\beta d\xi^\gamma \right\}
\end{aligned}
\tag{2.22}
$$

In Eq. 2.21, w_g^1 and w_g^2 are zero, because lateral surfaces of the control volume are fixed; $u^3 - w_g^3$ is zero because the bottom ($\xi^3 = 0$) is a fixed closed boundary and the free surface ($\xi^3 = 1$) moves with the same normal velocity of the water.

Eqs. 2.21 and 2.22 are respectively the governing equations for the conserved variables in integral contravariant form on a time-dependent curvilinear coordinate system.

The advancing in time of the numerical solution is obtained by a predictor-corrector method, that takes into account the dynamic component of the pressure. In the predictor step, the momentum balance equation expressed in terms of the conserved variables (Hu^l) is solved by a conservative scheme devoid of the dynamic pressure component. The divergence of the predictor field $(Hu^l)^*$ is used as the known term of a Poisson-like equation by which it is possible to define the scalar potential Ψ. In this way, a corrector field expressed in term of the conserved variable is directly obtained, $(Hu^l)^c$.

2.3 Poisson-like equation

A Poisson-like equation is used to find a scalar potential Ψ, by which takes into account the dynamic pressure and correct the predictor field. Eq. 2.22 is solved neglecting the dynamic pressure term and gives rise to the conserved predictor variable, $\overline{Hu^l}^*$. This predictor field is not divergence free. The gradient of the scalar potential Ψ gives rise to the corrected conserved variable, $\overline{Hu^l}^c$.

The Poisson-like equation expressed in contravariant form on a time-dependent curvilinear coordinate system is given by

$$\frac{\partial[\frac{g^{ls}\partial\Psi}{\partial s}H\sqrt{g_0}]}{\partial\xi^l} = -\frac{\partial(\overline{Hu^l})^*\sqrt{g_0}}{\partial\xi^l} \tag{2.23}$$

Eq. 2.23 can be expressed in integral contravariant form as follow

$$\begin{aligned}&\sum_{\alpha=1}^{3}\left\{\int_{\Delta A_0^{\alpha^+}}\frac{\partial\Psi^s}{\partial\xi^m}g^{\alpha m}H\sqrt{g_0}d\xi^\beta d\xi^\gamma - \int_{\Delta A_0^{\alpha^-}}\frac{\partial\Psi^s}{\partial\xi^m}g^{\alpha m}H\sqrt{g_0}d\xi^\beta d\xi^\gamma\right\}\\ &=\sum_{\alpha=1}^{3}\left\{\int_{\Delta A_0^{\alpha^+}}(\overline{Hu}^{\alpha(s)})^*\sqrt{g_0}d\xi^\beta d\xi^\gamma - \int_{\Delta A_0^{\alpha^-}}(\overline{Hu}^{\alpha(s)})^*\sqrt{g_0}d\xi^\beta d\xi^\gamma\right\}\end{aligned} \tag{2.24}$$

Once Eq. 2.24 is solved, the corrector field can be calculated as follow

$$\overline{Hu^l}^c = H\frac{g^{ls}\partial\Psi}{\partial s} \tag{2.25}$$

Chapter 3

Numerical scheme

In this thesis the equations of motion are solved by using a new finite-volume shock-capturing numerical scheme, which use a Riemann solver.

In recent three-dimensional free-surface models [9, 14, 20, 47], the wave breaking is simulated as a shock wave, i.e. a discontinuity of the equations of motion solution. It is known that the numerical simulation of a shock wave presents considerable difficulties. The numerical approximation of a shock wave may have a strong strength (i.e. erroneous ratio between the value of the quantities before and after the shock wave) and an erroneous propagation speed, and thus it can mistake the position of the discontinuity at a given time.

As demonstrated by [13, 26] the numerical models present in the literature [9, 14, 20, 47] are affected by some drawbacks: during the shoaling process the wave height increase is underestimated, the initial wave breaking point is not correctly located and the wave height decrease in the surf zone is not correctly evaluated, with consequent underestimation of the wave-induced currents. The main cause of these drawbacks is due to the excess of the kinetic energy dissipation of the ensemble-averaged motion in the numerical solution that is not introduced by the adopted turbulence model, but by the low order shock-capturing numerical scheme. [9, 14, 20, 47] use shock-capturing finite-volume numerical scheme that adopts 2^{nd} order Total Variation Diminishing (TVD) reconstructions technique and approximate Riemann solvers. In order to overcome these drawbacks and correctly represent the wave height evolution, wave breaking dynamics in the surf zone, and wave-induced coastal currents, the authors use fine grids, especially in the horizontal directions, that limit their application mainly to laboratory-scale

case studies.

To reduce the kinetic energy dissipation of the ensemble-averaged motion, that is introduced in the numerical solution by the low-order numerical scheme Cannata et al [13, 26] increased the order of accuracy of the numerical scheme ensuring good non-oscillatory properties. By using this high-order numerical scheme it is possible to leave the task of dissipating the kinetic energy of the ensemble-averaged motion to the turbulence model. The new numerical scheme proposed by [13, 26, 51] solves the three-dimensional Navier-Stokes equations written in integral contravariant form expressed in a generalized time-dependent curvilinear coordinate system, in which the vertical coordinate moves following the free surface. This numerical model is based on two elements of novelty. The first element of novelty is related to the reconstruction technique for the point values of the conserved variables on the cell faces. The numerical scheme is based on a new fifth-order reconstruction technique, called Wave-Targeted Essentially Non-Oscillatory (WTENO). This reconstruction technique uses different polynomials defined on contiguous cells, and also uses a so-called cut-off function (which varies in space and time) that depends on the polynomial regularity, and on the definition of a dynamic threshold (which also varies in space and time), which is a function of the steepness of the wave fronts. This reconstruction technique ensures high-order of accuracy, good non-oscillatory properties and avoids excessive dissipation of the kinetic energy of the ensemble-averaged motion due to the TVD reconstruction technique. The second element of novelty is the use of an exact solution of the Riemann problem for the time advancing of the point values of the conserved variables on the cell faces. By using the new high-order numerical scheme, it is possible to leave the task of dissipating the kinetic energy of the ensemble-averaged motion to the turbulence model.

The chapter is organized as follow: in Section 3.1, the finite volume discretization of the motion equations is introduced; in Section 3.2, the numerical scheme is presented; in Section 3.3, the new high-order WTENO reconstruction technique is presented; in Section 3.4 the exact solution for the Riemann problem is shown; in Section 3.5 the fractional step methods procedure is shown.

3.1 Finite volume discretization

3.1.1 Discretized equations of motion

The physical domain is divided into $N \times M \times O$ hexahedral cells $I_{i,j,k}$ (where $i = 1 - N$, $j = 1 - M$ and $k = 1 - M$), bounded by cell faces that lie on curvilinear coordinate surfaces (defined by indexes $i \pm \frac{1}{2}$, $j \pm \frac{1}{2}$ and $k \pm \frac{1}{2}$). The conserved variables are defined at the center of each cell. By integrating Eq. 2.21 over the water column and discretizing over space the obtained equation, the rate of change of the cell-averaged water depth, $(\overline{H})_{i,j,k}$, reads

$$\begin{aligned}(\overline{H})_{i,j} = &-\frac{1}{(\Delta\xi^1\Delta\xi^2\sqrt{g_0})_{i,j}} \\ &\left\{\left[(Hu^1\sqrt{g_0}\Delta\xi^2\Delta\xi^3)_{i+\frac{1}{2},j,k} - (Hu^1\sqrt{g_0}\Delta\xi^2\Delta\xi^3)_{i-\frac{1}{2},j,k}\right]\right. \\ &\left.+\left[(Hu^2\sqrt{g_0}\Delta\xi^1\Delta\xi^3)_{i,j+\frac{1}{2},k} - (Hu^2\sqrt{g_0}\Delta\xi^1\Delta\xi^3)_{i,j-\frac{1}{2},k}\right]\right\}\end{aligned} \tag{3.1}$$

By discretizing over space Eq. 2.22, the rate of change of the cell-averaged conserved variable $(\overline{Hu^l})_{i,j,k}$ reads

$$\begin{aligned}\frac{(\overline{Hu^l})_{i,j}}{\partial t} = &-\left(\frac{\tilde{\bar{g}}^{(l)}}{\Delta\xi^1\Delta\xi^2\Delta\xi^3}\sqrt{g_0}\right)_{i,j,k} \\ &\left\{\left[\left(Hu^m\frac{Hu^1}{H} + \left(GH - Gh + \frac{p_{dyn}}{\rho}\right)Hg^{m1}\sqrt{g_0}\right)\Delta\xi^2\Delta\xi^3\right]_{1+\frac{1}{2},j,k}\right. \\ &-\left[\left(Hu^m\frac{Hu^1}{H} + \left(GH - Gh + \frac{p_{dyn}}{\rho}\right)Hg^{m1}\sqrt{g_0}\right)\Delta\xi^2\Delta\xi^3\right]_{1-\frac{1}{2},j,k} \\ &+\left[\left(Hu^m\frac{Hu^2}{H} + \left(GH - Gh + \frac{p_{dyn}}{\rho}\right)Hg^{m2}\sqrt{g_0}\right)\Delta\xi^1\Delta\xi^3\right]_{1,j+\frac{1}{2},k} \\ &-\left[\left(Hu^m\frac{Hu^2}{H} + \left(GH - Gh + \frac{p_{dyn}}{\rho}\right)Hg^{m2}\sqrt{g_0}\right)\Delta\xi^1\Delta\xi^3\right]_{1,j-\frac{1}{2},k} \\ &+\left[\left(Hu^m\left(\frac{Hu^3}{H} - \omega_g^3\right) + \left(GH - Gh + \frac{p_{dyn}}{\rho}\right)Hg^{m3}\sqrt{g_0}\right)\Delta\xi^1\Delta\xi^2\right]_{1,j,k+\frac{1}{2}} \\ &-\left[\left(Hu^m\left(\frac{Hu^3}{H} - \omega_g^3\right) + \left(GH - Gh + \frac{p_{dyn}}{\rho}\right)Hg^{m3}\sqrt{g_0}\right)\Delta\xi^1\Delta\xi^2\right]_{1,j,k-\frac{1}{2}} \\ &-\frac{1}{\rho}\left[\left(R^{m1}H\sqrt{g_0}\Delta\xi^2\Delta\xi^3\right)\right]_{i+\frac{1}{2},j,k} - \left[\left(R^{m1}H\sqrt{g_0}\Delta\xi^2\Delta\xi^3\right)\right]_{i-\frac{1}{2},j,k} \\ &-\frac{1}{\rho}\left[\left(R^{m2}H\sqrt{g_0}\Delta\xi^1\Delta\xi^3\right)\right]_{i,j+\frac{1}{2},k} - \left[\left(R^{m2}H\sqrt{g_0}\Delta\xi^1\Delta\xi^3\right)\right]_{i,j-\frac{1}{2},k} \\ &\left.-\frac{1}{\rho}\left[\left(R^{m3}H\sqrt{g_0}\Delta\xi^1\Delta\xi^2\right)\right]_{i,j,k+\frac{1}{2}} - \left[\left(R^{m3}H\sqrt{g_0}\Delta\xi^1\Delta\xi^2\right)\right]_{i,j,k-\frac{1}{2}}\right\}\end{aligned} \tag{3.2}$$

The integral form of the Poisson-like equation, Eq. 2.24, is solved on a control volume $\Delta V_{i,j,k+\frac{1}{2}}$, as shown in Fig. 3.1. This control volume is defined at the center of the upper faces of each grid cells, while the velocity field is calculated at the center of a control volume $\Delta V_{i,j,k}$.

By discretizing over space Eq. 2.23, the Poisson-like equation can be rewritten as

$$\begin{aligned}
&\left[\left(\frac{\partial\Psi^{(s)}}{\partial\xi^m}g^{m1}\sqrt{g_0}\Delta\xi^2\Delta\xi^3\right)_{i+\frac{1}{2},j,k+\frac{1}{2}} - \left(\frac{\partial\Psi^{(s)}}{\partial\xi^m}g^{m1}\sqrt{g_0}\Delta\xi^2\Delta\xi^3\right)_{i-\frac{1}{2},j,k+\frac{1}{2}}\right] \\
&+\left[\left(\frac{\partial\Psi^{(s)}}{\partial\xi^m}g^{m2}\sqrt{g_0}\Delta\xi^1\Delta\xi^3\right)_{1,j+\frac{1}{2},k+\frac{1}{2}} - \left(\frac{\partial\Psi^{(s)}}{\partial\xi^m}g^{m2}\sqrt{g_0}\Delta\xi^1\Delta\xi^3\right)_{1,j-\frac{1}{2},k+\frac{1}{2}}\right] \\
&+\left[\left(\frac{\partial\Psi^{(s)}}{\partial\xi^m}g^{m3}\sqrt{g_0}\Delta\xi^1\Delta\xi^2\right)_{1,j,k+1} - \left(\frac{\partial\Psi^{(s)}}{\partial\xi^m}g^{m3}\sqrt{g_0}\Delta\xi^1\Delta\xi^2\right)_{1,j,k}\right] = \\
&-\Big\{\left[\left(Hu^{1(s)}\right)^*\sqrt{g_0}\Delta\xi^2\Delta\xi^3\right]_{i+\frac{1}{2},j,k+\frac{1}{2}} - \left[\left(Hu^{1(s)}\right)^*\sqrt{g_0}\Delta\xi^2\Delta\xi^3\right]_{i-\frac{1}{2},j,k+\frac{1}{2}} \\
&+\left[\left(Hu^{2(s)}\right)^*\sqrt{g_0}\Delta\xi^1\Delta\xi^3\right]_{i,j+\frac{1}{2},k+\frac{1}{2}} - \left[\left(Hu^{2(s)}\right)^*\sqrt{g_0}\Delta\xi^1\Delta\xi^3\right]_{i,j-\frac{1}{2},k+\frac{1}{2}} \\
&+\left[\left(Hu^{3(s)}\right)^*\sqrt{g_0}\Delta\xi^1\Delta\xi^2\right]_{i,j,k+1} - \left[\left(Hu^{3(s)}\right)^*\sqrt{g_0}\Delta\xi^1\Delta\xi^2\right]_{i,j,k}\Big\}
\end{aligned} \tag{3.3}$$

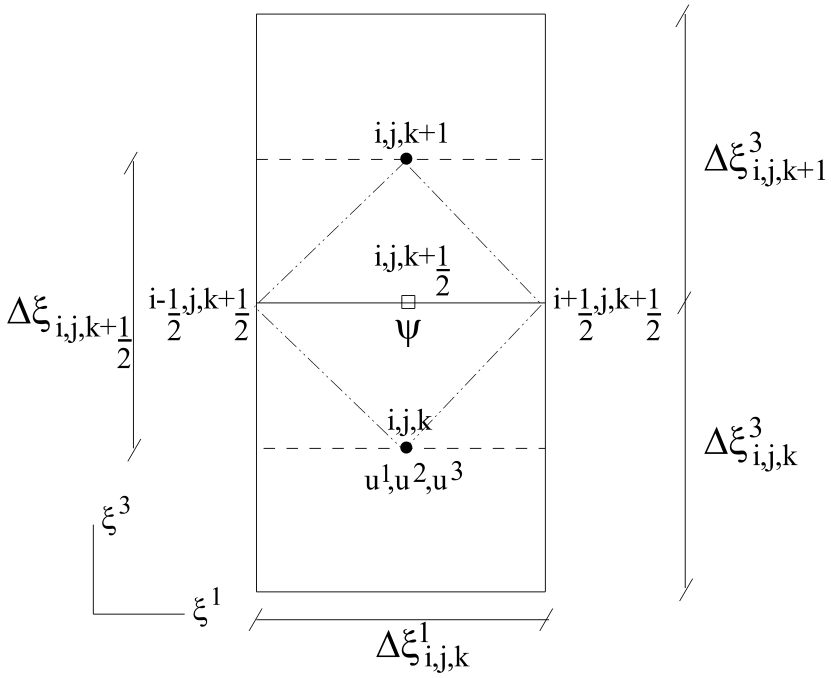

Figure 3.1: Control volume on which the Poisson-like equation is solved.

The contravariant components of the conserved corrector variables on the left hand side of Eq. 3.3, $\left(\frac{\partial \psi^{(s)}}{\partial \xi^m} g^m\right)_{i,j,k+\frac{1}{2}}$, are discretized in order to obtain a system of equations, where the matrix of coefficient has nineteen non-null diagonals

$$\begin{aligned} & a_1\Psi^{(s)}_{i,j-1,k-1} + a_2\Psi^{(s)}_{i-1,j-1,k-1} + a_3\Psi^{(s)}_{i,j,k-1} + a_4\Psi^{(s)}_{i+1,j,k-1} \\ & + a_5\Psi^{(s)}_{i,j+1,k-1} + a_6\Psi^{(s)}_{i-1,j-1,k} + a_7\Psi^{(s)}_{i,j-1,k} + a_8\Psi^{(s)}_{i+1,j-1,k} \\ & + a_9\Psi^{(s)}_{i-1,j,k} + a_{10}\Psi^{(s)}_{i,j,k} + a_{11}\Psi^{(s)}_{i+1,j,k} + a_{12}\Psi^{(s)}_{i-1,j+1,k} \\ & + a_{13}\Psi^{(s)}_{i,j+1,k} + a_{14}\Psi^{(s)}_{i+1,j+1,k} + a_{15}\Psi^{(s)}_{i,j-1,k+1} \\ & + a_{16}\Psi^{(s)}_{i-1,j,k+1} + a_{17}\Psi^{(s)}_{i,j,k+1} + a_{18}\Psi^{(s)}_{i+1,j,k+1} \\ & + a_{19}\Psi^{(s)}_{i,j+1,k+1} = Q_{i,j,k+\frac{1}{2}} \end{aligned} \tag{3.4}$$

where the term $Q_{i,j,k+\frac{1}{2}}$ is the divergence of the predictor conserved velocity (changed in sign).

3.1.2 Boundary conditions for the equations of motion

The kinematic condition at the free surface is given by

$$(u^3 - \omega_g^3)_{i,j,O+\frac{1}{2}} = 0 \tag{3.5}$$

This boundary condition is imposed on the upper faces $I_{i,j,O+\frac{1}{2}}$ (where O is the number of the computational cells in vertical direction) of the last computational grid cells. At the free surface, the zero-value condition of the Ψ potential is imposed

$$(\Psi^{(s)})_{i,j,O+\frac{1}{2}} = 0 \tag{3.6}$$

No slip-condition is imposed as the bottom boundary condition and it can be assigned by imposing null velocity contravariant components at the center of the first grid cell. The bottom boundary is defined at the center of the grid cells $I_{i,j,1}$. For the Poisson-like equation, the bottom boundary condition is given by imposing zero-value condition of the $\Psi^{(s)}$ potential derivative in the direction normal to the bottom.

$$\left(\frac{\partial \Psi^{(s)}}{\partial \xi^m} g^{m3}\right)_{i,j,1} = 0 \tag{3.7}$$

Such condition is equivalent to imposing the contravariant corrector velocity

component $u_c^{3(s)}$ to be null at the bottom. Consequently, the bottom boundary conditions for the velocity normal to the bottom are those assigned in the prediction field calculation

$$\left(u^{3(s)}\right)_{i,j,1} = \left(u^{*3(s)}\right)_{i,j,1} \tag{3.8}$$

At the lateral boundaries of the domain, a ghost cell is used. When the closed boundaries are used, a null derivative in the normal direction is assigned for the free-surface elevation and a null flux is imposed through the boundary. When the opened boundaries are used, a null derivative in the normal direction is imposed for the free-surface elevation and velocity components. The lateral boundaries for the Poisson-like equation are in the center of the grid cells of the lateral ghost cells of the momentum equation computational grid. The lateral boundary for the Poisson-like is obtained by imposing the $\Psi^{(s)}$ potential derivative as null in the direction normal to the boundary.

$$\left(\frac{\partial \Psi^{(s)}}{\partial \xi^m} g^{m1}\right)_{\frac{1}{2},j,k} = 0 \tag{3.9}$$

For the other lateral boundary, the same condition in Eq. 3.8 is given.

In Fig. 3.2, the computational domain is shown. The dashed line indicates the ghost cells, while the solid line indicates the calculation grid cells. At the center of each cell, the equations of motion are solved; at the upper faces of each cell the Poisson-like equation is solved. The bottom boundary is at the center of the grid cells $(I)_{i,j,1}$. The free-surface boundary is on the upper faces of each grid cells, $(I)_{i,j,O+\frac{1}{2}}$.

3.2 Numerical procedure

The numerical procedure can be divided into ten steps. In Fig. 3.3 the flow chart that describes the numerical procedure for the resolution of the integral contravariant form of the Navier-Stokes equations is shown.

1. The domain is divided into hexahedral grid cells. For each grid cell, $I_{i,j,k}$, the indexes i, j and k vary along the coordinate lines ξ^1, ξ^2 and ξ^3. Each cells are bounded by faces that lie on curvilinear coordinate surface, defined

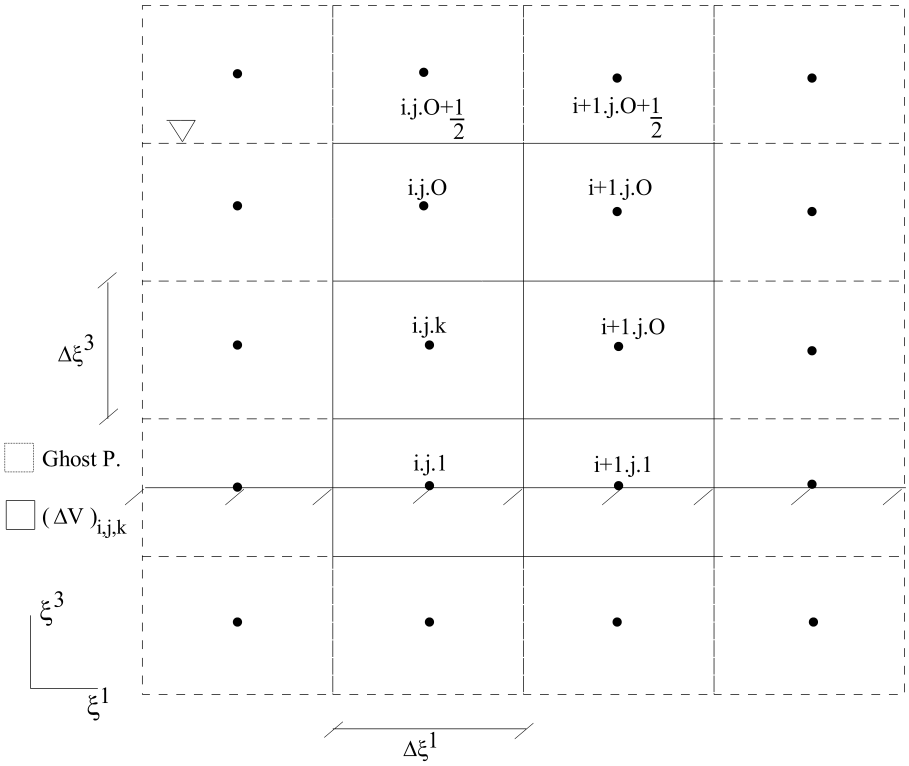

Figure 3.2: Grid cells of the computational domain. $---$ ghost cells and solid line computational grid cells.

by indexes $i \pm \frac{1}{2}, j \pm \frac{1}{2}, k \pm \frac{1}{2}$. Let be $(\overline{H})_{i,j}$ and $(\overline{Hu^l})_{i,j,k}$ the cell average values of the conserved variables H and Hu^l. The point value of a generic conserved variable defined at the centre of the computational cell face between the cells $I_{i,j,k}$ and $I_{i+1,j,k}$ is identified by $(\quad)_{i+\frac{1}{2},j,k}$. The point value of a generic conserved variable defined at the center of the opposite computational cell face between the cells $I_{i,j,k}$ and $I_{i-1,j,k}$ is identified by $(\quad)_{i-\frac{1}{2},j,k}$ (analogously for the other faces). To determine the point values at the centre of the computational cell faces, a high-order reconstruction technique is used starting from the cell average values of the same conserved variables known at time step t.

On a generic cell face $I_{i-\frac{1}{2},j,k}$, there are two point values of the conserved variables, $(\quad)^+_{i-\frac{1}{2},j,k}$ and $(\quad)^-_{i-\frac{1}{2},j,k}$, one coming from a polynomial centered in $I_{i,j,k}$ and the other coming from a polynomial centered in $I_{i-1,j,k}$.

2. The two point values of the conserved variables on each face of the cell $I_{i,j,k}$, given by the reconstructions, are the initial conditions for a local Riemann problem defined on each face. In order to solve a local Cartesian Riemann

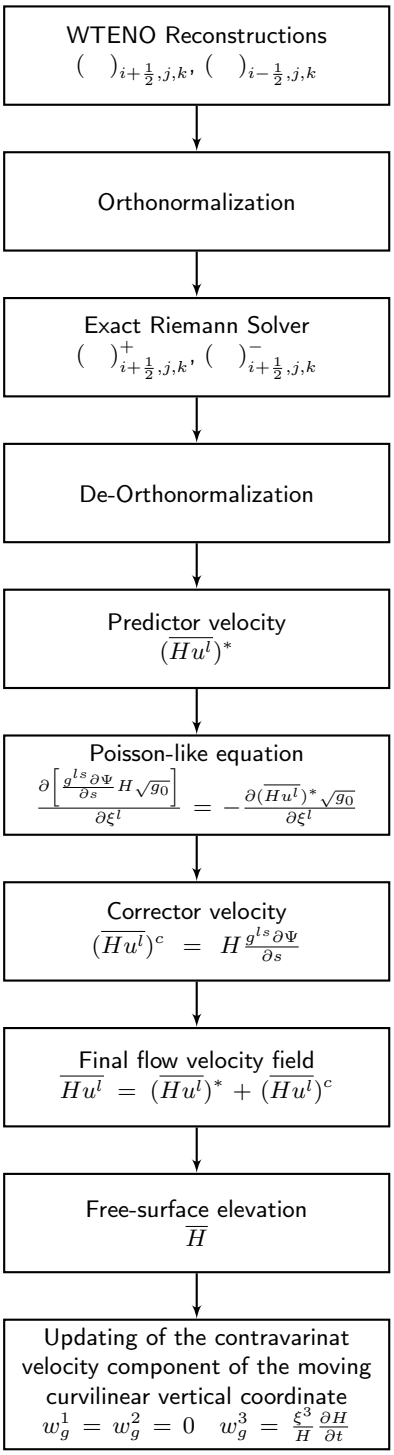

Figure 3.3: Flowchart of the numerical scheme.

problem, an orthonormalization procedure is made to transform the system of covariant and contravariant base vectors to a system of local orthonormal base vectors. The point values are expressed in terms of this system.

3. All the Riemann problems are solved by an exact procedure and the updated point values of the conserved variables are given on the cell faces.

4. The inverse transformation (de-orthonormalization procedure) is made to have the updated conserved variables expressed in terms of contravariant base vectors.

5. A predictor field of the cell average conserved variable $(\overline{Hu^l})^*$ is calculated by solving the momentum balance equation in which the dynamic pressure is not taken into account. This predictor field is not divergence-free and is used to calculate the known term of a Poisson-like equation.

6. The Poisson-like equation expressed in terms of the conserved variable $(\overline{Hu^l})^*$ is solved by a iterative multigrid method that use a combination of the four-colour Zebra and Gauss-Seidel line-by-line as a smoother.

7. The gradient of the scalar potential Ψ, obtained by solving the Poisson-like equation, is used to correct the field of conserved variables at the center of the computational grid cell and also at the center of the cell faces.

8. The sum of the predictor field $(\overline{Hu^l})^*$ and the corrector one $(\overline{Hu^l})^c$ gives the final cell average field of the conserved variable $\overline{Hu^l}$. This final field takes into account the dynamic pressure and is divergence-free.

9. The integration of the continuity equation over the water depth gives the updated cell averaged value of the water depth $\overline{H}$.

10. The contravariant velocity component of the moving curvilinear vertical coordinate is calculated once the free-surface position is updated.

3.3 WTENO Reconstructions

The shock-capturing numerical schemes used in the literature [9, 14, 20, 47] for the simulation of the hydrodynamic fields are based on the assumption that the

breaking wave can be represented by a discontinuity in the numerical solution (shock wave). In the proximity of the discontinuity, spurious oscillations can be generated and can propagate in the solution. The first−order numerical schemes, as demonstrated by Toro [67], ensure good non-oscillatory properties.

Many authors [9, 14, 20, 47] solve the three-dimensional motion equations by using shock-capturing finite volume numerical schemes that adopt (2^{nd} order) TVD reconstructions to reduce the spurious oscillations in the numerical solution. The 2^{nd} order TVD reconstructions ensure the maximum order of accuracy (2^{nd} order) where the solution is regular, while prevent the spurious oscillations where the solution is irregular by reducing the order of accuracy (1^{st} order) in the proximity of the discontinuity. It has been demonstrated by Cannata et al [13, 26] that the use of the TVD reconstructions introduces high numerical dissipation in the simulations and that, for this reason, the wave height is underestimated during the shoaling, the breaking point and the reduction of the wave height in the surf zone are not correctly evaluated.

To correctly simulate breaking waves and overcome the drawbacks introduced by the use of the low-order numerical schemes, the integral contravariant form of the Navier-Stokes equations is solved by using a new (5^{th} order) shock-capturing numerical technique [13, 26] for the reconstructions of the point values of the conserved variables at the centre of the computational cell faces. This technique starts form the Targeted Essentially Non-Oscillatory (TENO) technique, but is specifically designed for the three-dimensional simulation of the breaking waves and it is called WTENO by [13, 26].

The breaking waves are characterized by steep wave fronts where the turbulence phenomena are dominant. In correspondence of such wave fronts it is necessary that the reconstruction technique introduces low numerical energy dissipation to leave the task of dissipating the adequate amount of kinetic energy to the turbulence model. On the other hand in the surf zone on the wave tail (the part behind the wave front) the turbulence is negligible and the turbulence model should not dissipate kinetic energy. In this part of the wave it is necessary that the numerical scheme prevents the spurious oscillations produced on the free surface by introducing numerical energy dissipation.

In WTENO scheme the reconstruction of the point values of the conserved

variables at the centre of the computational cell faces of the generic computation grid cell $I_{i,j,k}$ is based on three elements. The first element consists in the definition of three different (2^{st} order) polynomials that are candidates for approximate the point value of the conserved variables in the computational grid cell $I_{i,j,k}$. The second element consists in the definition of a regularity function for each polynomial, which depends on the smoothness of the polynomials. The last element is the definition of a dynamic threshold, common to the three polynomials, that varies as a function of the smoothness and the steepness of the wave fronts. By comparing at every instant of the simulation and in each points of the domain the value of the regularity function with the dynamic threshold it can be deduced if one, two or three polynomials can be used to reconstruct the point values of the conserved variables. If just one or two polynomials participates to the reconstruction, the spatial order of accuracy is reduced and consequently the kinetic energy dissipation due to the numerical scheme increases.

The shock-capturing numerical scheme used in this thesis is based on a reconstruction procedure that is dynamically modified in every point and at every instant of the numerical simulations. On the steep wave fronts the numerical energy dissipation is reduced (in order to give the task of dissipating the kinetic energy to the turbulence model), while on the wave tails and the non-breaking wave fronts (where the kinetic energy dissipation is mainly located at the bottom, in the oscillating wave boundary layer) the adequate numerical energy dissipation is ensured.

The reconstruction procedure consists in calculating the point values of each conserved variable at the center of every computational cell face, starting from the integral of a given conserved variable over the cell volume. In the transformed space, used in this numerical model, the integral of the conserved variables over the cell volume is defined by three consecutive one-dimensional reconstructions, each one relative to a single coordinate line (dimension-by-dimension reconstruction).

The generic computational grid cell $I_{i,j,k}$, in the transformed space, denoted by ξ^1, ξ^2 and ξ^3 coordinates, has a regular and fixed shape and volume ($\Delta\xi^1\Delta\xi^2\Delta\xi^3$). The cell average conserved variable $\overline{Hu^l}$ can be indicated by this triple integral

$$\overline{Hu^l} = \frac{1}{\Delta\xi^1\Delta\xi^2\Delta\xi^3} \int_{\xi^3_{k-\frac{1}{2}}}^{\xi^3_{k+\frac{1}{2}}} \int_{\xi^2_{j-\frac{1}{2}}}^{\xi^2_{j+\frac{1}{2}}} \int_{\xi^1_{i-\frac{1}{2}}}^{\xi^1_{i+\frac{1}{2}}} Hu^l d\xi^1 d\xi^2 d\xi^3 \tag{3.10}$$

Let $(Hu^l)_{i+\frac{1}{2},j,k}$ and $(Hu^l)_{i-\frac{1}{2},j,k}$ be the point values of the conserved variable at the centre of the cell faces on which the ξ^1 coordinate is constant (placed at the side on which ξ^1 increases and decreases respectively). The reconstruction procedure is made up three different steps.

- Step 1: starting form the cell average values of the conserved variable $(\overline{Hu^l})_{i,j,k}$, the surf averaged value $(\widetilde{Hu^l})_{i,j,k}$, along the ξ^3 direction is given by

$$(\widetilde{Hu^l})_{i,j,k} = \frac{1}{\Delta\xi^2}\int_{\xi^2_{j-\frac{1}{2}}}^{\xi^2_{j+\frac{1}{2}}}\left[\frac{1}{\Delta\xi^1}\int_{\xi^1_{i-\frac{1}{2}}}^{\xi^1_{i+\frac{1}{2}}}\overline{Hu^l}(\xi^1,\xi^2,\xi^3)d\xi^1\right]d\xi^2 \tag{3.11}$$

- Step 2: starting from the surf averaged values $(\widetilde{Hu^l})_{i,j,k}$, the line averaged value $(\widehat{Hu^l})_{i,j,k}$, along the ξ^2 direction is given by

$$(\widehat{Hu^l})_{i,j,k} = \frac{1}{\Delta\xi^1}\int_{\xi^1_{i-\frac{1}{2}}}^{\xi^1_{i+\frac{1}{2}}}\widetilde{Hu^l}(\xi^1,\xi^2,\xi^3)d\xi^1 \tag{3.12}$$

- Step 3: starting form the line averaged values $(\widehat{Hu^l})_{i,j,k}$, the point values on the cell faces, $(Hu^l)_{i+\frac{1}{2},j,k}$ and $(Hu^l)_{i-\frac{1}{2},j,k}$, are reconstructed along the ξ^1 direction.

The value $(\widetilde{Hu^l})_{i,j,k}$ is reconstructed by a polynomial function $F_{i,j,k}(\xi^3)$ (where the indexes $(i,j,k=1,3)$ indicate the cell $I_{i,j,k}$ in which the polynomial is defined); in the other two directions the values are reconstructed by others polynomial functions

$$\begin{aligned}
(\widetilde{Hu^l})_{i,j,k} &= F_{i,j,k}(\xi^3)\\
(\widehat{Hu^l})_{i,j,k} &= F_{i,j,k}(\xi^2)\\
(Hu^l)_{1+\frac{1}{2},j,k} &= F_{i,j,k}(\xi^1_{i+\frac{1}{2}})\\
(Hu^l)_{1-\frac{1}{2},j,k} &= F_{i,j,k}(\xi^1_{i-\frac{1}{2}})
\end{aligned} \tag{3.13}$$

Each polynomial function is obtained by three different second-order polynomials defined on contiguous cells; for example the polynomial function for reconstruct the surface values is given by using these second-order polynomials

$P_{(p)i,j,k}(\xi^3)$ (where $p = -1, 0, +1$)

$$F_{i,j,k}(\xi^3) = \dot{\omega}_{-1} P_{(-1)i,j,k}(\xi^3) + \dot{\omega}_0 P_{(0)i,j,k}(\xi^3) + \dot{\omega}_1 P_{(1)i,j,k}(\xi^3) \tag{3.14}$$

In Eq. 3.14 the second-order polynomials are given by

$$P_{(p)i,j,k}(\xi^3) = a_{(p)i,j,k}(\xi^3)^2 + b_{(p)i,j,k}(\xi^3) + c_{(p)i,j,k} \tag{3.15}$$

The coefficients $a_{(p)i,j,k}$, $b_{(p)i,j,k}$ and $c_{(p)i,j,k}$ are determined by solving a linear system of three equations. Coming back to the Eq. 3.14 the coefficients $\dot{\omega}_p$ (with $p = -1, 0, +1$) are the non-linear weights and they are defined by

$$\dot{\omega}_p = \frac{\delta_p}{\sum_{p=-1}^{1} \delta_p C_p} \tag{3.16}$$

where C_p are the linear weights.

$$C_0 = 0.1 \qquad C_1 = 0.6 \qquad C_2 = 0.3 \tag{3.17}$$

The linear weights are calculated in such a way that the reconstruction in Eq. 3.14, obtained by three different second-order polynomials, is equal to a single fourth-order polynomials defined on 5 contiguous cells. The stencil made by these five contiguous cells is shown in Fig 3.4. Each second-order polynomial, shown in Fig. 3.4 is defined on a stencil of three contiguous cells.

δ_p are the cut-off functions adopted in TENO schemes [22, 54] and determine if one, two or three polynomials participate in the reconstruction (if all three polynomials are used the maximum order of accuracy (5^{th}) is reached)

$$\delta_p = \begin{cases} 0 & \Gamma_p < C_T \\ 1 & \Gamma_p \geq C_T \end{cases} \tag{3.18}$$

In Eq. 3.18 Γ_p is the regularity function and C_T is the dynamic threshold. At every instant of the simulation and at every point of the computational domain, the comparison between Γ_p and C_T determines how many polynomials are used

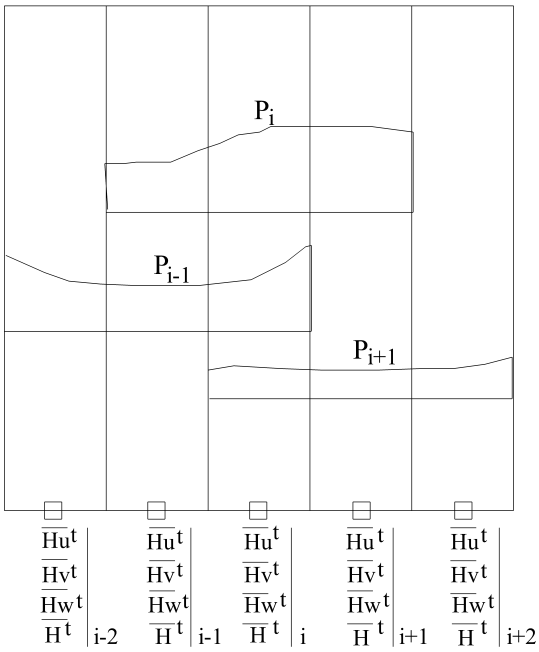

Figure 3.4: Stencil of contiguous cells for defining the polynomials $P_{(p)i,j,k}$.

in the reconstruction. Γ_p is defined as follow

$$\Gamma_p = \frac{\gamma_p}{\sum_{p=-1}^{1} \gamma_p} \tag{3.19}$$

γ_p depends on the smoothness indicator β_p of each polynomial and on the global smoothness indicator τ_p

$$\gamma_p = \left(C + \frac{\tau_p}{\beta_p + \epsilon} \right)^{\mu} \tag{3.20}$$

in which $\epsilon = 1e^{-40}$ is used just to prevent zero in the denominator, $\tau_p = \left|\beta_1 - \beta_{-1}\right|$ as adopted by [4], $\mu = 6$ and $C = 1$. β_p are computed by [36] and are related to the first and second derivative of the polynomial $P_{(p)i,j,k}(\xi^3)$; the value of β_p is high when the polynomial is irregular.

$$\beta_p = \int_{\xi^3_{k-\frac{1}{2}}}^{\xi^3_{k+\frac{1}{2}}} \Delta\xi^3 \left(\frac{\partial P_{(p)i,j,k}}{\partial \xi^3} \right)^2 d\xi^3 + \int_{\xi^3_{k-\frac{1}{2}}}^{\xi^3_{k+\frac{1}{2}}} (\Delta\xi^3)^2 \left(\frac{\partial^2 P_{(p)i,j,k}}{(\partial \xi^3)^2} \right)^2 d\xi^3 \tag{3.21}$$

By using the polynomials (Eq. 3.11) in Eq. 3.21, the smoothness indicators are given by

$$\begin{aligned}
\beta_0 &= \frac{13}{12}\left(\overline{u^l H_{i-2}} - 2\overline{u^l H_{i-1}} + \overline{u^l H_i}\right)^2 + \\
&\quad \frac{1}{4}\left(\overline{u^l H_{i-2}} - 4\overline{u^l H_{i-1}} + 3\overline{u^l H_i}\right)^2 \\
\beta_1 &= \frac{13}{12}\left(\overline{u^l H_{i-1}} - 2\overline{u^l H_i} + \overline{u^l H_{i+1}}\right)^2 + \frac{1}{4}\left(\overline{u^l H_{i-1}} - \overline{u^l H_{i+1}}\right)^2 \\
\beta_2 &= \frac{13}{12}\left(\overline{u^l H_i} - 2\overline{u^l H_{i+1}} + \overline{u^l H_{i+2}}\right)^2 + \\
&\quad \frac{1}{4}\left(3\overline{u^l H_i} - 4\overline{u^l H_{i+1}} + 3\overline{u^l H_{i+2}}\right)^2
\end{aligned} \tag{3.22}$$

The dynamic threshold C_T in WTENO reconstructions varies with space and time and is also a function of the regularity of the polynomials and the steepness of the wave front.

$$\begin{aligned}
C_T &= 10^{-n} \\
n &= B_l + (\theta + \theta_2)(B_h - B_l)
\end{aligned} \tag{3.23}$$

where $B_l = 1$ and $B_h = 7$ determine the minimum and maximum values of the exponent n. The parameter θ is the regularity function of each polynomial and is defined as follow

$$\theta = \frac{1}{1 + \frac{1}{d} max \frac{\tau_p}{\beta_p + \epsilon}} \qquad d = 10 \tag{3.24}$$

θ_2 in Eq. 3.23 is the parameter introduced in WTENO scheme to take into account the steepness of the wave front in order to increase the order of accuracy of the reconstructions on the breaking wave fronts and limit the spurious oscillations that can arise on the wave tails. Both the parameters influence the value of the exponent n: if n assumes low values the propensity of the technique to cut off one or two polynomials increases. θ_2 is given by

$$\theta_2 = \left\{ \frac{\frac{\partial \eta}{\partial t} - \left(\frac{\partial \eta}{\partial t}\right)^* + \left|\frac{\partial \eta}{\partial t} - \left(\frac{\partial \eta}{\partial t}\right)^*\right|}{2\left|\frac{\partial \eta}{\partial t} - \left(\frac{\partial \eta}{\partial t}\right)^*\right|} \right\} \left[\frac{\frac{\partial \eta}{\partial t}}{\left(\frac{\partial \eta}{\partial t}\right)^*} - 1 \right] \tag{3.25}$$

in which $\partial\eta/\partial t$ is the local time rate of change of the free-surface elevation, $(\partial\eta/\partial t)^*$ is a threshold value of $\partial\eta/\partial t$ used to distinguish the breaking wave fronts from the wave tails. The portion of the temporal variation of the free-surface characterized by positive values of $\partial\eta/\partial t$ is a wave front, on the other hand the negative values individuate the wave tails. Larger values of $\partial\eta/\partial t$ indi-

cate a higher steepness of the wave front and for this reason it possible to compare $\partial\eta/\partial t$ with the threshold $(\partial\eta/\partial t)^*$ to determine if a wave front is a breaking wave front. Kennedy et al [37] defines a wave breaking front for $(\partial\eta/\partial t)^* = 0.3\sqrt{gh}$. The first term of the Eq. 3.25 has the task to activate θ_2

$$\left\{ \frac{\frac{\partial\eta}{\partial t} - \left(\frac{\partial\eta}{\partial t}\right)^* + \left|\frac{\partial\eta}{\partial t} - \left(\frac{\partial\eta}{\partial t}\right)^*\right|}{2\left|\frac{\partial\eta}{\partial t} - \left(\frac{\partial\eta}{\partial t}\right)^*\right|} \right\} = \begin{cases} 0 & \frac{\partial\eta}{\partial t} \leq \left(\frac{\partial\eta}{\partial t}\right)^* \\ 1 & \frac{\partial\eta}{\partial t} > \left(\frac{\partial\eta}{\partial t}\right)^* \end{cases} \tag{3.26}$$

The second term of the Eq. 3.25 gives the magnitude to θ_2. θ_2 is activated on the breaking wave fronts $\partial\eta/\partial t > (\partial\eta/\partial t)^*$ and for this reason θ_2 differs from zero; on the wave tails and on the non-breaking fronts θ_2 is equal to zero.

Higher values of θ_2 produce increment the exponent n in Eq. 3.23, so C_T is reduced. For low values of C_T the propensity to cut off one or two polynomials is reduced. Consequently on the wave breaking fronts the numerical energy dissipation is reduced, because the high-order is reached. On non-breaking wave fronts and on the wave tails the reconstruction technique guarantees an adequate numerical dissipation to limit the spurious oscillations that can arise in the numerical solutions.

3.4 Exact Riemann Solver

The WTENO reconstructions presented in Section 3.3 give the point values of the conserved variables on the cell faces. On each cell face, there are two values of the conserved variables, one right and one left (H^+, H^-, Hu^{l+}, Hu^{l-}, Hv^{l+}, Hv^{l-}, Hw^{l+} and Hw^{l-} where the symbols + and − indicate respectively the right and left values of the conserved variables). To updating in time the point values of the conserved variables at the center of the cell faces an exact local Riemann solver is used. The two values on the cell faces that represent the discontinuity are the initial conditions for the Riemann problem.

In the literature [9, 14, 20, 47] the authors use an approximate Riemann solver. The main difference between the approximate and the exact Riemann solvers is the resolution of the contact wave in addition to the shock and rarefaction waves. By using the complete solution of the Riemann problem (and the 5^{th}-order reconstructions), it is possible to further limit the numerical energy dissipation.

In the following part the complete solution of the Riemann problem is explained.

The vector of the conserved variables is expressed with respect to a local Cartesian system of a base vectors (the horizontal coordinates, x^1 and x^2, are Cartesian and the vertical coordinate, ξ^3, varies overtime according to the σ-coordinate transformation). The integral contravariant form of the Navier-Stokes equations can be transformed in a conservative differential form on the local system of base vectors.

$$\begin{gathered}
\frac{\partial H}{\partial t}+\frac{\partial Hu}{\partial x^1}+\frac{\partial Hv}{\partial x^2}+\frac{\partial H(u^3-w_g^3)}{\partial \xi^3}=0 \\
\frac{\partial Hu}{\partial t}+\frac{\partial Huu}{\partial x^1}+\frac{\partial Huv}{\partial x^2}+\frac{\partial \frac{1}{2}GH^2}{\partial x^1}-GH\frac{\partial b}{\partial x^1}+\frac{\partial Hu(u^3-w_g^3)}{\partial \xi^3}=0 \\
\frac{\partial Hv}{\partial t}+\frac{\partial Hvu}{\partial x^1}+\frac{\partial Hvv}{\partial x^2}+\frac{\partial \frac{1}{2}GH^2}{\partial x^2}-GH\frac{\partial b}{\partial x^2}+\frac{\partial Hv(u^3-w_g^3)}{\partial \xi^3}=0 \\
\frac{\partial Hw}{\partial t}+\frac{\partial Hwu}{\partial x^1}+\frac{\partial Hwv}{\partial x^2}+\frac{\partial Hw(u^3-w_g^3)}{\partial \xi^3}=0
\end{gathered} \tag{3.27}$$

In Eqs. 3.27 the local Cartesian components of the vector of conserved variables are expressed by H, Hu, Hv and Hw; the contravariant component of the fluid velocity and the contravariant component of the moving coordinate are given respectively by u^3 and w_g^3. It is possible to rewrite the above system as follow

$$\frac{\partial \mathbf{U}}{\partial t}+\frac{\partial \mathbf{F}(\mathbf{U})}{\partial x^1}+\frac{\partial \mathbf{G}(\mathbf{U})}{\partial x^2}+\frac{\partial \mathbf{H}(\mathbf{U})}{\partial \xi^3}=\mathbf{S} \tag{3.28}$$

where

$$\begin{gathered}
\mathbf{U}=\begin{pmatrix} H \\ Hu \\ Hv \\ Hw \end{pmatrix}, \quad \mathbf{F}(\mathbf{U})=\begin{pmatrix} Hu \\ Huu+\frac{1}{2}GH^2 \\ Huv \\ Huw \end{pmatrix}, \quad \mathbf{G}(\mathbf{U})=\begin{pmatrix} Hv \\ Hvu \\ Hvv+\frac{1}{2}GH^2 \\ Hvw \end{pmatrix}, \\
\mathbf{H}(\mathbf{U})=\begin{pmatrix} 0 \\ Hu(u^3-w_g^3) \\ Hv(u^3-w_g^3) \\ Hw(u^3-w_g^3) \end{pmatrix}, \quad \mathbf{S}=\begin{pmatrix} -\frac{\partial H(u^3-\omega^3)}{\partial \xi^3} \\ GH\frac{\partial h}{\partial x^1} \\ GH\frac{\partial h}{\partial x^2} \\ 0 \end{pmatrix}
\end{gathered} \tag{3.29}$$

Three different exact Riemann problems each one relative to a single coordinate direction can be solved to obtain the solution of Eqs. 3.28, as indicated by

Toro [67]. In the following part the solution for the x^1-spit Riemann problem is shown.

The initial value problem is given by

$$\begin{cases} \frac{\partial \mathbf{W}}{\partial t} + \frac{\partial \mathbf{F}(\mathbf{W})}{\partial x^1} = 0 \\ \mathbf{W}(x,0) = \begin{cases} \mathbf{W}_L \; if \; x^1 < 0 \\ \mathbf{W}_R \; if \; x^1 > 0 \end{cases} \end{cases} \tag{3.30}$$

where

$$\mathbf{W}_L = \begin{pmatrix} H_L \\ H_L u_L \\ H_L v_L \\ H_L w_L \end{pmatrix}, \qquad \mathbf{W}_R = \begin{pmatrix} H_R \\ H_R u_R \\ H_R v_R \\ H_R w_R \end{pmatrix}, \qquad \mathbf{F}(\mathbf{W}) = \begin{pmatrix} Hu \\ Huu + \frac{1}{2}GH^2 \\ Huv \\ Huw \end{pmatrix} \tag{3.31}$$

where $\mathbf{W}_L$ and $\mathbf{W}_R$ are the vectors of the initial conditions ($\mathbf{W} = (H, u, v, w)$) on the left and right side of the cell face which in the local system of coordinates is places at $x = 0$; $\mathbf{F}(\mathbf{W})$ is the vector of the fluxes in x^1 direction. It is possible to define four constant state ($\mathbf{W}_L$, $\mathbf{W}_{stL}$, $\mathbf{W}_{stR}$ and $\mathbf{W}_R$) determined by the three eigenvalues ($e_1 = u - a, \quad e_2 = u, \quad e_3 = u + a$ where $a = \sqrt{Gh}$ by recalling that h is the still water depth) that is associated to three waves. The solution is unknown in the star region (indicated by the subscript st) that is the region between the left and right waves and it is influenced by the interaction of $\mathbf{W}_L$ and $\mathbf{W}_R$. Across the left and right waves, H and u change, while v and w remain constant; across the middle wave v and w change discontinuously, while H and u remaining constant. The left and right waves are determined according to the following conditions

$$\begin{gathered} H_{st} > H_L \; left \; shock \; wave \\ H_{st} \leq H_L \; left \; rarefaction \; wave \\ H_{st} > H_R \; right \; shock \; wave \\ H_{st} \leq H_R \; right \; rarefaction \; wave \end{gathered} \tag{3.32}$$

The values of H_{st} and u_{st} are not influenced by the tangential velocity com-

ponents, because the left and right waves are not influenced too. Obtaining a non-linear algebraic equation for H_{st} is the first step of the procedure, for this reason u_{st} should be connected to the left and right values of H by two function: $f_L(H, H_L)$ and $f_R(H, H_R)$. The solution for H_{st} is given by the root of the following non-linear algebraic equation

$$fun(H_{st}) \equiv fun_L(H_{st}, H_L) + fun_R(H_{st}, H_R) + u_R - u_L = 0 \tag{3.33}$$

where $fun_L(H_{st}, H_L)$ and $fun_R(H_{st}, H_R)$ are functions defined by using the Rankine-Hugoniot conditions[1] for a shock wave and Riemann invariants[2] for a rarefaction wave

$$\begin{aligned} fun_L &= \begin{cases} 2(\sqrt{GH_{st}} - \sqrt{GH_L}),\ if\ H_{st} \leq H_L\ (rarefaction\ wave) \\ (H_{st} + H_L)\sqrt{\frac{1}{2}G\frac{(H_{st}-H_L)}{H_{st}H_L}},\ if\ H_{st} > H_L\ (shock\ wave) \end{cases} \\ fun_R &= \begin{cases} 2(\sqrt{GH_{st}} - \sqrt{GH_R}),\ if\ H_{st} \leq H_R\ (rarefaction\ wave) \\ (H_{st} + H_R)\sqrt{\frac{1}{2}G\frac{(H_{st}-H_R)}{H_{st}H_R}},\ if\ H_{st} > H_R\ (shock\ wave) \end{cases} \end{aligned} \tag{3.34}$$

Only for the following conditions $H_{st} < H_{min}$; $H_{min} \leq H_{st} \leq H_{max}$; $H_{st} > H_{max}$ (where $H_{min} = min(H_L, H_R)$ and $H_{max} = max(H_L, H_R)$), the solution for H_{st} has physical meaning, because $H_{st} > 0$. The solution for Eq. 3.33 depends on $\Delta u = u_R - u_L$. If the following depth positive condition is fulfilled, H_{st} will be positive: $2(a_L + a_R) > u_R - u_L$ where $a = \sqrt{Gh}$.

If $f(H_{min}) > 0$, the left and right waves are rarefaction waves and $f(H_{st})$ becomes

$$2(a_{st} - a_L) + 2(a_{st} - a_R) + u_R - u_L = 0 \tag{3.35}$$

The solution for a_{st} and u_{st}

$$\begin{aligned} a_{st} &= \frac{1}{2}(a_L + a_R) - \frac{1}{4}(u_R - u_L) \\ u_{st} &= \frac{1}{2}(u_L + a_R) + a_L - a_R \end{aligned} \tag{3.36}$$

Newton-Raphson iterative scheme is used to numerically solve the other cases of Eq. 3.33 for H_{st}.

[1] see AppendixA
[2] see AppendixB

The solution for u_{st} in the star region is calculated by using H_{st} as follow

$$u_{st} = \frac{1}{2}(u_L + u_R) + \frac{1}{2}\left[f_R(H_{st}, H_R) - f_L(H_{st}, H_L)\right] \tag{3.37}$$

By comparing H_{st} with h_L and h_R it is possible to understand if the wave is a shock wave or rarefaction wave as shown in Eq. 3.32 and so find the complete solution of the problem.

- If $H_{st} > H_L$, the left wave is a shock wave with speed S_L given by

$$\begin{aligned} S_L &= u_L - a_L q_L \\ q_L &= \sqrt{\frac{\frac{1}{2}(H_{st} + H_L)H_{st}}{H_L^2}} \end{aligned} \tag{3.38}$$

- If $H_{st} \leq H_L$, the left wave is a rarefaction wave, for which the speed of the head S_{HL} and tail S_{TL} of the wave are

$$\begin{aligned} S_{HL} &= u_L - a_L \\ S_{TL} &= u_{st} - a_{st} \end{aligned} \tag{3.39}$$

  In this case the solution inside the rarefaction wave is given by

$$W_{Lfan} = \begin{cases} a = \frac{1}{3}\left(u_L + 2a_L - \frac{x^1}{t}\right) \\ u = \frac{1}{3}\left(u_L + 2a_L - \frac{2x^1}{t}\right) \end{cases} \tag{3.40}$$

  In Fig. 3.5 the structure of the complete solution is shown for the two possible waves on the left side of the shear wave $x/t = u_{st}$ (that is the middle wave across which the tangential velocity components change discontinuously): in the first figure the left wave is a shock wave and in the second figure the left wave is a rarefaction wave.

- If $H_{st} > H_R$ the right wave is a shock, with speed S_R

$$\begin{aligned} S_R &= u_R + a_R q_R \\ q_R &= \sqrt{\frac{\frac{1}{2}(H_{st} + H_R)H_{st}}{H_R^2}} \end{aligned} \tag{3.41}$$

- If $H_{st} \leq H_R$ the right wave is a rarefaction wave for which the speed on the

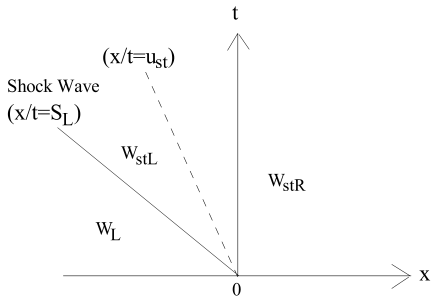

(a) Solution for a shock left wave $H_{st} > H_L$.

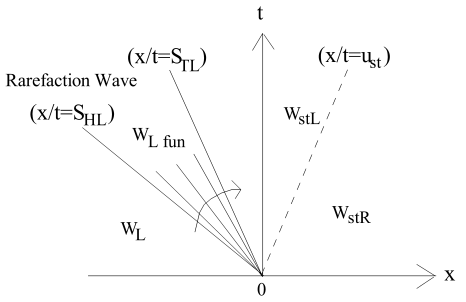

(b) Solution for a rarefaction left wave$H_{st} \leq H_L$.

Figure 3.5: Complete solution of the Riemann problem to the left of the contact wave.

head and tail are

$$\begin{aligned} S_{HR} &= u_R + a_R \\ S_{TR} &= u_{st} + a_{st} \end{aligned} \tag{3.42}$$

In this case the solution inside the righ rarefaction wave is given by

$$W_{Rfan} = \begin{cases} a = \frac{1}{3}\left(-u_R + 2a_R - \frac{x^1}{t}\right) \\ u = \frac{1}{3}\left(u_R - 2a_R - \frac{2x^1}{t}\right) \end{cases} \tag{3.43}$$

In Fig. 3.6 the structure of the complete solution is shown for the two possible waves on the right side of the shear wave $x/t = u_{st}$: in the first figure the right wave is a shock wave and in the second figure the right wave is a rarefaction wave.

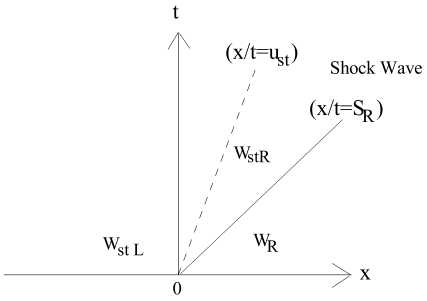

(a) Solution for a shock right wave $H_{st} > H_R$.

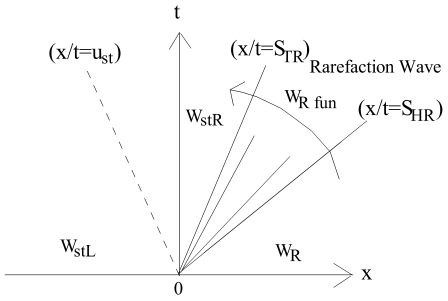

(b) Solution for a rarefaction right wave$H_{st} \leq H_R$.

Figure 3.6: Complete solution of the Riemann problem to the right of the contact wave.

The remaining components are easily obtained as a function of the celerity of

a contact wave, once H_{st} and u_{st} are calculated

$$\begin{cases} u_{st} > 0 \begin{cases} v = v_L \\ w = w_L \end{cases} \\ u_{st} < 0 \begin{cases} v = v_R \\ w = w_R \end{cases} \end{cases} \tag{3.44}$$

3.5 Fractional step method

The fractional step methods is used to produce a non-hydrostatic divergence-free velocity field and update the water depth. The predictor field $(Hu^l)^*$, obtained by solving the momentum balance equation without considering the dynamic pressure, is associated to a non-divergence free velocity field. This approximated velocity field should be corrected by the gradient of the scalar potential Ψ. The scalar potential is calculated by a Poisson-like equation expressed in terms of the conserved variable Hu^l. The known right-hand side of the Poisson-like equation is the divergence of the predictor field

$$\frac{\partial[\frac{g^{ls}\partial\Psi}{\partial s}H\sqrt{g_0}]}{\partial\xi^l} = -\frac{\partial(Hu^l)^*\sqrt{g_0}}{\partial\xi^l} \tag{3.45}$$

in which g^{ls} with $l, s = 1, 2, 3$ is contravariant metric tensor. The corrector field is obtained by the gradient of the scalar potential Ψ

$$(Hu^l)^c = H\frac{g^{ls}\partial\Psi}{\partial s} \tag{3.46}$$

The sum of the predictor field and the corrector field gives the final non-hydrostatic divergence-free velocity field

$$Hu^l = (Hu^l)^* + (Hu^l)^c \tag{3.47}$$

Knowing the final velocity field it is possible to update the free-surface elevation by solving the continuity equation and it is possible to determine the

contravariant velocity components of the moving curvilinear vertical coordinate.

$$v^1 = v^2 = 0 \quad v^3 = \frac{\xi^3}{H}\frac{\partial H}{\partial t} \tag{3.48}$$

The Message Passing Interface (MPI) is used to parallelised the calculation code to save computational time.

Chapter 4

Smagorinsky Turbulence Model under breaking waves

In the literature, the turbulence closure relations for the Reynolds stress tensor in breaking wave simulations are made by different turbulence models like the Smagorinsky model, one-equation or two-equation turbulence models.

In recent papers [9, 11, 12, 20, 23, 25, 31, 33, 44, 47, 52, 73], the Smagorinsky turbulence model is calibrated for three-dimensional numerical simulations of wave propagation from deep-water to the coastline.

It should be noted however that the existing numerical models that use the Smagorinsky turbulence model [47] are collocated in the context of low-order accurate shock-capturing numerical schemes. In these schemes, the reconstructions of point values of the conserved variables are made by 2^{nd} order TVD schemes and the Riemann problem is solved by an approximate Riemann solver. As just mentioned in Chapter 3, these models leave the task of dissipating the kinetic energy of the ensemble-averaged motion (in which the complete spectrum of the turbulent stochastic motion is not directly simulate) in the surf zone to the shock-capturing numerical scheme and use the Smagorinsky turbulence model with coefficients significantly underestimated in order to eliminate some spurious oscillations. In the cases in which the 2^{nd} order shock-capturing numerical schemes are used, the breaking wave height is underestimated and the wave breaking point is shifted offshoreward.

In order to reduce the dissipation of the kinetic energy of the ensemble-averaged motion introduced by the numerical schemes and leave the task of dissi-

pating the kinetic energy of the ensemble-averaged motion only to the turbulence model, it is necessary to use the new high-order numerical scheme, presented in Chapter 3 and adequate turbulence models. This new shock-capturing numerical scheme uses conserved variables, 5^{th}-order WTENO reconstructions and an exact Riemann solver.

In the first section (Section 4.1) of this chapter, the Smagorinsky turbulence model and some considerations about the oscillating wave boundary layer are presented. In the second section (Section 4.2), the comparison between the numerical results obtained by using the new high-order scheme, presented in Chapter 3, and the numerical results obtained by using the low-order scheme are also presented, in order to validate the new high-order numerical scheme. In the last section (Section 4.3), some conclusive considerations are made about the use of the Smagorinsky turbulence model.

4.1 Smagorinsky Turbulence Model and near-wall treatment

One of the most popular turbulence models largely used in the literature for the simulation of breaking waves [44, 47, 73] is the Smagorinsky turbulence model.

In this turbulence model, the deviatoric part of the turbulent stress tensor is modeled as follow

$$T_{ij}^{dev} = T_{ij} - \frac{1}{3}T_{kk}\delta_{ij} = -2\nu_T S_{ij} \tag{4.1}$$

where T_{ij}^{dev} $(i, j = 1, 2, 3)$ are the Cartesian components of the deviatoric part of the turbulent stress tensor T_{ij}; δ_{ij} is the Kronecker symbol; S_{ij} are the Cartesian components of the strain rate tensor. The eddy viscosity ν_T is given by

$$\nu_T = (C_S\Delta)^2|S_{ij}| \tag{4.2}$$

in which $\Delta = \sqrt[3]{\Delta x^1 \Delta x^2 \Delta x^3}$ represents the turbulence length scale related to the grid size, C_S is the Smagorinsky coefficient, usually ranged between $0.1 - 0.3$ and $|S_{ij}|$ is the norm of the strain rate tensor S_{ij}.

The above Smagorinsky turbulence model is used outside the oscillating wave

boundary layer, while inside the oscillating wave boundary layer a specific near-wall treatment is assumed for the turbulent quantities.

The eddy viscosity in the oscillating wave boundary layer is deduced by following the line indicated by Liu and Lin [45].

According to the oscillating wave boundary layer theory, the zone close to the bottom can be divided into three main regions characterized by different types of stresses. Let be y^+ the dimensionless wall distance defined as follow

$$y^+ = \frac{zu^*}{\nu} \tag{4.3}$$

where z is the vertical distance from the wall, u^* is the bottom friction velocity and $\nu = 10^{-6}m^2s^{-1}$ is the kinematic viscosity.

- Viscous sublayer ($y^+ \leq 5$): this region is the lower part of the boundary layer characterized by the dominance of the viscous stresses;
- Buffer layer ($5 < y^+ \leq 30$): in this region viscous stresses and turbulent stresses coexist;
- Turbulent core ($y^+ > 30$): here the turbulent stresses dominate and the viscous stresses can be neglected.

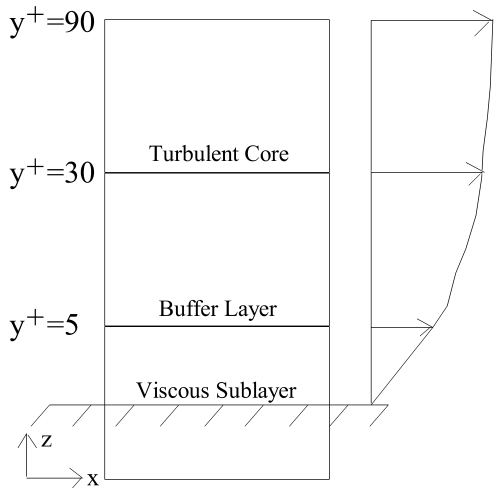

Figure 4.1: Oscillating wave boundary layer.

In this thesis, the equations of motion that include the Smagorinsky turbulence model are solved in the turbulent core, where the turbulent stresses are dominant, and the velocity boundary condition $\vec{u}_B$ is placed on the border between the buffer

layer and the turbulent core. The eddy viscosity near the bottom and the velocity boundary condition are deduced by the theory of the oscillating wave boundary layer [45] that is outlined below.

The Reynolds averaged momentum balance equation in the Cartesian coordinate system is given by

$$\frac{\partial \overline{u_i}}{\partial t} + \overline{u_j}\frac{\partial \overline{u_i}}{\partial x_j} = -\frac{1}{\overline{\rho}}\frac{\partial \overline{P}}{\partial x_i} + G_i + \frac{1}{\overline{\rho}}\frac{\partial \overline{\tau_{ij}}}{\partial x_j} - \frac{\partial \overline{u_i' u_j'}}{\partial x_j} - \overline{\frac{\partial P'}{\partial x_i}} + \overline{\frac{1}{\rho'}\frac{\partial \tau_{ij}'}{\partial x_j}} \tag{4.4}$$

in which $i, j = 1, 2, 3$[1]; the symbol $\overline{(\quad)}$ indicates a Reynolds averaged quantity, the symbol $(\quad)'$ indicates the turbulent fluctuations, P is the total pressure, G_i is the $i-th$ component of the gravity acceleration and τ_{ij} is the viscous stress tensor.

Let us consider an oscillating turbulent free-surface flow produced by the propagation of the wave train over the rigid bottom, in which z is the coordinate normal to the bottom and x is the coordinate in the wave propagation direction. By invoking the boundary layer approximation, close to the bottom, Eq. 4.4 reduces to

$$\nu\frac{\partial^2 \overline{u}}{\partial z^2} - \frac{\partial \overline{u'w'}}{\partial z} = 0 \tag{4.5}$$

in which $\overline{u}$ and $\overline{w}$ are the Reynolds averaged Cartesian velocity components in the direction of x and z axis respectively, and $\overline{u'}$ and $\overline{w'}$ are their turbulent fluctuations.

By integrating Eq. 4.5 along the vertical direction, from the wall ($z = 0m$) to z outside the viscous sublayer where the viscous stresses can be neglected, it is obtained the following expression

$$\begin{gathered} -\int_0^z \nu\frac{\partial^2 \overline{u}}{\partial z^2}dz = -\int_0^z \frac{\partial \overline{u'w'}}{\partial z}dz \\ \underbrace{-\nu\frac{\partial \overline{u}}{\partial z}\Big|_z}_{0} + \underbrace{\nu\frac{\partial \overline{u}}{\partial z}\Big|_0}_{visc.str.} = \underbrace{\overline{u'w'}\big|_z}_{turb.str.} + \underbrace{\overline{u'w'}\big|_0}_{0} \\ \nu\frac{\partial \overline{u}}{\partial z}\Big|_0 = \overline{u'w'}\big|_z \end{gathered} \tag{4.6}$$

[1]In this thesis the Einstein notation is used. The notation conventional implies summation over a set of indexed terms in a formula. When an index variable appears twice in a single term, it implies summation of that term over all the values of the index. $y = \sum_{i=1}^{3} c_i x^i = c_1 x^1 + c_2 x^2 + c_3 x^3$ is simplified by the convention to $y = c_i x^i$. The upper indices are not exponents but are indices of coordinates, coefficients or basis vectors.

The first term on the left-hand side of Eq. 4.6 is equal to zero because outside the viscous sublayer the viscous stresses can be neglected; the second term on the right-hand side of the equation is null because the turbulent stresses can be neglected inside the viscous sublayer.

The viscous stress at the bottom τ_w can be expressed in terms of the so-called friction velocity u^* as follow

$$\nu \frac{\partial \overline{u}}{\partial z}\bigg|_0 = \frac{\tau_w}{\rho} = u^{*2} \tag{4.7}$$

The turbulent stresses can be expressed as follow

$$\tau_{ij} = -\overline{u_i' u_j'} = \nu_T \frac{\partial \overline{u_i'}}{\partial x_j} \tag{4.8}$$

By assuming that the eddy viscosity is proportional to square of mixing length

$$\nu_T \propto l^2 \tag{4.9}$$

and by assuming that the mixing length can be proportional to the wall distance through a coefficient κ [56]

$$l \propto \kappa z \tag{4.10}$$

the eddy viscosity can be expressed by the mixing-length model

$$\nu_T = l^2 \left|\frac{\partial \overline{u}}{\partial z}\right| = (\kappa z)^2 \left|\frac{\partial \overline{u}}{\partial z}\right| \tag{4.11}$$

Introducing Eqs. 4.7 and 4.8 in Eq. 4.6 it can be obtained

$$u^{*2} = \nu_T \frac{\partial \overline{u'}}{\partial z} \tag{4.12}$$

By using Eq. 4.11, Eq. 4.12 becomes

$$u^{*2} = (\kappa z)^2 \left|\frac{\partial \overline{u}}{\partial z}\right| \frac{\partial \overline{u}}{\partial z} \tag{4.13}$$

from which it is possible to obtain

$$\frac{\partial \overline{u}}{\partial z} = \frac{u^*}{\kappa z} \tag{4.14}$$

The eddy viscosity in the oscillating boundary layer outside the viscous sublayer can be obtained by introducing Eq. 4.14 in Eq. 4.11

$$\nu_T = \kappa u^* z \tag{4.15}$$

in which $\kappa = 0.41$ is the von Kàrmàn constant.

The integration of Eq. 4.14 in the turbulent core (for hydraulically rough regime) produces the well-known logarithmic law

$$\frac{\overline{u(z)}}{u^*} = \frac{1}{\kappa} ln \left(\frac{z}{S_C/30} \right) \tag{4.16}$$

in which S_C is the bottom roughness and $\overline{u(z)}$ is the velocity in the turbulent core.

By assuming the above logarithmic law for the distribution of the velocity in the wall region, the friction velocity is calculated by introducing in Eq. 4.16 the value of the velocity in the first calculation point, that is placed inside the turbulent core, $\overline{u(z)}$, and its coordinate z. The resulting logarithmic law is used to calculate the velocity boundary condition, that is placed at the border between buffer layer and turbulent core.

4.2 Results and discussion

Three breaking wave test cases are numerically reproduced by using Smagorinsky turbulence model and the above-mentioned near-wall treatment. The numerical simulations are carried out by two different numerical schemes: the low-order numerical scheme (2^{nd} order TVD reconstructions, Approximated Riemann solver and primitive variables used for the equations of motion) and the high-order numerical scheme (5^{th} order WTENO reconstructions, Exact Riemann solver and conserved variables for the equations of motion).

In Fig 4.2 the discretization of the vertical cells are shown. The first computational grid cell in which the equations of motion are solved is indicated by number 1 in Fig. 4.2 and it is placed in the turbulent core. At the distance z_B from the bottom, the parallel to the bottom velocity boundary condition u_B is determined by using Eq. 4.16 (in which u^* is previously calculated by introducing the veloc-

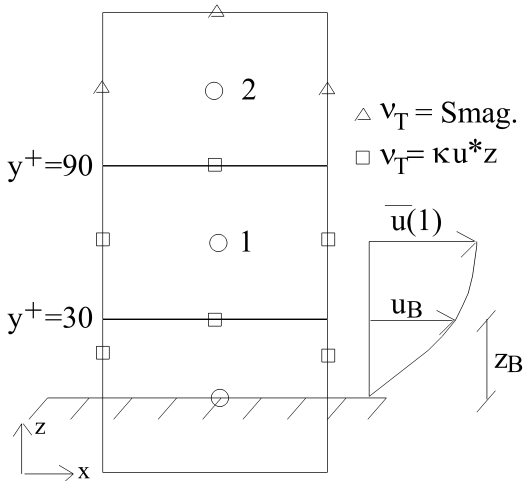

Figure 4.2: Discretization of the vertical cells outside the buffer layer for the Smagorinsky model.

ity $\overline{u}(1)$ and its coordinate z_1 in the logarithmic law). The lower face of the first computational grid cell is at $y^+ = 30$, at the border between the buffer layer and the turbulent core. The eddy viscosity inside the oscillating wave boundary layer ($y^+ \leq 90$) is calculated by Eq. 4.15; outside the oscillating wave boundary layer ($y^+ > 90$) the eddy viscosity is calculated by the Smagorinsky model (Eq. 4.2).

The test cases reproduced in this thesis are three: Ting and Kirby test case for spilling breaker [63], Stive test case for spilling breaker [60, 61] and Stive test case for a spilling/plunging breaker [61]. A synthetic description of these tests is given in Tab. 4.1.

Test	Name	Turb. model	Numerical Scheme	Note
Ting and Kirby [63]	Ting1	Smagorinsky	2nd-order (TVD + Approx. Riemann S.)	$C_S = 0.2$
Ting and Kirby [63]	Ting2	Smagorinsky	5nd-order (WTENO + Exact Riemann S.)	$C_S = 0.2$
Ting and Kirby [63]	Ting3	Smagorinsky	5nd-order (WTENO + Exact Riemann S.)	$C_S = 0.1$ $C_S = 0.2$ $C_S = 0.3$
Stive spilling [60, 61]	Stive1	Smagorinsky	5nd-order (WTENO + Exact Riemann S.)	$C_S = 0.1$ $C_S = 0.2$ $C_S = 0.3$
Stive spilling-plunging [61]	Stivesp1	Smagorinsky	5nd-order (WTENO + Exact Riemann S.)	$C_S = 0.1$ $C_S = 0.2$ $C_S = 0.3$

Table 4.1: Test cases with Smagorinsky turbulence models.

Iribarren number [34] is used to describe and classify periodic waves breaking

on sloping beaches. This dimensionless parameter is determined [2, 34] as follow

$$\xi_b = \frac{tan(\alpha)}{\sqrt{\frac{H_b}{L_0}}} = \begin{cases} \xi_b < 0.4 & spilling \quad breaker \\ 0.4 < \xi_b < 2.0 & plunging \quad breaker \\ \xi_b > 2.0 & surging \quad or \quad collapsing \end{cases} \tag{4.17}$$

where α is the beach slope, H_b is the wave height at the breaking point and $L_0 = gT^2/(2\pi)$ is the wavelenght in deep water (T is the wave period). The four types of breaking waves are described below and are represented in Fig. 4.3.

- Spilling breakers: these breaking waves move along gradually sloping beach. The crest spills gradually down the wave face. The time spent to break is long.

- Plunging breakers: these breaking waves move toward a steep beach or a bottom with sudden depth changes. The base of the wave slows down while the crest forms upward and continues to spin. The wave fronts become concave as the trough and the crest curls over and breaks on the trough. There is a lot of air compressed in this breaker. This kind of breaking waves are common in offshore wind conditions.

- Surging breakers: these breaking waves are characterized by long-period and rush up a very steep beach without dissipating much kinetic energy. The base of the wave moves fast and does not allow the crest to evolve. This breaker does not break.

- Collapsing breakers: these breaking waves is a mix of the surging and plunging waves. The crest does not break and the bottom face of the wave gets vertical and collapses.

In Tab. 4.2 a schematic summary of the wave parameters for each test cases are reported.

4.2.1 Ting and Kirby test case of a spilling breaker with a cnoidal wave

The first test case is Ting and Kirby [63] laboratory test. The authors [63] experimentally reproduce spilling breaking waves by using cnoidal waves that have

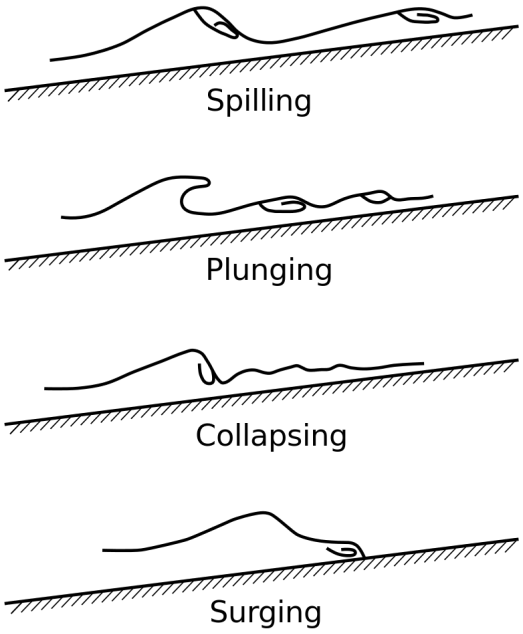

Figure 4.3: Breaker types [69].

Test case	Waves type	T $[s]$	H_s $[m]$	L $[m]$	h $[m]$	Slope $[-]$	x_B $[m]$	H_B $[m]$
Ting [63]	Spilling	2.00	0.125	6.35	0.4	1:35	6.25	0.156
Stive [60, 61]	Spilling	1.79	0.159	4.96	0.85	1:40	35.5	0.178
Stive [61]	Spilling/Plunging	2.99	0.142	7.30	0.85	1:40	33.5	0.226

Table 4.2: Wave parameters: wave period, wave height in deep water, wavelenght, undisturbed water depth in deep water, beach slope, wave breaking point, wave height at the breaking point.

wave height $H_s = 0.125m$, wavelength $L = 6.35m$ and wave period $T = 2s$. The wave tank has an undisturbed water depth of $h = 0.40m$ and a seabed slope of $1 : 35$. The used computational grid has 512 nodes in the wave propagation direction, with grid spacing of $\Delta x = 0.05m$, and 13 non uniform layer in the vertical direction.

On the west side of the computational domain, a cnoidal wave [68] is generated by imposing the velocity components and the free-surface elevation. On the east side of the computational domain a wet and dry technique is adopted. At the bottom of the computational domain the no-slip condition is imposed. In Fig. 4.4 the computational domain is represented. In the zone near the coastline (about $x > 11.0m$), the computational grid cells are much smaller than the ones before, for this reason the adopted time step is $\Delta t = 0.0001s$.

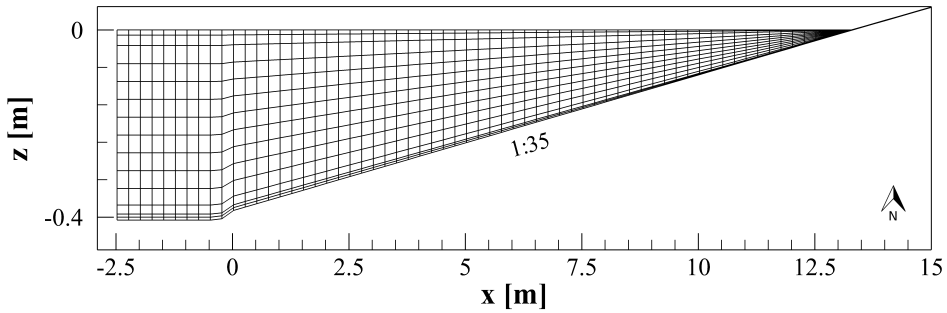

Figure 4.4: Computational domain for Ting and Kirby [63] test case (in the x-direction, only one line out every 10 is drawn).

In Fig. 4.5 the maximum, average and minimum water surface elevation obtained by the low-order numerical scheme are shown. The Smagorinsky coefficient used in this numerical simulation is $C_S = 0.2$. From the figure it is possible to notice that the local maximum water surface elevation is underestimated and the wave breaking point is shifted forward with respect to the experimental measurements. The main reason of the difference between the numerical and the experimental measurements in terms of the location of the wave breaking point is due to the use of the primitive variables (H and u^l) in the Poisson equation. From the Fig. 4.5 it can be notice that the use of the primitive variables produces an anticipated wave breaking point, due to incorrect velocity propagation of the shock waves [67], as already underlined in Chapter 3. Furthermore, the underestimation of the local maximum water surface elevations is due to the use of the low-order shock-capturing numerical scheme. In the adopted numerical scheme, the task of dissipating the kinetic energy of the ensemble-averaged motion is entrusted to the reconstruction technique and the approximate Riemann solver. By this way the numerical model underestimates the wave height around the wave breaking point, shifts offshoreward the wave breaking point and produces an excess of dissipation of kinetic energy of the ensemble-averaged motion.

In order to overcome all the drawbacks introduced by the use of the low-order numerical scheme the new high-order numerical scheme is used. In general, high-order numerical schemes introduce less numerical dissipation and allow to leave the turbulence model the task of dissipating the right quantity of kinetic energy of the ensemble-averaged motion.

In Fig. 4.6 the numerical results obtained with the new numerical scheme,

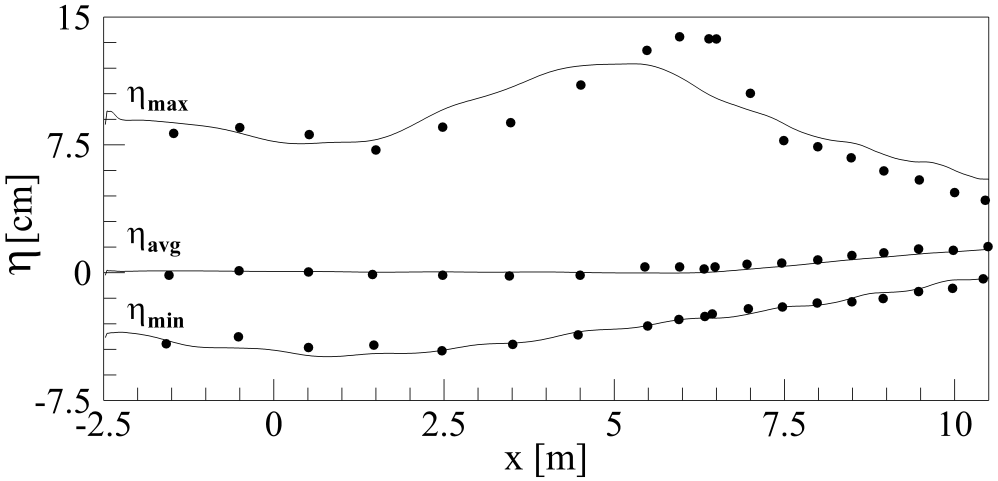

Figure 4.5: Ting1: local minimum, average and maximum water surface elevations. Experimental measurements • [63] and numerical results − with the Smagorinsky turbulence model and low-order numerical scheme.

presented in Chapter 3, are shown. The new shock-capturing scheme adopts conserved variables, 5^{th}-order WTENO reconstructions and an exact Riemann solver. The Smagorinsky coefficient used in this numerical simulation is $C_S = 0.2$.

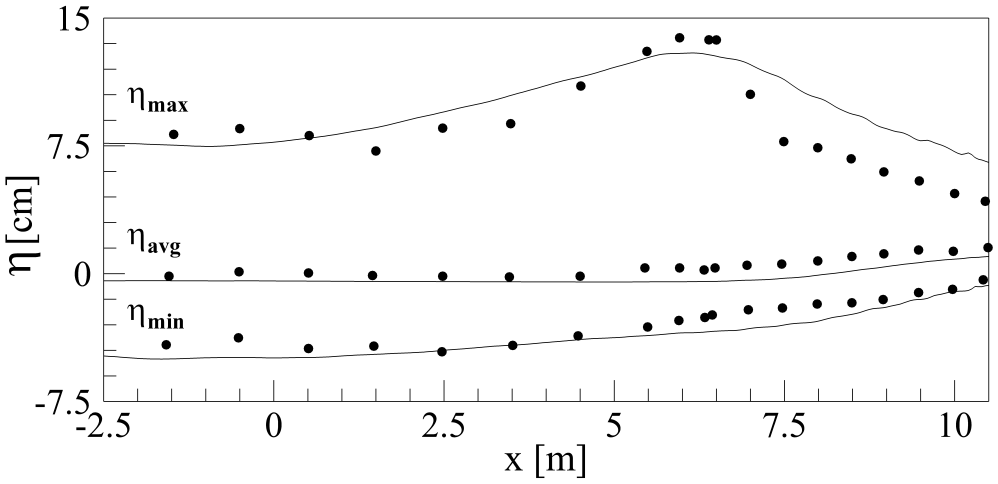

Figure 4.6: Ting2: local minimum, average and maximum water surface elevations. Experimental measurements • [63] and numerical results − with the Smagorinsky turbulence model and high-order numerical scheme.

The location of the wave breaking point is slightly shifted offshoreward with respect to the one obtained by the experimental measurements. The local maximum water surface elevation is slightly underestimated around the wave breaking point and is overestimated in the surf zone. By comparing the results obtained by the two numerical models (Figs. 4.5 and 4.6), it is evident that the high-order numerical model limits the excessive numerical dissipation of the ensemble-averaged

motion introduced by the low-order numerical scheme.

In order to understand how the Smagorinsky coefficient can influence the numerical results, three different numerical simulations has been made with three different values of the Smagorinsky coefficient. In Fig. 4.7 the three numerical results are shown in comparison with the experimental measurements. The numerical simulations are carried out with the new shock-capturing numerical scheme.

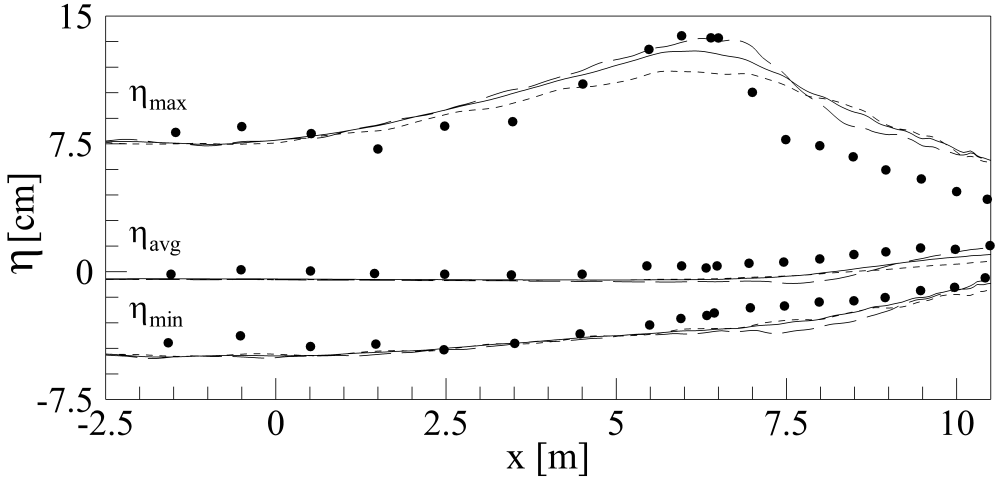

Figure 4.7: Ting3: local minimum, average and maximum water surface elevations. Experimental measurements • [63]. Numerical results with $C_S = 0.1$ dashed line $- - -$, $C_S = 0.2$ solid line $-$ and $C_S = 0.3$ dotted line $\cdots$ (Smagorinsky turbulence model and high-order numerical scheme).

The dashed line represents the numerical results obtained by using $C_S = 0.1$, the solid line represents the same numerical results shown in Fig. 4.6 obtained with $C_S = 0.2$ and dotted line represents the ones obtained by $C_S = 0.3$. It is possible to notice that high values of the Smagorinsky coefficient reduce the local maximum water surface elevations in the shoaling zone and around the wave breaking point. As a consequence, the wave breaking point is shifted offshoreward. The local maximum water surface elevation in the surf zone is overestimated in all the three simulations.

4.2.2 Stive test case of a spilling breaker with a monochromatic wave

The second test case that is numerically reproduced is a laboratory test by Stive [60, 61]. The author experimentally reproduced a spilling breaking waves that

have wave height $H_s = 0.159m$, wavelenght $L = 4.96m$ and wave period $T = 1.79s$. The wave tank has an undisturbed water depth of $h = 0.85m$ at the beginning, length of $55m$ and a seabed slope $1 : 40$. The used computational grid has 960 nodes in the wave propagation direction, with grid spacing of $\Delta x = 0.05m$ and 13 non uniform layer in vertical direction. A monochromatic and regular wave is generated on the west side and a wet and dry technique is adopted on the east side of the computational domain. At the bottom, no-slip condition is imposed. The computational domain is represented in Fig. 4.8. In the zone near the coastline (about $x > 36.0m$), the computational grid cells are much smaller than the ones before, for this reason the adopted time step is $\Delta t = 0.0001s$.

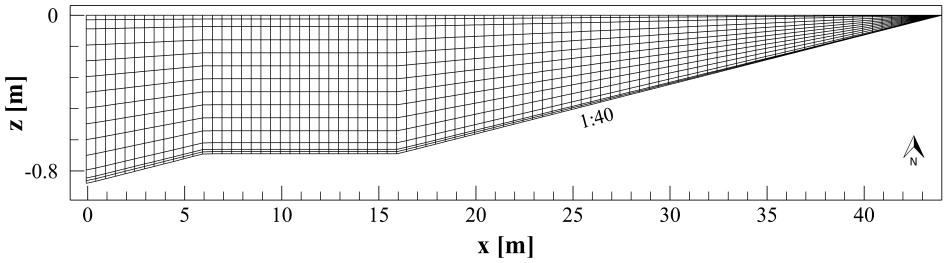

Figure 4.8: Computational domain for Stive [60, 61] test case (in the x-direction, only one line out every 10 is drawn).

In Fig. 4.9, the numerical results (in terms of wave height) obtained by the new high-order numerical scheme (presented in Chapter 3), for three different values of the Smagorinsky coefficient, are shown in comparison with the experimental measurements. In Fig. 4.9, the solid line is obtained by using $C_s = 0.2$, the

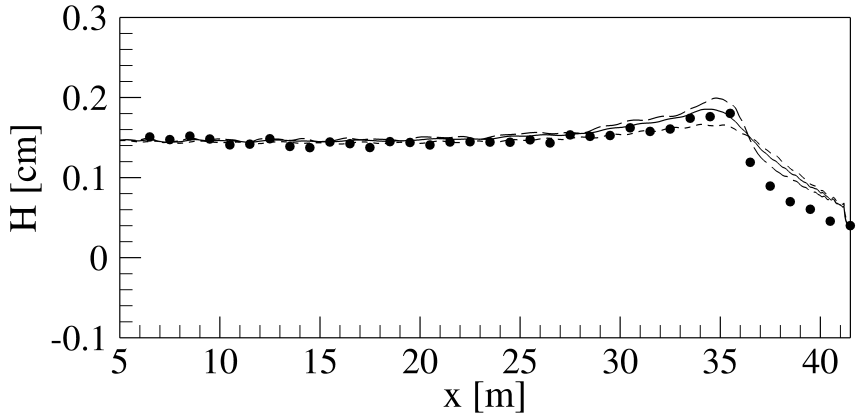

Figure 4.9: Stive1: wave height. Experimental measurements • [60, 61]. Numerical results with $C_S = 0.1$ dashed line $- - -$, $C_S = 0.2$ solid line $-$ and $C_S = 0.3$ dotted line $\cdots$ (Smagorinsky turbulence model and high-order numerical scheme).

dotted line is obtained by using $C_s = 0.3$ and the dashed line is obtained by using $C_s = 0.1$. In all the three results, the wave breaking point is shifted offshoreward. The highest value of the Smagorinsky coefficient produces an underestimation of the wave height around the wave breaking point; while the lowest value one produces an overestimation of the breaking-point wave height. In the surf zone, all the three numerical simulations produce the overestimation of the wave heights.

4.2.3 Stive test case of a spilling-plunging breaker with a monochromatic wave

The third test case that is numerically reproduced is another laboratory test by Stive [61]. In this case the author experimentally reproduced spilling/plunging breaking waves, i.e. waves characterized by almost plunging wave breaking. In this case, the Iribarren number is $\xi_b = 0.4$, which is the upper limit of the spilling breaking wave (beyond which the waves are considered as plunging breaking waves).

The wave tank used by Stive [61] for this particular breaking wave is the same used for test Stive1 in Subsection 4.2.2: the tank is $55m$ long, the undisturbed water depth in deep water is $h = 0.85m$ and the slope is $1 : 40$. For this test, the wave height is $H_s = 0.142m$, the wavelenght is $L = 7.3m$ and the wave period is $T = 2.99s$. The computational grid adopted for the numerical simulation of this test is the same of the one used to simulate Stive1 test: 960 nodes in the wave propagation direction ($\Delta x = 0.05m$) and 13 non uniform layer in vertical direction. On the west side of the computational domain, monochromatic and regular waves are generated, while a wet and dry technique is adopted on the opposite side. At the bottom, no-slip conditions are imposed. The computational domain is represented in Fig. 4.8.

In Fig. 4.10, the numerical results (in terms of wave height) obtained with three different values of the Smagorinsky coefficient are compared with the experimental measurements. The numerical model used for the simulations are the one presented in Chapter 3 (high-order WTENO reconstructions and exact Riemann solver). The numerical simulation obtained with a Smagorinsky coefficient $C_s = 0.1$ overestimates the wave breaking height. Furthermore, the location of the wave breaking point is shifted forward with respect to the measured one (as

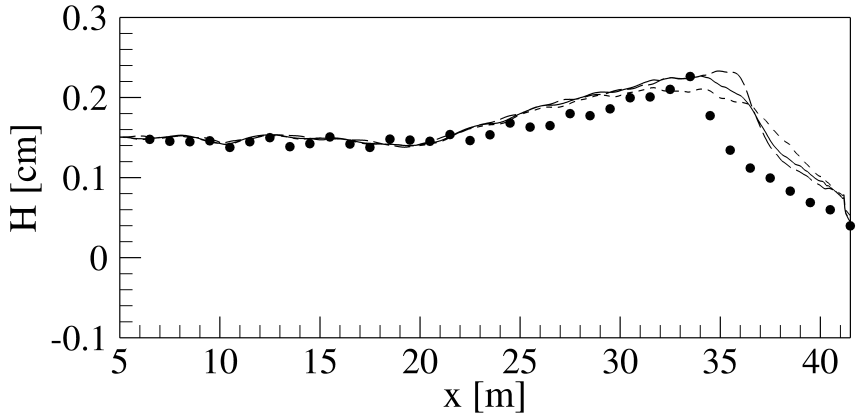

Figure 4.10: Stivesp1: wave height. Experimental measurements • [61]. Numerical results with $C_S = 0.1$ dashed line $- - -$, $C_S = 0.2$ solid line $-$ and $C_S = 0.3$ dotted line $\cdots$ (Smagorinsky turbulence model and high-order numerical scheme).

it is possible to see from dashed line in Fig. 4.10). By using $C_s = 0.2$ (solid line in Fig. 4.10), the wave breaking height is well predicted, but the wave breaking point is shifted forward. The numerical results obtained with $C_s = 0.3$ (dotted line in Fig. 4.10) show both an underestimation of the wave breaking height and a wave breaking point that is shifted forwards. In the surf zone, all the numerical results overestimate the wave height. From the Fig. 4.10, it is possible to notice that high values of the Smagorinsky coefficient underestimate the wave height around the wave breaking point, without significantly improving the wave height prediction in the surf zone.

4.3 Conclusions

In this chapter, it has been demonstrated that the low-order shock-capturing numerical scheme underestimates the wave height around the wave breaking point, gives an erroneous wave breaking point (shifted offshoreward) and produces an excess of dissipation of kinetic energy of the ensemble-averaged motion. In the simulations carried out by the above-mentioned numerical scheme, the Smagorinsky turbulence model is used just to eliminate the spurious oscillations.

It has been demonstrated that the new high-order shock-capturing numerical scheme limits the numerical dissipation, leaving the task of dissipating the kinetic energy of the ensemble-averaged motion to the turbulence model. The numerical results obtained by this numerical model (with the Smagorinsky turbu-

lence model) are in better agreement with the experimental measurements than the ones obtained by the low-order numerical model. For the same value of the Smagorinsky coefficient, the high-order scheme gives a more onshore located wave breaking point and a higher breaking wave height than the ones obtained by the low-order scheme.

In the high-order shock-capturing numerical schemes for breaking waves, the Smagorinsky turbulence model is not adequate to correctly represent the wave height evolution in the surf zone. Indeed, the numerical results show that the wave breaking point is shifted onshoreward and the local maximum water surface elevations are overestimated in all the surf zone. In addition, the Smagorinsky model is significantly influenced by the choice of the coefficient C_s, as demonstrated by the results.

From a general point of view, high values of the Smagorinsky coefficient (with high-order numerical schemes) can produce an overestimation of the eddy viscosity in the shoaling zone, in the region around the wave breaking point and in the surf zone. The same overestimation can be produced by the choice of the spatial discretization step: high values of the spatial discretization step increment the eddy viscosity and thus overestimate the dissipation of the kinetic energy of the ensemble-averaged motion in the region around the wave breaking point and in the surf zone. The strong influence of the Smagorinsky coefficient and the grid dimension on the eddy viscosity can produce numerical results very different from each other.

Furthermore, the Smagorinsky model does not give any information about the turbulent kinetic energy distribution in the domain, for this reason it is no possible to validate the model in terms of turbulent kinetic energy.

Chapter 5

$k - l$ Turbulence Model under breaking waves

Some considerations should be replied about the use of the Smagorinsky turbulence models with high-order shock-capturing numerical schemes. The solution of the equations of motion with high-order shock-capturing numerical scheme and with the Smagorinsky turbulence model is not able to correctly represent the wave height, the wave breaking point, as well as the effects of the turbulent phenomena on the dissipation of kinetic energy of the ensemble-averaged motion in the surf zone. The ability of the Smagorinsky turbulence model to dissipate the kinetic energy of the ensemble-averaged motion is directly influenced by the value of the Smagorinsky coefficient and the adopted spatial discretization step. After choosing the spatial discretization step, a laborious calibration of the Smagorinsky coefficient could improve the results regarding the wave breaking point, but could not guarantee an adequate reduction of the wave height in the surf zone. Furthermore by using Smagorinsky model, it is not possible to have any information about the turbulent kinetic energy distribution in the domain, which can be useful to validate the model in terms of turbulent kinetic energy.

To overcome the Smagorinsky turbulence model drawbacks, many authors [6, 18, 19] used a one-equation turbulence model called $k - l$ (k is the turbulent kinetic energy and l is the mixing length) in which a partial differential equation for the turbulent kinetic energy k is solved and a closure relation for the turbulent stress tensor is used as a function of the turbulent kinetic energy and the mixing

length.

Some synthetic considerations should be done about the turbulent structures in the surf zone. The turbulent structures in the surf zone are very complex. Outside the surf zone, the production of turbulent kinetic energy is limited to the oscillating wave boundary layer; inside the surf zone, the production of turbulent kinetic energy is mainly located in the oscillating wave boundary layer and near the breaking wave fronts. A part of the turbulent kinetic energy produced at the wave breaking point and in the oscillating wave boundary layer is dissipated in the intermediate zone, between the oscillating wave boundary layer and the wave fronts. In the existing $k-l$ turbulence model [6, 18, 19], the dissipation of turbulent kinetic energy is represented in the same way both before and after the wave breaking point. In particular, this model does not take into account the differences of dissipation due to the turbulent phenomena in the shoaling zone, in the region around the wave breaking point and in the surf zone. In the papers present in the literature [6, 18, 19, 47] concerning breaking wave simulations that adopt the Smagorinsky or the $k-l$ turbulence model, the equations of motion are not solved in the zone nearest to the bottom.

As is known, the oscillating wave boundary layer can be divided into three regions: the viscous sublayer, the buffer layer and the turbulent core. In order to simulate the turbulent phenomena and their effects on turbulent kinetic energy in the oscillating wave boundary layer (in the turbulent core and in the buffer layer) and in the proximity of the free surface in the breaking zone, it is necessary implement an adequate $k-l$ turbulence model.

The new $k-l$ turbulence model proposed in this thesis is presented in this Chapter. This new model is proposed to simulate the turbulent phenomena that occur in the surf zone and in the oscillating wave boundary. The k-equation is written in integral contravariant form on generalized curvilinear coordinate system.

Two different $k-l$ turbulence models are presented in this thesis: the standard $k-l$ model, hereinafter called KLS, and new $k-l$ model, hereinafter called KLN.

In the first model, KLS, the mixing length is easily calculated as proportional to the undisturbed water depth (as suggested by [6, 63]). The first point nearest

to the bottom, where the equations of motion are solved, is placed in the turbulent core of the oscillating wave boundary layer, while the equation of the turbulent kinetic energy is solved outside the oscillating wave boundary layer. The eddy viscosity in the oscillating wave boundary layer is calculated by the hypothesis between production and dissipation of turbulent kinetic energy in all the turbulent core and it is a function of the friction velocity.

In order to correctly take into account the effects that the turbulent phenomena (associated with wave propagation) have on the dissipation of the kinetic energy of the ensemble-averaged motion, it is necessary to distinguish the behaviour of the turbulence model before and after the wave breaking point. For this reason, in the second model, KLN, outside the oscillating wave boundary layer, a new formula for the mixing length is proposed as a function of the first and second spatial derivatives of the local maximum water surface elevation. In the oscillating wave boundary layer, the mixing length is calculated by the hypothesis of the balance between production and dissipation of turbulent kinetic energy.

The first point, nearest to the bottom, in which the equations of motion are solved, is placed in the buffer layer. The velocity boundary condition is placed in the buffer layer at the border with the viscous sublayer. The fist point, nearest to the bottom, in which the k-equations is solved, is in the buffer layer in the proximity to the viscous sublayer.

In the first section, Section 5.1, the equations for the $k-l$ turbulence model are presented in integral contravariant form on a time-dependent curvilinear coordinate system. In Section 5.2 and Section 5.3 the standard $k-l$ model (KLS) and the new $k-l$ model (KLN) are presented. In Section 5.4, some laboratory tests are numerically reproduced and compared by using both turbulence models. In the last section, Section 5.5, some conclusive considerations are made about the use of the new $k-l$ turbulence model.

5.1 Equations of $k-l$ Turbulence Model

The equation for the turbulent kinetic energy in the present thesis is written in integral contravariant form in a time-dependent curvilinear coordinate system as

follow

$$\begin{aligned}\frac{\partial\overline{Hk}}{\partial\tau} = &-\frac{1}{\Delta V_0\sqrt{g_0}}\sum_{\alpha=1}^{3}\left\{\int_{\Delta A_0^{\alpha+}}\left[Hk\left(\frac{Hu^\alpha}{H}-\frac{Hw_g^\alpha}{H}\right)\right]\sqrt{g_0}d\xi^\beta d\xi^\gamma - \right.\\ &\left.\int_{\Delta A_0^{\alpha-}}\left[Hk\left(\frac{Hu^\alpha}{H}-\frac{Hw_g^\alpha}{H}\right)\right]\sqrt{g_0}d\xi^\beta d\xi^\gamma\right\}\\ &+\frac{1}{\Delta V_0\sqrt{g_0}}\sum_{\alpha=1}^{3}\left\{\int_{\Delta A_0^{\alpha+}}\left[\left(\nu+\frac{\nu_T}{\sigma_k}\right)g^{\alpha r}\frac{\partial k}{\partial\xi^r}H\sqrt{g_0}\right]d\xi^\beta d\xi^\gamma - \right.\\ &\left.\int_{\Delta A_0^{\alpha-}}\left[\left(\nu+\frac{\nu_T}{\sigma_k}\right)g^{\alpha r}\frac{\partial k}{\partial\xi^r}H\sqrt{g_0}\right]d\xi^\beta d\xi^\gamma\right\}\\ &+\frac{1}{\Delta V_0\sqrt{g_0}}\int_{\Delta V_0}\left[(P_k-\varepsilon)H\sqrt{g_0}\right]d\xi^1 d\xi^2 d\xi^3\end{aligned} \tag{5.1}$$

where P_k and ε are respectively the production and dissipation of turbulent kinetic energy and σ_k is a coefficient and in this thesis is assumed equal to 1. In Eq. 5.1, it is possible to identify the different terms that make up the turbulent kinetic energy transport equation [71].

- Unsteady term: this term is the first term on left-hand side of Eq. 5.1.
- Advection: in Eq. 5.1, the advection term is identified by the first two terms on the right-hand side of the k-equation. Advection is the transport of a quantity by bulk motion of a fluid. The sum of the unsteady term and the advection gives the rate of change of the turbulent kinetic energy following a fluid particles.
- Molecular and turbulent diffusion: these quantities are summed in the third and fourth terms of Eq. 5.1. The molecular diffusion takes place for the random impacts of the molecules due to the thermal agitation. The molecular diffusion represents the diffusion of turbulence energy caused by fluid's natural molecular transport process. The turbulent diffusion (represented by the triple correlation of the velocity) is analogous to the molecular diffusion, but it does not have a true physical meaning, being dependent on the flow conditions and it is not a property of the fluid. The turbulent diffusion enhances the transfer of mass, momentum and energy
- Production and dissipation: is indicated by the last term on the right-hand

side of Eq. 5.1. The production represents the rate at which kinetic energy is transferred from the mean flow to the turbulence. The dissipation is the rate at which turbulence kinetic energy is converted into thermal internal energy. This term is equal to the mean rate at which work is done by the fluctuating part of the strain rate against the fluctuating viscous stresses.

The production of turbulent kinetic energy is given by

$$P_k = \frac{T^{lm}}{H}(Hu_l)_{,m} \tag{5.2}$$

where $(u_l)_{,m}$ is the covariant derivative of the covariant component of the velocity [1]. The dissipation of turbulent kinetic energy is given by

$$\varepsilon = C_\mu \frac{k^{\frac{3}{2}}}{l} \tag{5.3}$$

where $C_\mu = 0.09$. The closure relation for the turbulent stress tensor is given by

$$T^{lm} = -2\nu_T S^{lm} + \frac{2}{3}kg^{lm} \tag{5.4}$$

in which the eddy viscosity is a function of k and l

$$\nu_T = C_\mu \sqrt{k} l \tag{5.5}$$

The mixing length is usually assumed proportional to the undisturbed water depth, h, [6, 56]

$$l = \phi h \tag{5.6}$$

In the numerical simulations of breaking waves, the coefficient ϕ is usually assumed equal to 0.1 [6], according to the experimental measurements by Ting and Kirby [64, 65] that estimated a range of ϕ between 0.1 and 0.2 for breaking waves.

In the wave propagation from deep water to the coastline, five different zones can be identified in order to simplify the representation of the different characteristics of turbulence. The five zones are synthetically defined in the graph of the distribution of the local maximum water surface elevations, shown in Fig. 5.1. From this graph, Zone 1 is located before the wave breaking point, where the shoaling phenomenon takes place; in this zone, the production of turbulent

kinetic energy is mostly located near the bottom. Zone 2 is located around the wave breaking point where there is the maximum wave height. In this zone, the waves get steeper until they reach a limit value beyond which they break. When the wave breaking starts, there is a strong production of turbulence both at the bottom and at the wave breaking fronts. In the surf zone there are two different zones, as shown in Fig. 5.1. The first one, defined as Zone 3, is characterized by a strong reduction of wave height and, consequently, a large gradient of the local maximum water surface elevations. In the graph of the local maximum water surface elevations, this zone is characterized by the maximum negative slope. In the second part of the surf zone, named Zone 4, the wave continues to break with lower negative slope of the water surface elevation, compared to the one in Zone 3. In this zone, there is also a production of turbulent kinetic energy at the bottom and at the free surface, until the wave is completely dissipated in the wet and dry zone. Zone 5 is in proximity of the bottom, where most production of turbulent kinetic energy takes place inside the oscillating wave boundary layer.

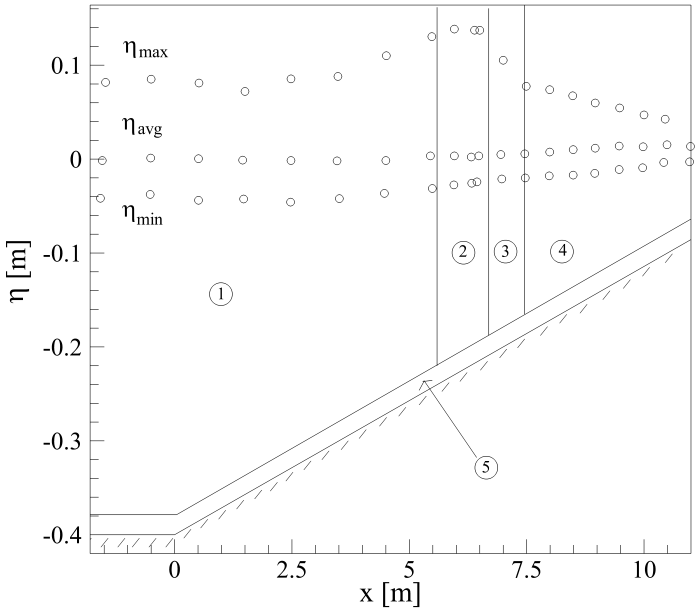

Figure 5.1: Definition of the zones. Zone 1: shoaling zone; Zone 2: zone around the wave breaking point; Zone 3: surf zone with high slope of the local maximum water surface elevations; Zone 4: surf zone. Zone 5: oscillating wave boundary layer. Experimental measurements ∘ of the local maximum water surface elevations.

In order to correctly take into account the effects that the turbulent phenomena (associated with wave propagation) have on the dissipation of the kinetic energy of the ensemble-averaged motion, it is necessary to distinguish the be-

haviour of the turbulence model in the different above-mentioned zones.

In this thesis, a new $k-l$ model is proposed to increase (in accordance with the experimental results) the slope (in absolute value) of the maximum water surface elevations in Zone 3. In this model, a new formulation for the mixing length is proposed; it is proportional to the undisturbed water depth through a coefficient that is a function of the spatial variation of the local maximum water surface elevation $\partial\eta_{max}(\xi^1)/\partial\xi^1$ (first derivative) and $\partial^2\eta_{max}(\xi^1)/(\partial\xi^1)^2$ (second derivative). The new equation for the mixing length proposed in this thesis reads

$$l = l_2 \cdot h = \frac{\lambda_{max}(\xi^1)}{4H_B} \left\{ k_1 + k_2 \left[\frac{\frac{\partial\eta_{max}(\xi^1)}{\partial\xi^1} - \left|\frac{\partial\eta_{max}(\xi^1)}{\partial\xi^1}\right|}{\left|\frac{\partial\eta_{max}(\xi^1)}{\partial\xi^1}\right|} \right] \right. \\ \left. \frac{\eta_{max}(\xi^1)}{max\ \eta_{max}(\xi^1)} \left| \frac{\frac{\partial^2\eta_{max}(\xi^1)}{(\partial\xi^1)^2} - \left|\frac{\partial^2\eta_{max}(\xi^1)}{(\partial\xi^1)^2}\right|}{\left|\frac{\partial^2\eta_{max}(\xi^1)}{(\partial\xi^1)^2}\right|} \right| \right\} \cdot h \quad (5.7)$$

where $l_2 = A_1\{k_1 + k_2[A_2\ A_3\ A_4]\}$ is the multiplier of the undisturbed water depth, $\eta_{max}(\xi^1) = \max_t\ \eta(\xi^1, t)$ and $\eta_{min}(\xi^1) = \min_t\ \eta(\xi^1, t)$ are, respectively, the local maximum and minimum (over time) water surface elevations; $\lambda_{max}(\xi^1) = \eta_{max}(\xi^1) + \eta_{min}(\xi^1)$ is the local wave height; $H_B = (\eta_{max} + h)_B$ is the total water depth at the wave breaking point ($k_1 = 1$ and $k_2 = 0.3$). The coefficient l_2 varies along the wave propagation direction and does not vary over the water depth.

The spatial variations of the local maximum water surface elevation allow to find the first four zones previously described: Zone 1 and Zone 2 (before the wave breaking point) are characterized by positive values of the derivative $\partial\eta_{max}(\xi^1)/\partial\xi^1$, Zone 3 and Zone 4 are characterized by negative values of the same derivative.

$$\begin{cases} \frac{\partial\eta_{max}}{\partial\xi^1} > 0 : Zone\ 1\ and\ Zone\ 2 \\ \frac{\partial\eta_{max}}{\partial\xi^1} < 0 : Zone\ 3\ and\ Zone\ 4 \end{cases} \quad (5.8)$$

By using these derivatives, it is possible to differentiate the behavior of the mixing length before and after the wave breaking point. The mixing length undergoes a reduction in Zone 3 by modifying the production of turbulent kinetic energy.

The two different $k-l$ turbulence models are presented below.

5.2 Standard $k-l$ Turbulence Model (KLS)

In this thesis, in the numerical simulations of breaking waves carried out by the Standard $k-l$ turbulence model (KLS), the same spatial discretization and near-wall treatment used in the numerical simulations carried out by the Smagorinsky turbulence model (described in Section 4.1) are adopted. According to [6, 20, 45, 47], the calculation point nearest to the bottom, in which the equations of motion are solved, is located inside the turbulent core. The velocity boundary condition is calculated by the logarithmic law, Eq. 4.16 and it is placed at the border between the buffer layer and the turbulent core. The eddy viscosity in the oscillating wave boundary layer, outside the viscous sublayer, is calculated by Eq. 4.15 and it is a function of the friction velocity, that it is determined by introducing in Eq. 4.16 the value of the velocity in the first calculation point.

Outside the oscillating wave boundary layer, the turbulent kinetic energy equation is solved, the eddy viscosity is calculated by the KLS turbulence model and the closure relation for the mixing length is the one proposed by [6, 63], $l = 0.1h$.

The turbulent kinetic energy boundary condition is imposed outside the oscillating wave boundary layer, where, according to [45], k is calculated by assuming the simplifying hypothesis of balance between production and dissipation of turbulent kinetic energy. The production of turbulent kinetic energy in the Cartesian coordinate system reads

$$P_k = -\overline{u_i' u_j'} \frac{\partial \overline{u_i}}{\partial x_j} = \varepsilon \tag{5.9}$$

in which $i, j = 1, 2, 3$.

By using Eqs. 4.12 and 4.13, Eq. 5.9 becomes

$$P_k = u^{*2} \frac{u^*}{\kappa z} = \varepsilon \tag{5.10}$$

Introducing Eq. 5.10 in Eq. 5.3, we obtain

$$\varepsilon = C_\mu \frac{k^{3/2}}{l} = \frac{u^{*3}}{\kappa z} \tag{5.11}$$

and

$$k = \frac{u^{*2}}{C_\mu} \tag{5.12}$$

Eq. 5.12 is used as a turbulent kinetic energy boundary condition, which is placed just outside the turbulent core.

5.3 New $k-l$ Turbulence Model (KLN)

In the buffer layer and in the turbulent core of the oscillating wave boundary layer, there is a significant production of turbulent kinetic energy and a strong variability of this along the vertical direction. The balance between production and dissipation of turbulent kinetic energy strictly holds true at the border between the buffer layer and the turbulent core [10, 45]. The above-mentioned production of turbulent kinetic energy in the buffer layer and in the turbulent core influences the distribution of the turbulent kinetic energy along the vertical direction. In order to adequately represent the effects of the turbulent phenomena and the distribution of turbulent kinetic energy in the proximity of the bottom, it is necessary to solve the equations of motion and the turbulent kinetic energy equation both in the turbulent core and in the buffer layer (differently from the standard KLS turbulence model).

In the New $k-l$ turbulence model (KLN), the equations of motion are solved up to the buffer layer ($y^+ = 20$). The velocity boundary condition is placed in the buffer layer in the proximity of the viscous sublayer (at $y^+ = 10$) and it is calculated by the logarithmic law, Eq. 4.16.

The k-equation is solved up to the buffer layer in the proximity of the viscous sublayer, $y^+ = 10$ and its boundary condition is placed at the bottom, where k is zero.

Outside the oscillating wave boundary layer, the mixing length is a function of the first and second spatial derivative of the local maximum water surface elevation (5.7). In the oscillating wave boundary layer, the mixing length is defined by

$$l = \frac{\kappa u^* z}{C_\mu \sqrt{k}} \tag{5.13}$$

It is possible to obtain Eq. 5.13 by combining Eqs. 4.15 and 5.6. This relation arises by the hypothesis of the balance between production and dissipation of turbulent kinetic energy in all the turbulent core. This hypothesis strictly holds true at the border between the buffer layer and the turbulent core [10]. In Eq.

5.13, the friction velocity u^* is determined by introducing in the logarithmic law (Eq. 4.16) the flow velocity at the first calculation point, that is placed inside the buffer layer, at $y^+ = 20$.

5.4 Results and discussion

Three breaking wave test cases are numerically reproduced by using the two $k-l$ turbulence models. All the numerical simulations are carried out by using the new high-order shock capturing numerical scheme.

In the first model (KLS turbulence model), the mixing length is a function of the undisturbed water depth ($l = 0.1h$) as proposed by [6, 63]; the coefficient that multiplies the undisturbed water depth does not vary. The discretization of the vertical grid cells (called Grid1) adopted in the simulations carried out by the KLS turbulence model (presented in Section 5.2) is shown in Fig. 5.2. The motion equations are solved by starting from the turbulent core, where the first calculation grid cell is indicated by the number one in Fig. 5.2. At the lower face of this cell, placed at the border between the buffer layer and the turbulent core, the velocity boundary condition is calculated by the logarithmic law Eq. 4.16. At the lower and upper faces of the first calculation grid cell, the eddy viscosity is given by Eq. 4.15 ($\nu_T = \kappa u^* z$). At $y^+ = 90$, the turbulent kinetic energy boundary condition, given by Eq. 5.12, is imposed. The turbulent kinetic energy is calculated at the upper faces of each grid cell; the first face in which the turbulent kinetic energy equation is solved is the upper face of the cell indicated by number two in Fig. 5.2.

The spatial discretization step in the wave propagation direction is $\Delta x = 0.05m$, while 13 non uniform layers are adopted along the vertical direction.

In the simulations carried out by the second $k-l$ turbulence model (KLN), the oscillating wave boundary layer is discretized by using one grid cell in the buffer layer and two grid cells in the turbulent core. In this way, it is possible to solve the equations of motion and the turbulent kinetic energy equation also in the buffer layer, to adequately take into account the effects of the turbulent phenomena on the dissipation of the kinetic energy of the ensemble-averaged motion and the distribution of the turbulent kinetic energy along the vertical direction.

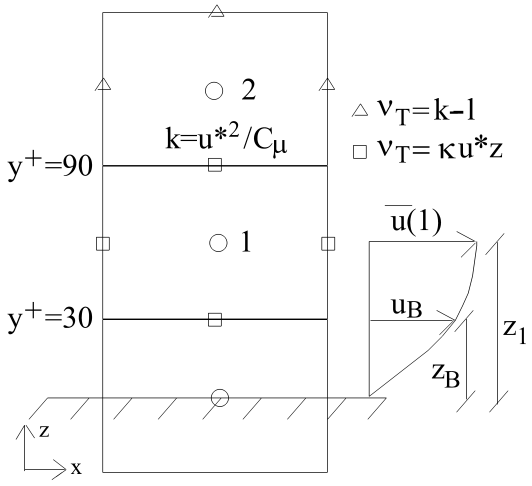

Figure 5.2: Grid1. Vertical discretization of the grid cells outside the buffer layer for simulations carried out by the standard $k-l$ turbulence model (KLS).

In Fig. 5.3, the vertical discretization (called Grid2) adopted in the simulations carried out by the KLN turbulence model (presented in Section 5.3) is shown. The lower face of the first computational grid cell is placed in the buffer layer at $y^+ = 10$, in the proximity of the viscous sublayer. Consequently, the equations of motion are solved also in the buffer layer ($y^+ = 20$). The velocity boundary condition u_B is placed at the lower face of the first computational grid cell (indicated with the number one in Fig. 5.3) and is calculated by the logarithmic law, Eq. 4.16. In the oscillating wave boundary layer (cells indicated with one, two and three in Fig. 5.3), the mixing length is given by Eq. 5.13. Outside the oscillating wave boundary layer, by starting from $y^+ = 80$, the mixing length is given by Eq. 5.7. The k-equation is solved by starting from the buffer layer, in the proximity of the viscous sublayer ($y^+ = 10$), to take into account the effects that turbulent phenomena have on the dissipation of the kinetic energy of the ensemble-averaged motion inside the oscillating wave boundary layer. The turbulent kinetic energy boundary condition is set equal to zero at the bottom ($z = 0m$). Outside the oscillating wave boundary layer, the eddy viscosity is given by Eq. 5.6.

The spatial discretization step in the wave propagation direction is $\Delta x = 0.05m$, while 18 non uniform layers are adopted along the vertical direction.

In Tab. 5.1, a synthetic description of the test cases of this chapter are described.

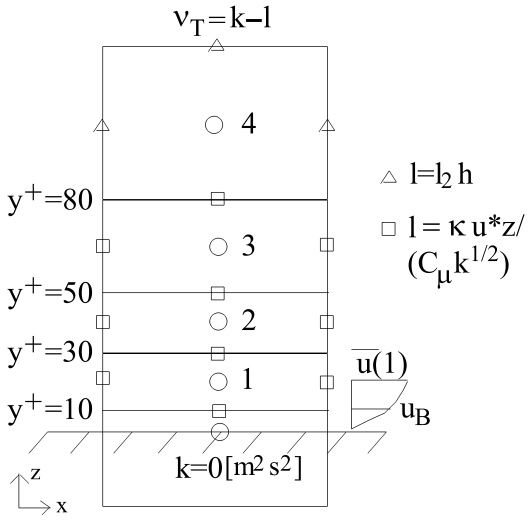

Figure 5.3: Grid2. Vertical discretization of the grid cells inside the buffer layer and turbulent core for the simulations carried out by the new $k-l$ turbulence model (KLN).

Test	Name	Turb. model	Numerical Scheme	Discret.	Note
Ting and Kirby [63]	Ting4	Standard $k-l$ KLS	5nd-order (WTENO + Exact Riemann S.)	Grid1	$l=0.1h$
Ting and Kirby [63]	Ting5	New $k-l$ KLN	5nd-order (WTENO + Exact Riemann S.)	Grid2	$l=l_2\cdot h$
Stive spilling [60, 61]	Stive2	Standard $k-l$ KLS	5nd-order (WTENO + Exact Riemann S.)	Grid1	$l=0.1h$
Stive spilling [60, 61]	Stive3	New $k-l$ KLN	5nd-order (WTENO + Exact Riemann S.)	Grid2	$l=l_2\cdot h$
Stive spilling-plunging [61]	Stivesp2	Standard $k-l$ KLS	5nd-order (WTENO + Exact Riemann S.)	Grid1	$l=0.1h$
Stive spilling-plunging [61]	Stivesp3	New $k-l$ KLN	5nd-order (WTENO + Exact Riemann S.)	Grid2	$l=l_2\cdot h$

Table 5.1: Test cases with $k-l$ turbulence models.

5.4.1 Ting and Kirby test case of a spilling breaker with a cnoidal wave

In this Section, a Ting and Kirby test case for a spilling breaking wave [63] is numerically reproduced. The description of the laboratory test is in Section 4.2.

Figs. 5.4, 5.5 and 5.6 show the numerical results obtained by the standard $k-l$ turbulence model (KLS) on Grid1. As showed by Fig. 5.4, the local maximum water surface elevation at the wave breaking point is slightly underestimated and the wave breaking point is shifted offshorward. In the KLS turbulence model, the mixing length is a function of the undisturbed water depth ($l=0.1h$) and the coefficient that multiplied h does not vary. Consequently, the mixing length does not take adequately into account the different turbulent phenomena that occur in the distinct zones shown in Fig. 5.1.

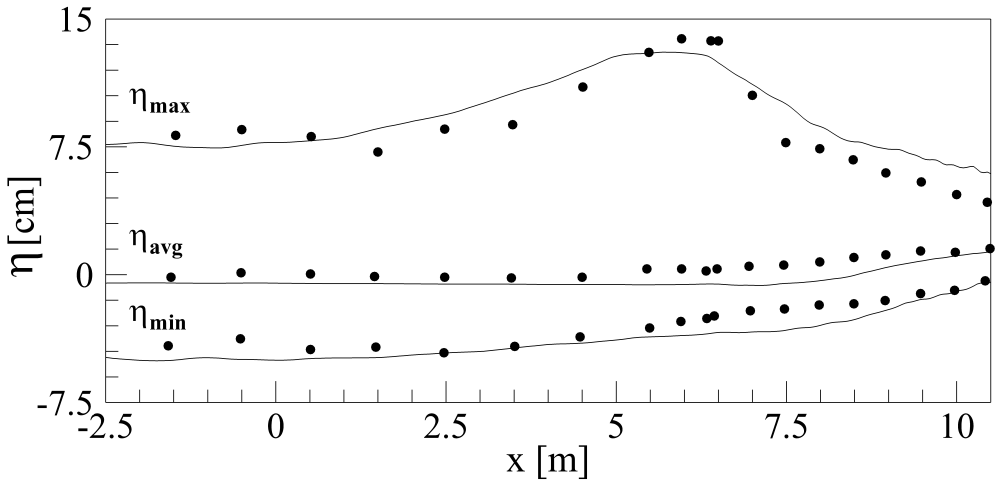

Figure 5.4: Ting4: local minimum, average and maximum water surface elevations. Experimental measurements • [63] and numerical results − with the standard $k-l$ turbulence model (KLS).

The time mean vertical distribution of the normalized turbulent kinetic energy and horizontal flow velocity (undertow) are shown in Figs. 5.5 and 5.6, respectively. In both figures, letters (a)-(e) refers to the results relative to $x = 7.27m$, $x = 7.88m$, $x = 8.5m$, $x = 9.07$ and $x = 9.67m$, respectively. In all figures, the values of the time mean turbulent kinetic energy and horizontal flow velocity are normalized as a function of the time mean quantity $\sqrt{g\overline{\overline{H}}}$ as follow

$$k'' = \sqrt{\frac{\overline{k}}{g\overline{\overline{H}}}}, \quad u'' = \frac{\overline{u}}{\sqrt{g\overline{\overline{H}}}}, \quad z'' = \frac{z-\overline{\eta}}{\overline{H}} \tag{5.14}$$

As can be notice from Figs. 5.5(a)-(d), the normalized turbulent kinetic energy is overestimated with respect to the experimental measurements. Only at $x = 9.67m$ the normalized turbulent kinetic energy is well predict, as shown in Fig. 5.5(e). The normalized horizontal flow velocity distributions are overestimated until $x = 8.50m$ (Figs. 5.6(a)-(c)); at $x = 9.06m$ and $x = 9.67m$ (Figs. 5.6(d)-(e)), the normalized horizontal flow velocity distributions are underestimated near the bottom and overestimated near the free surface.

Under breaking waves, the time mean horizontal flow velocity is characterized by onshore directed velocities, near the free surface and offshore directed velocities near the bottom; this phenomenon is usually defined undertow.

The reason why this KLS turbulence model is not able to correctly predict the wave height and the distribution of the turbulent kinetic energy and flow velocity

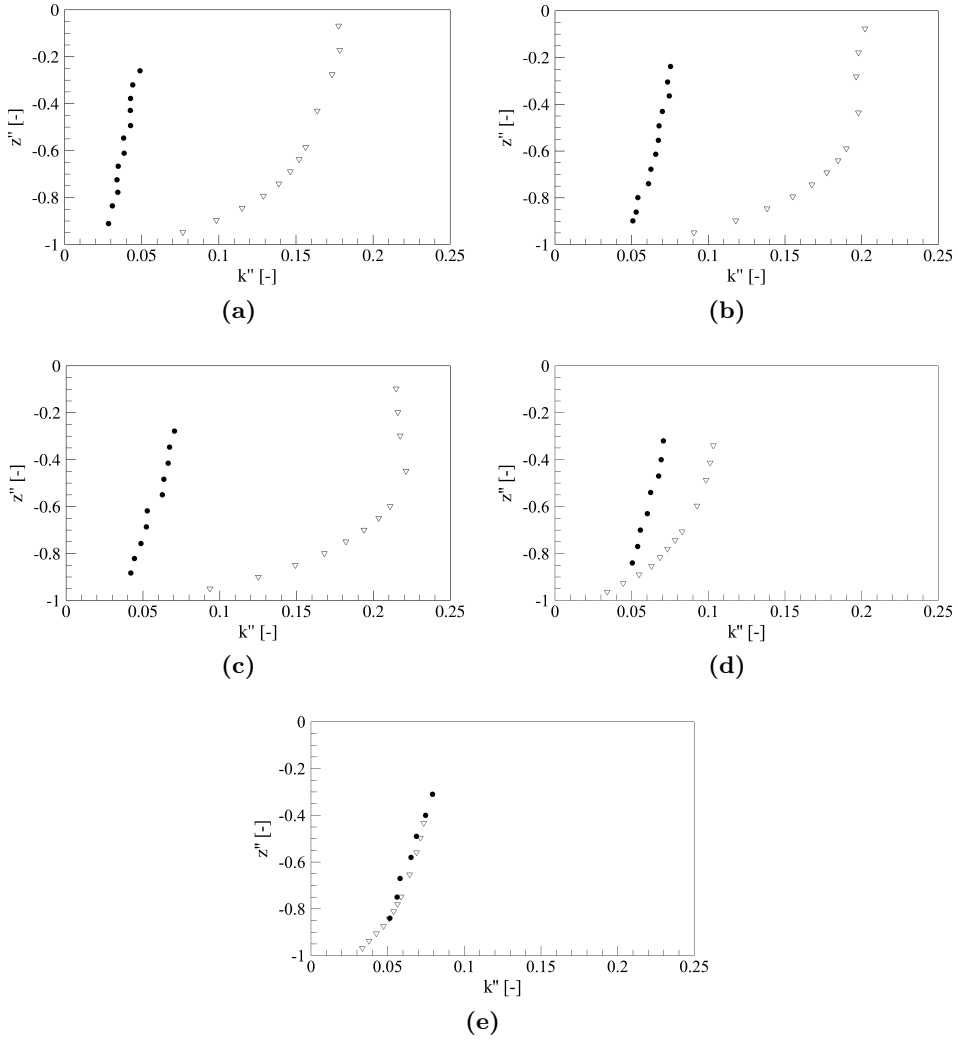

Figure 5.5: Ting4: time mean vertical distribution of the normalized turbulent kinetic energy at (a) $x = 7.27m$, (b) $x = 7.88m$, (c) $x = 8.5m$, (d) $x = 9.07m$ and (e) $x = 9.67m$. Experimental measurements • [63] and numerical results ▽ with the standard $k - l$ turbulence model (KLS).

can be attributed to three different reasons: a too simplified representation of the turbulent kinetic energy dissipation; the fact that the turbulent kinetic energy is calculated only outside the oscillating wave boundary layer; the fact that the equations of motion are not solved in the zone nearest to the bottom (viscous and buffer layers). By using the same coefficient for the mixing length in all the domain, the turbulence model is not able to differ the behaviour of the turbulent kinetic energy dissipation in the distinct zones. In this model, the equations of motion are solved by starting from the turbulent core ($y^+ = 60$) and the turbulent kinetic energy equation is solved by starting from outside the turbulent core ($y^+ > 90$). Furthermore (as already said), a simplified formulation for the

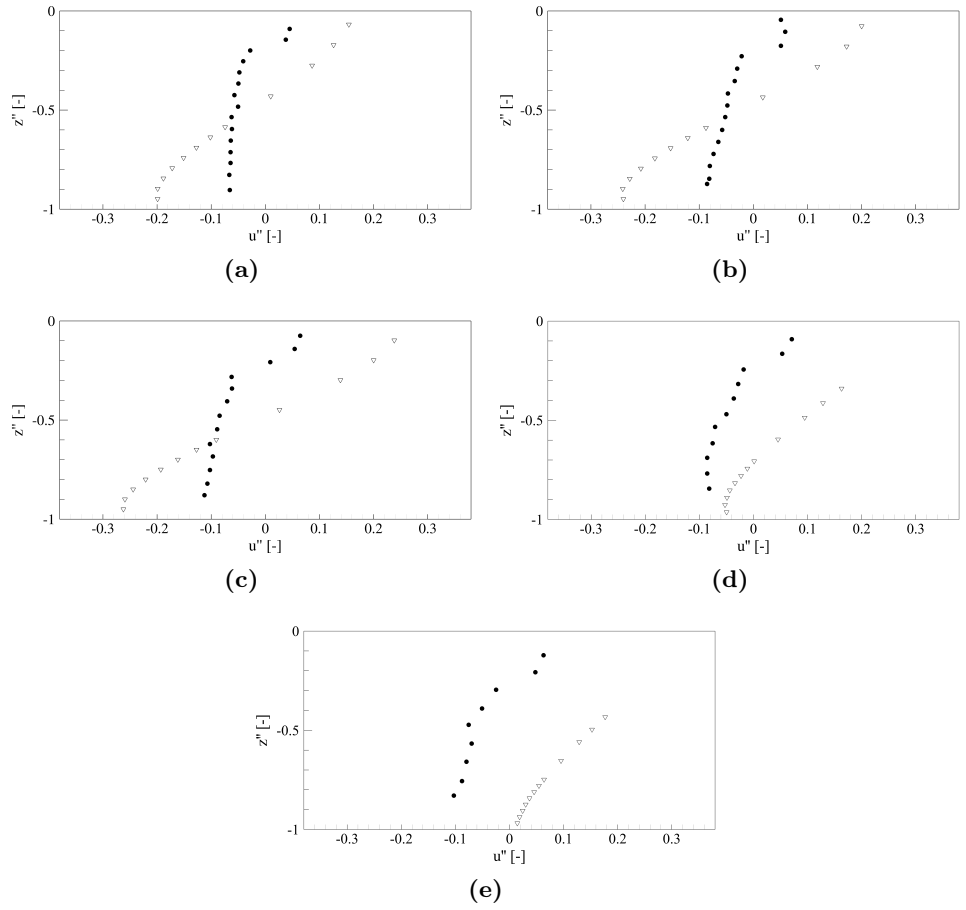

Figure 5.6: Ting4: time mean vertical distribution of the normalized horizontal flow velocity at (a) $x = 7.27m$, (b) $x = 7.88m$, (c) $x = 8.5m$, (d) $x = 9.07m$ and (e) $x = 9.67m$. Experimental measurements • [63] and numerical results ▽ with the standard $k - l$ turbulence model (KLS).

eddy viscosity is used in the turbulent core of the oscillating wave boundary layer.

The vertical distribution of the turbulent kinetic energy is strongly influenced by its production in the turbulent core and the buffer layer of the oscillating wave boundary layer (as well as on the breaking wave fronts). For this reason, it is necessary to solve the equations of motion and also the turbulence kinetic energy equation inside the oscillating wave boundary layer.

In conclusion, as shown by the numerical results, the standard $k-l$ turbulence model, in which the mixing length is the one proposed in the literature [6] and the near bed discretization is the one described in Section 5.2, is not able to correctly predict the wave height at the wave breaking point and in the surf zone and is not able to take into account the different turbulent phenomena that occur in the distinct zones of the domain.

From what has been written before, comes the need to verify if, by solving the equations of motion and the turbulent kinetic energy equation in the turbulent core and in the buffer layer of the oscillating wave boundary layer and by modifying the closure relation for the mixing length, it is possible to improve the numerical results with respect to the ones produced by the standard KLS turbulence model.

In order to take into account the considerable variability of the production and dissipation of turbulent kinetic energy in the zone before the wave breaking point, around the wave breaking point, in all the surf zone and at the bottom (5 zones shown in Fig. 5.1), in the new $k-l$ turbulence model KLN, the mixing length is calculated as a function of the spatial first and second derivative of the local maximum water surface elevation. The turbulent kinetic energy equation is solved also in the buffer layer and in the turbulent core. In Figs. 5.7, 5.8 and 5.9, the results obtained with the new $k-l$ turbulence model (KLN) on Grid2 are shown.

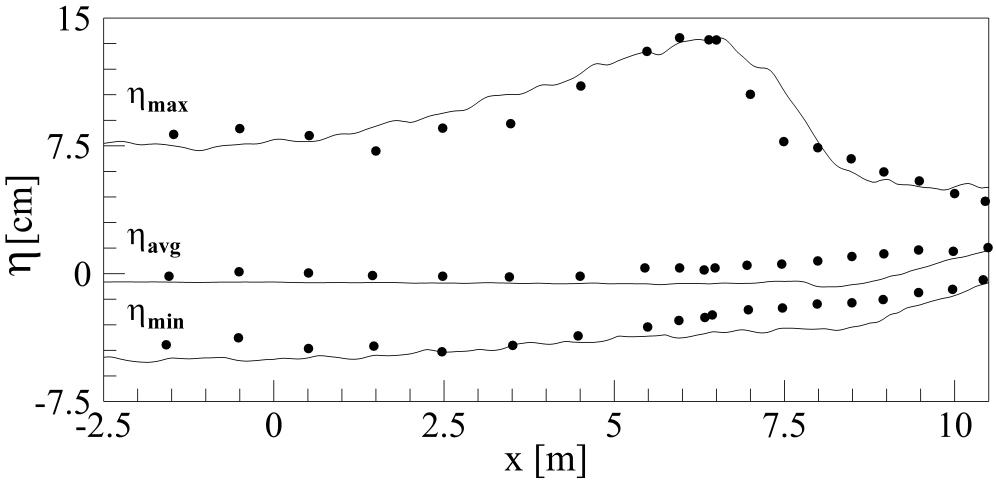

Figure 5.7: Ting5: local minimum, average and maximum water surface elevations. Experimental measurements • [63] and numerical results − with the new $k-l$ turbulence model (KLN).

Form Fig. 5.7, it is possible to notice that by this model the local maximum water surface elevation is well predicted, the wave breaking point is correctly located and the decrease of the wave height in the surf zone is quite in good agreement with the experimental measurements.

As shown in Fig. 5.8, the time mean vertical distribution of the normalized

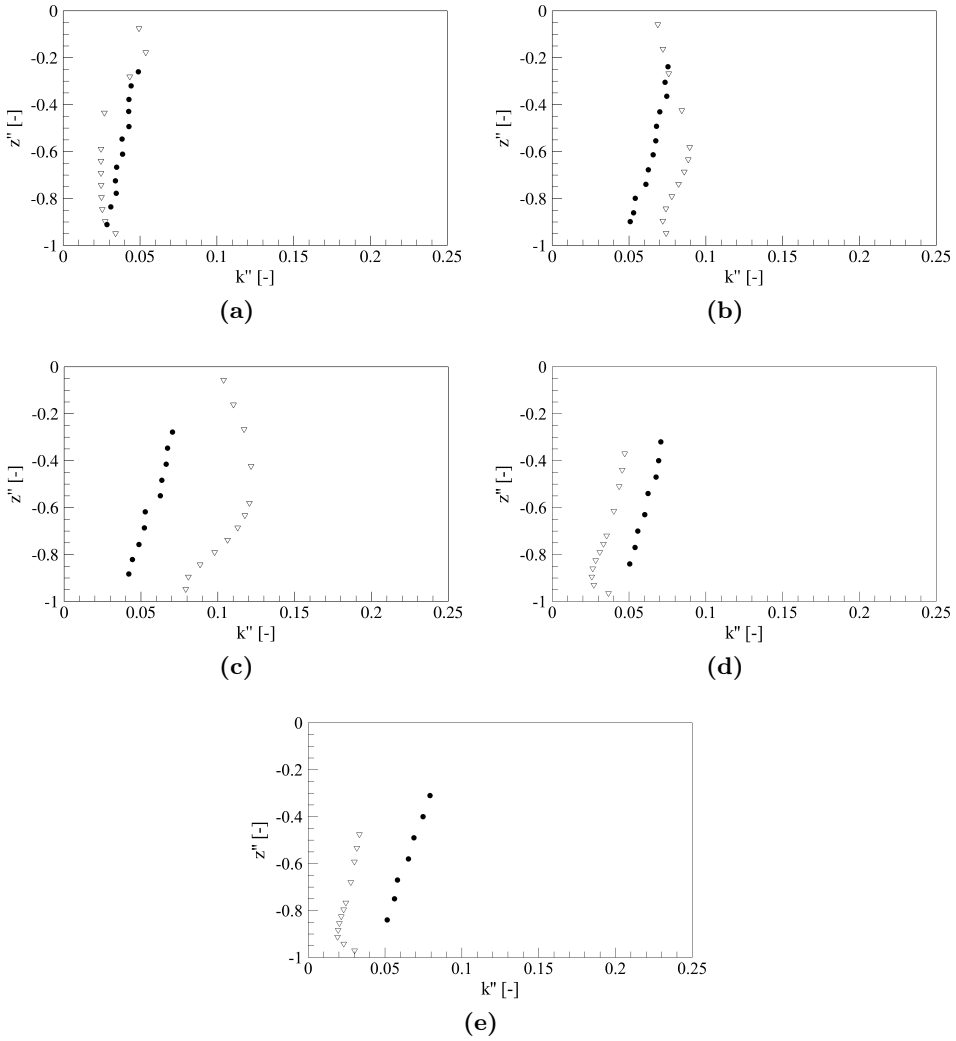

Figure 5.8: Ting5: time mean vertical distribution of the normalized turbulent kinetic energy at (a) $x = 7.27m$, (b) $x = 7.88m$, (c) $x = 8.5m$, (d) $x = 9.07m$ and (e) $x = 9.67m$. Experimental measurements • [63] and numerical results $\triangledown$ with the new $k-l$ turbulence model (KLN).

turbulence kinetic energy is quite in good agreement with the experimental measurements at $x = 7.27m$, $x = 7.88m$, $x = 9.07m$ (Figs. 5.8(a), (b) and (d)). At $x = 8.5m$, the above quantity is overestimated, similarly to the result obtained by the KLS turbulence model (see Fig. 5.5(c)); while at $x = 9.67m$ (Fig. 5.8(e)), the turbulent kinetic energy is slightly underestimated with respect to the experimental measurements.

The numerical results in terms of the normalized horizontal flow velocity agree well with the experimental measurements at $x = 7.27m$ (Figs. 5.9(a)); in the following two points (Figs. 5.9(b) and (c)) the numerical results overestimate the experimental values; in the last two points (Figs. 5.9(d) and (e)) the experimental

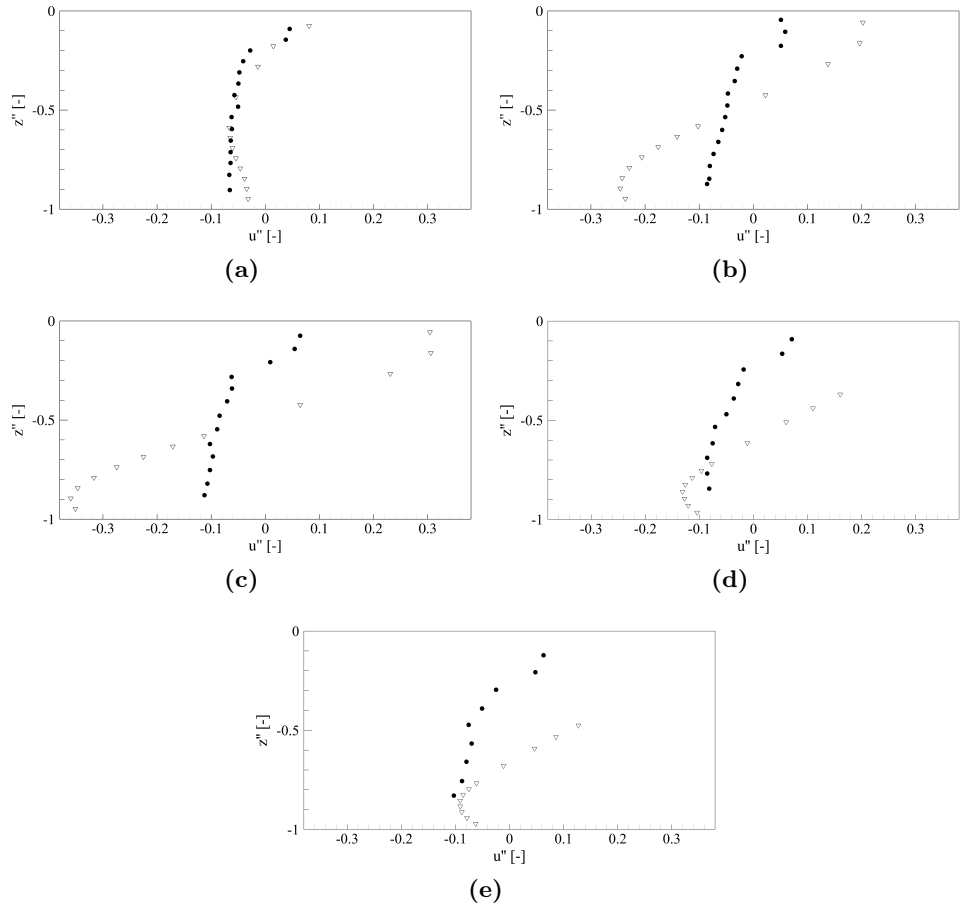

Figure 5.9: Ting5: time mean vertical distribution of the normalized horizontal flow velocity at (a) $x = 7.27m$, (b) $x = 7.88m$, (c) $x = 8.5m$, (d) $x = 9.07m$ and (e) $x = 9.67m$. Experimental measurements • [63] and numerical results ▽ with the new $k - l$ turbulence model (KLN).

values are overestimated at the free surface and are underestimated near the bottom.

In Fig. 5.10(a), an instantaneous field of the turbulent kinetic energy obtained by the proposed KLN turbulence model is shown. In Fig. 5.10(b), an instantaneous velocity field is shown in which one vector every two is drawn. These snapshots are taken after 75 subsequent waves, when the results reach a quasi-steady state ($T_s = 150s$).

The turbulent kinetic energy reaches maximum values in correspondence of the breaking wave fronts, in particular at $x = 7.0m$ and $x = 10.5m$, as shown in Fig. 5.10(a). The turbulent kinetic energy is produced mainly at the wave breaking fronts and minimally at the bottom in correspondence of the wave breaking fronts. This produced quantity is transported and diffused in the surf zone.

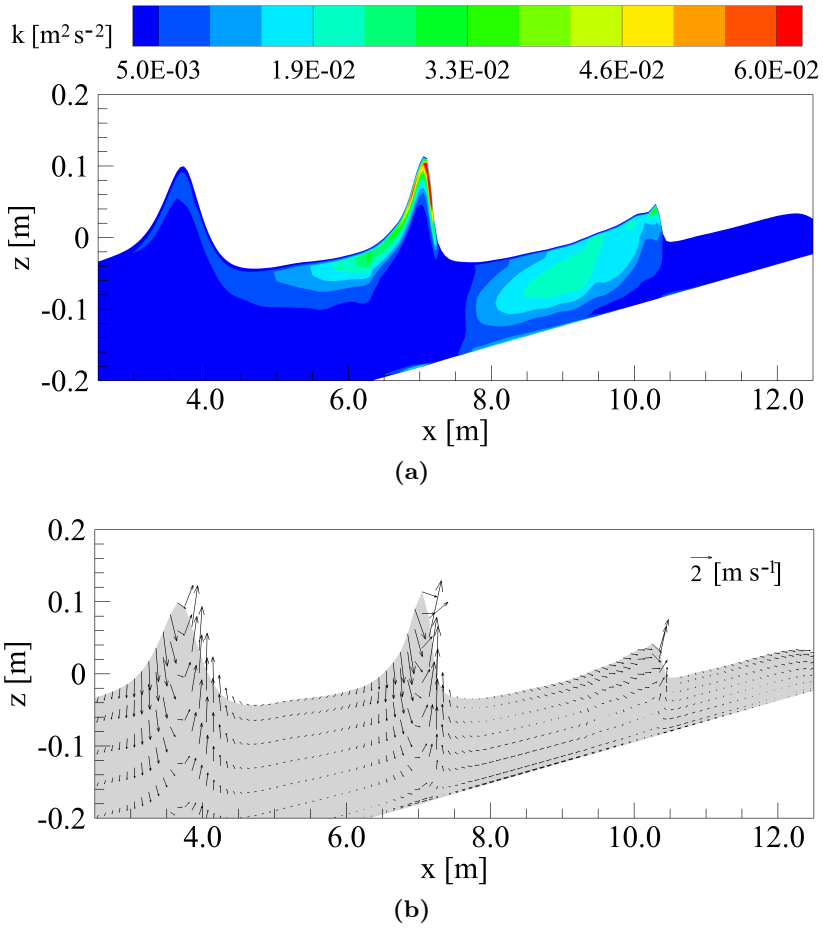

Figure 5.10: Ting5: (a) Instantaneous wave field with contours of turbulent kinetic energy. (b) Instantaneous velocity field, one vectors every two is drawn. ($T_s = 150s$)

5.4.2 Stive test case of a spilling breaker with a monochromatic wave

In this Section, an experimental test of a spilling breaker by Stive [60, 61] is numerically reproduced by the high-order numerical scheme presented in Chapter 3. The description of the laboratory test is presented in Section 4.2.2.

In Fig. 5.11, the numerical results obtained by the KLS turbulence model on Grid1 is compared against the experimental measurements in terms of wave height.

As shown in Fig. 5.11, the wave breaking point obtained by the numerical simulation is shifted offshoreward and the wave height is underestimated. In the KLS turbulence model, the mixing length is a function of the undisturbed water depth ($l = 0.1h$) and the coefficient that multiplied h does not vary. Consequently, the mixing length does not take into account the different way to produce and

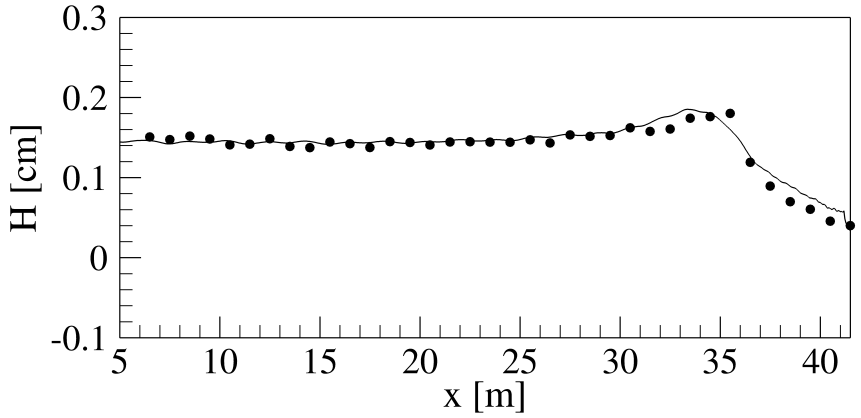

Figure 5.11: Stive2: wave height. Experimental measurements • [60, 61] and numerical results solid line with the standard $k-l$ turbulence model (KLS).

dissipate turbulent kinetic energy before the wave breaking point, around the wave breaking point and after the wave breaking point in the surf zone (Zones 1-4 in Fig. 5.1). Furthermore, the equations of motion are solved by starting from the turbulent core ($y^+ = 60$) and the k-equation is solved out the oscillating wave boundary layer ($y^+ > 90$). For this reason, this model does not consider the effects that the turbulent phenomena have in the dissipation of the kinetic energy of the ensemble-averaged motion and production of turbulent kinetic energy in the oscillating wave boundary layer.

The KLS turbulence model does not correctly represent the wave height and the location of the wave breaking point, because the mixing length defined in the literature [6, 63] is not able to differ the behaviour of the turbulence model before the wave breaking point, around the wave breaking point and in the surf zone.

In the new $k-l$ turbulence model (KLN), the equations of motion are solved also in the buffer layer ($y^+ = 20$) and the k-equation is solved by starting from the buffer layer, in the proximity of the viscous sublayer ($y^+ = 10$). Furthermore, the mixing length is a function of the first and second spatial derivative of the local maximum water surface elevation.

In Fig. 5.12, the wave height obtained with the KLN turbulence model on Grid2 is shown and compared with the experimental measurements.

The wave breaking point is correctly evaluated and the wave height at the wave breaking point is slightly overestimated. In the surf zone, the wave height correctly decreases. By comparing Fig. 5.11 and Fig. 5.12, it can be remarked that the (KLN) turbulence model gives numerical results that are in better agreement with

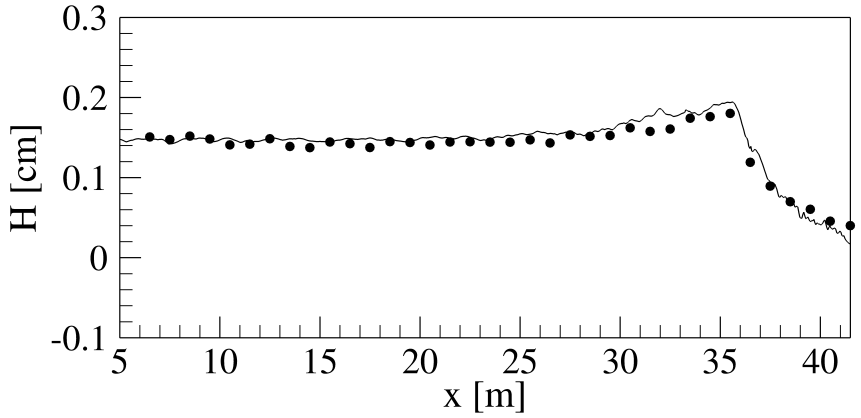

Figure 5.12: Stive3: wave height. Experimental measurements • [60, 61] and numerical results solid line with the new $k-l$ turbulence model (KLN).

the experimental measurements that the ones obtained by the KLS turbulence model.

In Fig. 5.13(a), instantaneous field of turbulent kinetic energy is shown. In Fig. 5.13(b), an instantaneous velocity field is shown in which one vector every two is drawn. These snapshots are taken after about 100 subsequent waves, when the results reach quasi-steady state ($T_s = 180s$).

The maximum value of the turbulent kinetic energy is just in the surf zone, in correspondence of the breaking wave fronts. In the oscillating wave boundary layer in correspondence of the wave breaking fronts, there is very little production of turbulent kinetic energy.

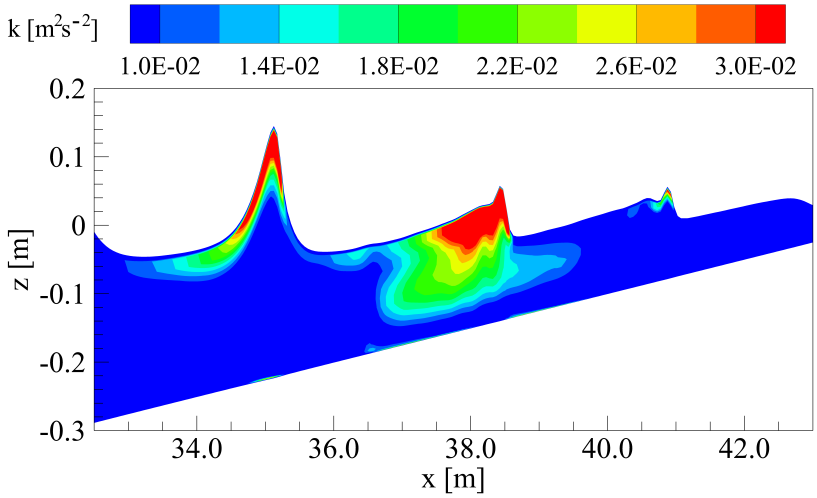

(a)

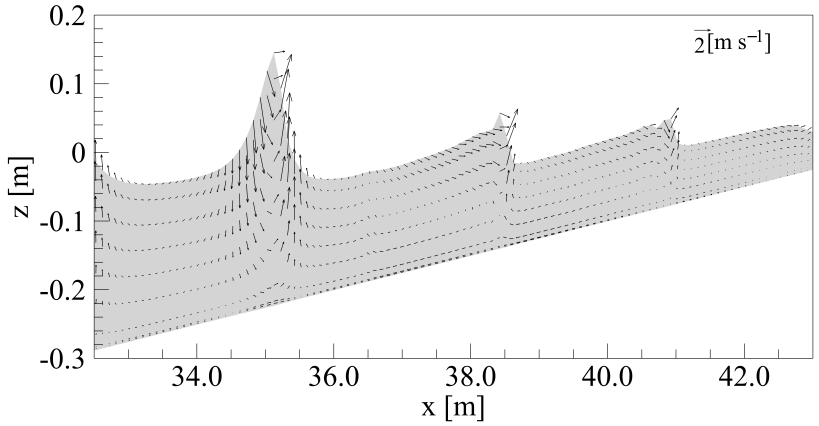

(b)

Figure 5.13: Stive3: (a) Instantaneous wave field with contours of turbulent kinetic energy. (b) Instantaneous velocity field, one vectors every two is drawn. ($T_s = 180s$)

5.4.3 Stive test case of a spilling-plunging breaker with a monochromatic wave

In this Section, an experimental test of a spilling/plunging breaker by Stive [61] is numerically reproduced with the high-order numerical scheme presented in Chapter 3. The description of the laboratory test is presented in Section 4.2.3.

In Fig. 5.14, the numerical results obtained by the KLS turbulence model on Grid1 is compared against the experimental measurements in terms of wave height.

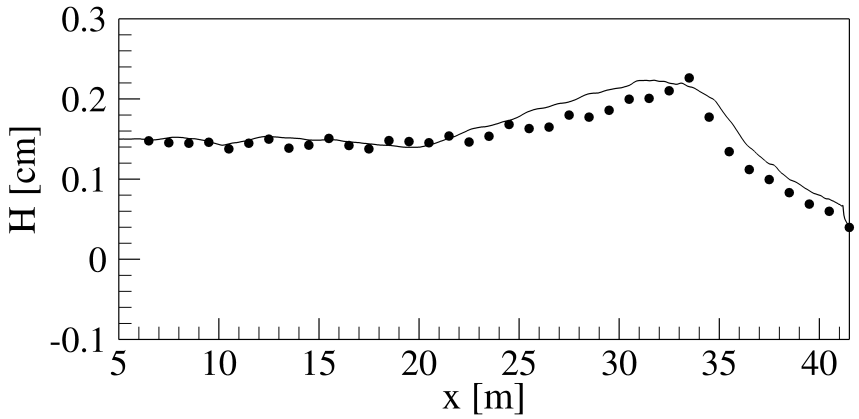

Figure 5.14: Stivesp2: wave height. Experimental measurements • [61] and numerical results solid line with the standard $k - l$ turbulence model (KLS).

The wave height shown in the Fig. 5.14 is underestimated before the wave breaking point and the position of the wave breaking point is shifted offshoreward with respect to the one obtained by the laboratory test. Before the wave breaking

point, the wave height is slightly overestimated. Through this model it is not possible to take into account the different turbulent phenomena that occur before and after the wave breaking point and near to the bottom.

In Fig. 5.15, the wave height obtained by the new $k-l$ turbulence model (KLN) on Grid2 is presented and compared with the experimental measurements.

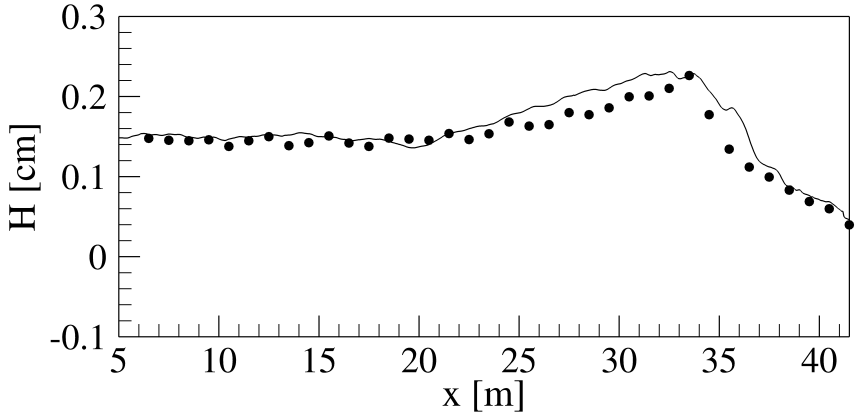

Figure 5.15: Stivesp3: wave height. Experimental measurements • [61] and numerical results solid line with the new $k-l$ turbulence model (KLN).

In this case, the breaking point is correctly located. The wave height at the breaking point is correctly evaluated, while it is slightly overestimated before and after the wave breaking point.

In Fig. 5.16(a)-(b), instantaneous fields of turbulent kinetic energy and an instantaneous velocity field are shown. These snapshots are taken after about 60 subsequent waves, when the results reach quasi-steady state ($T_s = 179s$).

The turbulent kinetic energy assumes the maximum values on the breaking waves, at $x = 33.5m$ and $x = 38.5m$ (see Fig. 5.16(a)). The production of turbulent kinetic energy in the oscillating wave boundary layer is very small.

5.5 Conclusions

In the Subsection 5.4, the results obtained by numerically reproducing three different test cases with the two $k-l$ turbulence models (the KLS turbulence model and the KLN turbulence model).

In KLS turbulence model, the first point, nearest to the bottom, in which the equations of motion are solved, is located in the turbulent core ($y^+ = 60$),

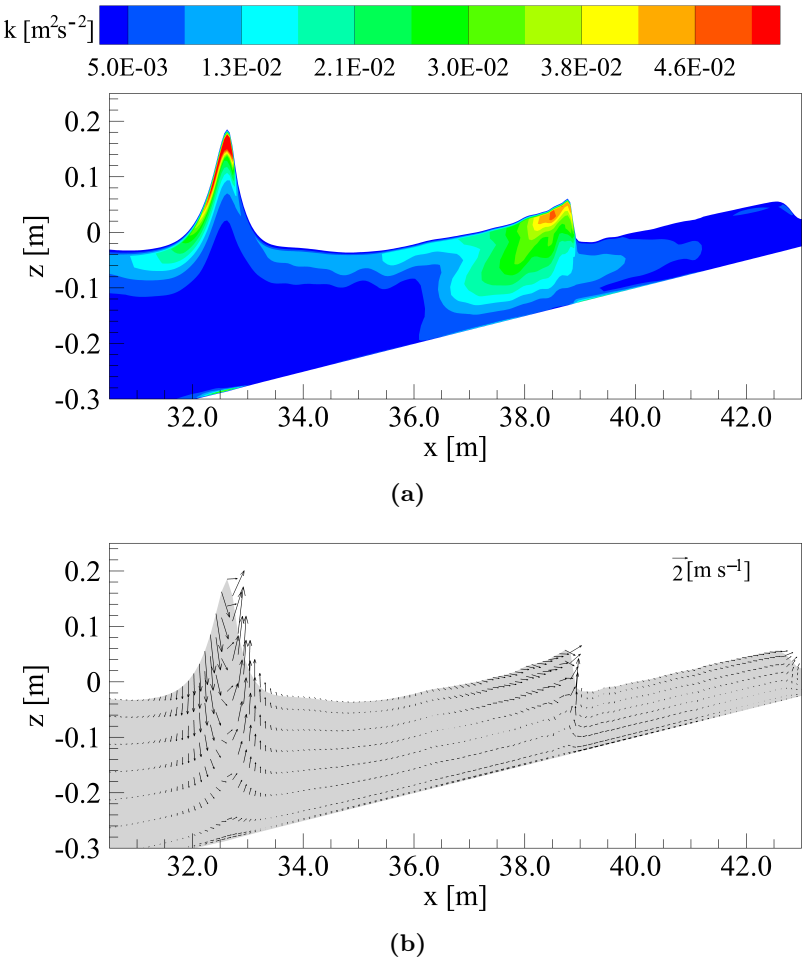

Figure 5.16: Stivesp3: (a) Instantaneous field with contours of turbulent kinetic energy. (b) Instantaneous velocity field, one vectors every two is drawn. ($T_s = 179s$)

while the turbulent kinetic energy equation is solved outside the oscillating wave boundary layer ($y^+ > 90$). The velocity boundary condition is placed at the border between the buffer layer and the turbulent core ($y^+ = 30$) and it is calculated by the logarithmic law (Eq. 4.17). The boundary condition for the turbulent kinetic energy is placed in the turbulent core ($y^+ = 90$) and it is calculated by assuming the balance between production and dissipation of turbulent kinetic energy. The mixing length is a function of the undisturbed water depth through a constant coefficient. The eddy viscosity in the oscillating wave boundary layer as a function of the friction velocity and it is calculated by assuming true the balance between production and dissipation of turbulent kinetic energy in all the turbulent core. In the KLN turbulence model, the first point nearest to the bottom in which the equations of motion is solved is in the buffer layer ($y^+ = 20$). The velocity boundary condition is placed in the buffer layer, in the proximity of the

viscous sublayer ($y^+ = 10$). The turbulent kinetic energy equation is solved by starting from the buffer layer, in the proximity of the viscous sublayer ($y^+ = 10$). Outside the oscillating wave boundary layer, a new formula for the mixing length is proposed as a function of the first and second spatial derivatives of the local maximum water surface elevation. In the oscillating wave boundary layer, the mixing length is calculated as a function of the friction velocity (according to Eq. 5.13), by assuming true the hypothesis of the balance between production and dissipation of turbulent kinetic energy in all the turbulent core.

It has been demonstrated by the numerical simulations that the standard $k-l$ turbulence model (KLS), in which the equations of motion are solved by starting from the buffer layer and the turbulent kinetic energy equation is solved outside the oscillating wave boundary layer (Section 5.2), is not able to correctly predict the wave height at the wave breaking point and in the surf zone and is not able to take into account the different turbulent phenomena that occur in the water column as the wave propagates.

The numerical results demonstrated that the new $k - l$ turbulence model (KLN) is able to represent in different way the turbulence phenomena before and around the wave breaking point and in the surf zone. In particular, it has been demonstrated that by solving the equations of motion in the buffer layer and the k-equation in the proximity of the viscous sublayer, it is possible to better take into account the effects that the turbulent phenomena have in the dissipation of the kinetic energy of the ensemble-averaged motion in the oscillating wave boundary layer [32]. In this model, the hypothesis of the balance between production and dissipation of turbulent kinetic energy is assumed valid in all the turbulent core. The mixing length is calculated in two different ways inside and outside the oscillating wave boundary layer. Indeed, inside the oscillating wave boundary layer it is calculated by the above-mentioned hypothesis, while outside the oscillating wave boundary layer the mixing length is calculated as a function of the spatial first and second derivative of the local maximum water surface elevation.

From the comparison between the numerical results obtained by the standard $k - l$ turbulence model and the new $k - l$ turbulence model, it is evident the

necessity of adequately represent the different turbulent phenomena that take place before and after the wave breaking point. It is also clear that the turbulent phenomena should be represented differently in the distinct zones. In addition, the numerical results show that the equations of motion and the turbulent kinetic energy equation must be necessary solved also in the buffer layer of the oscillating wave boundary layer.

Chapter 6

$k-\omega$ Turbulence Model under breaking waves

In order to have an adequate representation of the turbulent phenomena both in the oscillating wave boundary layer and on the wave breaking fronts, it is necessary take into account the considerable variability of the production and dissipation of the turbulent kinetic energy along the water column and in the surf zone. For this reason, it is clear that it is necessary an adequate and laborious calibration of the mixing length with the $k-l$ turbulence model. The definition of the mixing length in the oscillating wave boundary layer leads to the assumption that the balance between production and dissipation of turbulent kinetic energy holds true in all the turbulent core. The above-mentioned balance strictly holds true at the interface between the turbulent core and the buffer layer [10]. In the previous Chapter (Chapter 5), it has been demonstrated the importance of represent scrupulously the effects that the turbulent phenomena have in the dissipation of the kinetic energy of the ensemble-averaged motion in the proximity of the bottom. It is necessary to remove the hypothesis of the balance between production and dissipation of turbulent kinetic energy in all the turbulent core for the definition of the mixing length. Hence, the need to develop a more general two-equations turbulence model ($k-\omega$) which is able to overcome the drawbacks of the new $k-l$ turbulence model and take into account the effects of the turbulent phenomena in the oscillating wave boundary layer, till the border between the buffer layer and the viscous sublayer.

In presence of coastal works, their interaction with the waves produces hydrodynamic fields characterized by unsteady quasi-periodic vortex structures and stochastic turbulent fluctuations. The quasi-periodic vortex structures are unsteady phenomena that arise from the interaction between the fluid and the coastal works. The stochastic turbulent fluctuations are superimposed on the unsteady quasi-periodic motion of the vortex structures.

By following the suggestion of Bosh and Rodi [5], the generic instantaneous hydrodynamic quantity $\Theta(t)$ is separated into three components. The first component is represented by the value of the hydrodynamic quantity $\overline{\Theta}(t)$, whose time periodicity is related only to the wave periodicity. The second component $\tilde{\Theta}(t)$ is related to the quasi-periodicity of the vortex structures produced by the interaction between fluid and coastal works. The third component $\Theta'(t)$ is the turbulent fluctuation. Always in accordance with Bosh and Rodi [5], the sum of $\overline{\Theta}(t)$, related to the periodicity of the wave, and $\tilde{\Theta}(t)$, related to the quasi-periodicity of the vortex structures, gives rise to the ensemble-averaged component, which is calculated by numerically solving the ensemble-averaged motion equations. In this context, the complete spectrum of the stochastic turbulent motion is simulated by a statistical turbulence model. The models coherent with the above-mentioned approach are named, in the literature, Unsteady Reynolds-Averaged Navier-Stokes Equations (URANS) models.

It is necessary recalling the fact that the product between the ensemble-averaged velocity and the divergence of the Reynolds stress tensor represents the dissipation of kinetic energy of the ensemble-averaged motion. An overestimation of the Reynolds stress tensor (that occurs in the ensemble-averaged Navier-Stokes equations) produces an excess of dissipation of the kinetic energy of the ensemble-averaged motion.

In the direct simulation of the quasi-periodic vortex structures, mainly due to the interaction between the waves and coastal works, it is necessary to solve the equations of motion also inside the turbulent core and the buffer layer (with small spatial discretization steps in the proximity of the obstacle walls) and to adequately represent the turbulent phenomena in the proximity of the walls.

Franke and Rodi [21] have shown that the occurrence and quality of the vortex structures prediction strongly depend on the turbulence model used. From

a general point of view, traditionally one-equation and two-equation turbulence models [6, 18–20, 41, 42, 44, 45, 47, 58, 72, 73] were found to severely underpredict the strength of the vortex structures, mainly because of the production of turbulent kinetic energy. When the production of turbulent kinetic energy is too high, the Reynolds stress tensor is overestimated. The product between the ensemble-averaged velocity and the divergence of the stress tensor represents the dissipation of the kinetic energy of the ensemble-averaged motion. An overestimation of the Reynolds stress tensor produces an excess of dissipation of the kinetic energy of the ensemble-averaged motion. Consequently, by using turbulence models that produce an excessive production of turbulent kinetic energy, the unsteady quasi-periodic vortex structures (beside all of the stochastic turbulent fluctuations) are expelled from the direct simulations of the ensemble-averaged motion.

In the context of the URANS model, two-equations $k-\omega$ turbulence model [49, 70, 71], is able to represent the turbulent phenomena, so that the numerical models can directly simulate the unsteady quasi-periodic vortex structures, and is able to also give correct boundary conditions at the bottom and does not need to define a specific mixing length. The turbulent kinetic energy dissipation ε (in the $k-\varepsilon$ turbulence model [20, 41, 42, 45, 58, 72]) does not admit boundary conditions at the bottom; the specific dissipation rate ω admits bottom boundary condition [49, 70, 71].

One of the first $k-\omega$ present in the literature is proposed by Wilcox [70] and it is used to simulate compressible flow around an airfoil. Wilcox proposed a boundary condition for the specific dissipation rate ω that incorporates the effects of the surface roughness. As underlined by several authors [49, 71] the Wilcox model has the tendency to overestimate the eddy viscosity when the production of turbulent kinetic energy is significantly increased and the specific dissipation rate is not able to reduce the growth of turbulent kinetic energy.

Wilcox [71] proposed a $k-\omega$ model in which the eddy viscosity is limited. Furthermore, a cross-diffusion term is added in ω-equation to enhance ω production in order to increase the dissipation of turbulent kinetic energy.

Mayer and Madsen [48] have used the Wilcox $k-\omega$ turbulence model [70] in the simulation of the breaking waves. They have demonstrated that this $k-\omega$

turbulence model produces an excessive production of turbulent kinetic energy in the zone between the breaking wave fonts and the oscillating wave boundary layer. This excessive production of turbulent kinetic energy induces an overestimation of the Reynolds stress tensor. In the numerical simulations of the wave and velocity fields, the overestimation of the Reynolds stress tensor produces an excessive reduction of the wave height and the wave breaking point is shifted offshoreward.

In this thesis, a new $k-\omega$ turbulence model is proposed for the simulation of the breaking waves and the interaction between waves and coastal works in the breaking waves. The k and ω equations are formulated in integral contravariant form on a generalized curvilinear coordinate system.

It is necessary to recall that in $k-\omega$ model the eddy viscosity is the ratio of turbulent kinetic energy to specific dissipation rate. In order to limit the production of the turbulent kinetic energy in the zone between the breaking wave fronts and the oscillating wave boundary layer, in the new $k-\omega$ turbulence model, the denominator of the eddy viscosity is calculated as the maximum value between three terms: the first one is directly calculated by the ω-equation; the second one is a function of absolute value of the strain rate tensor and the absolute value of the vorticity tensor; the third value is calculated by the product between the absolute value of the strain rate tensor and a coefficient that is activated as a function of the zone in which it is calculated. This coefficient is determined by the local maximum water depth and is increased in the surf zone, where the local maximum water depth is reduced. In such a way, the behaviour of the model before and after the wave breaking point is differentiated.

In order to further reduce the production of the turbulent kinetic energy in the zone between the breaking wave fronts and the oscillating wave boundary layer, in the new $k-\omega$ model, a dynamic coefficient for the dissipation of ω is added by following the line proposed by Yakhot [72]. In the new $k-\omega$ turbulence model proposed in this thesis, a dynamic procedure (which is a function of the strain rate tensor) for calculating this coefficient is introduced. For high values of the strain rate tensor, the coefficient that multiplies the dissipation of ω decreases, by further reducing the production of turbulent kinetic energy.

The velocity boundary condition is calculated without using logarithmic laws and it is placed at the border between the buffer layer and the viscous sublayer.

The boundary condition for the turbulent kinetic energy is null directly at the bottom. The boundary condition for the specific dissipation rate is placed at the bottom and it is a function of the bottom roughness and the friction velocity (the friction velocity is calculated by the viscous stress at the border between the viscous sublayer and the buffer layer). The k and ω-equations are solved starting from the border between the viscous sublayer and the buffer layer. Since the turbulent equations are solved near the bottom, it is possible to directly simulate the unsteady quasi-periodic vortex structures due to the interaction between breaking waves and coastal works.

This Chapter is organized as follow: in Section 6.1 the existing $k-\omega$ is presented; in Section 6.2 the new $k-\omega$ proposed in this thesis and the new boundary conditions for the turbulent kinetic energy and the specific dissipation rate are presented; in Section 6.3 some numerical tests are reproduced by using the new $k-\omega$ turbulence model; in Section 6.4, some conclusive considerations are made about the use of the new $k-\omega$ turbulence model.

6.1 Existing $k-\omega$ Turbulence Model

Kolmogorov [40] proposed the first two-equation turbulence model. He chose the turbulent kinetic energy k as the first turbulence parameter and the dissipation rate of k per unit k, indicated by ω, as the second one (hereinafter called specific dissipation rate). He related ω to the length scale l as follows

$$\omega = c\frac{k^{\frac{1}{2}}}{l} \tag{6.1}$$

where c is a constant. The unit of measurement of ω is $[1/t]$, where t is the time. The reciprocal of ω is the time scale on which dissipation of turbulence kinetic energy occurs. Wilcox [71] underlined that, while the actual processes of dissipation (ε) take place in the smallest eddies, the specific dissipation rate (ω) is the transfer rate of turbulence kinetic energy to the smallest eddies. Consequently, ω is indirectly associated with dissipative processes.

The relation between ω and ε is

$$\omega = \frac{\varepsilon}{C_\mu k} \tag{6.2}$$

where C_μ is a constant. Kolmogorov understood that there is a fairly small number of physical processes observed in the fluid motion: unsteadiness, convection, diffusion, dissipation, dispersion and production.

In the last decades, many authors proposed several $k-\omega$ turbulence models applied to the compressible flow around a airfoil [59, 70, 71]. These models are more computationally robust than the $k-\varepsilon$ models for the integration of the turbulent flows to a solid boundary. As underlined by several authors [49, 71], the first and more used Wilcox model [70] has the tendency to overestimate the eddy viscosity when the production of turbulent kinetic energy exceeds its dissipation. The new version of the $k-\omega$ turbulence model proposed by Wilcox [71] is the most famous model and limits the growth of the turbulent kinetic energy and the eddy viscosity. The Cartesian equations for the model [71] are

$$\frac{\partial k}{\partial t} + \frac{\partial u_j k}{\partial x_j} = \tau_{ij}\frac{\partial u_i}{\partial x_j} - \beta^* k\omega + \frac{\partial}{\partial x_j}\left[\left(\nu + \sigma^*\nu_T\right)\frac{\partial k}{\partial x_j}\right] \tag{6.3}$$

$$\frac{\partial \omega}{\partial t} + \frac{\partial u_j \omega}{\partial x_j} = \frac{\alpha}{\nu_T}\tau_{ij}\frac{\partial u_i}{\partial x_j} - \beta\omega^2 + \frac{\sigma_d}{\omega}\frac{\partial k}{\partial x_j}\frac{\partial \omega}{\partial x_j} + \frac{\partial}{\partial x_j}\left[\left(\nu + \sigma\nu_T\right)\frac{\partial \omega}{\partial x_j}\right] \tag{6.4}$$

All the closure coefficients and the auxiliary relations are given by

$$\begin{gathered}
\alpha = \frac{13}{25} \quad \beta = 0.0708 \quad \beta^* = 0.09 \quad \sigma = \frac{1}{2} \quad \sigma^* = \frac{3}{5} \quad \sigma_{d0} = \frac{1}{8} \\
\sigma_d = \begin{cases} 0 & \frac{\partial k}{\partial x_j}\frac{\partial \omega}{\partial x_j} \leq 0 \\ \sigma_{d0} & \frac{\partial k}{\partial x_j}\frac{\partial \omega}{\partial x_j} > 0 \end{cases} \\
\nu_T = \frac{k}{\tilde{\omega}} \quad \tilde{\omega} = max\left\{\omega, \quad C_{lim}\sqrt{\frac{2S_{ij}S_{ij}}{\beta^*}}\right\} \quad C_{lim} = \frac{7}{8}
\end{gathered} \tag{6.5}$$

In Eqs. 6.3-6.4, τ_{ij} and S_{ij} are, respectively, the Cartesian components of the turbulent stress tensor and strain rate tensor. $\tau_{ij}\frac{\partial u_i}{\partial x_j}$ and $\frac{\alpha}{\nu_T}\tau_{ij}\frac{\partial u_i}{\partial x_j}$ are the production terms; $\beta^* k\omega$ and $\beta\omega^2$ are the dissipation terms; $\frac{\sigma_d}{\omega}\frac{\partial k}{\partial x_j}\frac{\partial \omega}{\partial x_j}$ is the cross diffusion term and $\frac{\partial}{\partial x_j}\left[\left(\nu + \sigma^*\nu_T\right)\frac{\partial k}{\partial x_j}\right]$ and $\frac{\partial}{\partial x_j}\left[\left(\nu + \sigma\nu_T\right)\frac{\partial \omega}{\partial x_j}\right]$ are the diffusive terms. It is possible obtain the ω-equation from the ε-equation; all mathematical

steps are described in Appendix C.

6.1.1 Cross diffusion term

The cross-diffusion term appears in the Eq. 6.4, because this equation derives form the ε equation (all mathematical steps are described in Appendix C). This term is originally introduced by Speziale [59]. According to [59], the cross diffusion term can make the $k-\omega$ asymptotically consistent near the wall. In free shear flows, this term enhances the production of ω that increases the turbulent kinetic energy dissipation. The overall effect is to reduce the net production of turbulence kinetic energy.

Menter [49] introduced a coefficient, σ_d, for activating the cross-diffusion term only away from the solid boundary: this coefficient (Eq. 6.5) becomes zero near the solid boundary, where k grows and ω decreases, as the distance from the boundary increases.

6.1.2 Stress-limiter

Menter [49] and Wilcox [71] demonstrated that the first Wilcox model [70] has the tendency to predict turbulence levels that are much higher than the measured ones. For this reason, the eddy viscosity is limited by the introduction of a stress limiter, $\tilde{\omega}$ (Eq. 6.5).

In the context of the simulation of wave and velocity fields, Mayer and Madsen [48] have demonstrated that Wilcox's $k-\omega$ produces too much turbulence in the zone between the oscillating turbulent boundary layer and the wave breaking fronts. For this reason, the Reynolds stress tensor is overestimated. The effects of the overestimation of the turbulent stress tensor cause premature wave decay: the wave breaking point is not correctly evaluated and the wave height is underestimated around the wave breaking point.

In order to improve the representation of the turbulent phenomena under breaking waves and the simulation of the wave-structure interactions, in this thesis, a new $k-\omega$ turbulence model is proposed.

6.2 New $k-\omega$ Turbulence Model

In this subsection, a new $k-\omega$ turbulence model is proposed for the simulation of the breaking waves and wave-structure interactions. This new model is collocated in the context of URANS numerical simulations, where only the unsteady stochastic turbulent fluctuations are represented by the Reynolds stress tensor. The unsteady quasi-periodic vortex structures are directly simulated in the velocity fields.

As demonstrated by [48], the Wilcox's $k-\omega$ turbulence model, when applied to breaking wave simulations, produces an excess of turbulent kinetic energy in the zone between the oscillating wave boundary and the wave fronts, with a resulting underestimation of the wave height both in the shoaling and surf zone and a wrong prediction of the wave breaking point. In the new model, the excessive growth of the turbulent kinetic energy is limited by using a particular closure relation for the eddy viscosity and for the dissipation of ω.

The balance equations for the turbulent kinetic energy and for the specific dissipation rate are written in an original integral contravariant form on a generalized curvilinear coordinate system.

$$\begin{aligned}\frac{\partial \overline{Hk}}{\partial \tau} = &-\frac{1}{\Delta V_0\sqrt{g_0}}\sum_{\alpha=1}^{3}\left\{\int_{\Delta A_0^{\alpha+}}\left[Hk\left(\frac{Hu^\alpha}{H}-\frac{Hw_g^\alpha}{H}\right)\right]\sqrt{g_0}d\xi^\beta d\xi^\gamma - \right.\\ &\left.\int_{\Delta A_0^{\alpha-}}\left[Hk\left(\frac{Hu^\alpha}{H}-\frac{Hw_g^\alpha}{H}\right)\right]\sqrt{g_0}d\xi^\beta d\xi^\gamma\right\}\\ &+\frac{1}{\Delta V_0\sqrt{g_0}}\sum_{\alpha=1}^{3}\left\{\int_{\Delta A_0^{\alpha+}}\left[\left(\nu+\frac{\nu_T}{\sigma_k}\right)g^{\alpha r}\frac{\partial k}{\partial \xi^r}H\sqrt{g_0}\right]d\xi^\beta d\xi^\gamma - \right.\\ &\left.\int_{\Delta A_0^{\alpha-}}\left[\left(\nu+\frac{\nu_T}{\sigma_k}\right)g^{\alpha r}\frac{\partial k}{\partial \xi^r}H\sqrt{g_0}\right]d\xi^\beta d\xi^\gamma\right\}\\ &+\frac{1}{\Delta V_0\sqrt{g_0}}\int_{\Delta V_0}\left[(P_k-\beta^* k\omega)H\sqrt{g_0}\right]d\xi^1 d\xi^2 d\xi^3\end{aligned} \tag{6.6}$$

$$\begin{aligned}\frac{\partial\overline{H\omega}}{\partial\tau} = &-\frac{1}{\Delta V_0\sqrt{g_0}}\sum_{\alpha=1}^{3}\left\{\int_{\Delta A_0^{\alpha+}}\left[H\omega\left(\frac{Hu^\alpha}{H}-\frac{Hw_g^\alpha}{H}\right)\right]\sqrt{g_0}d\xi^\beta d\xi^\gamma - \right.\\ &\left.\int_{\Delta A_0^{\alpha-}}\left[H\omega\left(\frac{Hu^\alpha}{H}-\frac{Hw_g^\alpha}{H}\right)\right]\sqrt{g_0}d\xi^\beta d\xi^\gamma\right\}\\ &+\frac{1}{\Delta V_0\sqrt{g_0}}\sum_{\alpha=1}^{3}\left\{\int_{\Delta A_0^{\alpha+}}\left[\left(\nu+\frac{\nu_T}{\sigma_\omega}\right)g^{\alpha r}\frac{\partial\omega}{\partial\xi^r}H\sqrt{g_0}\right]d\xi^\beta d\xi^\gamma - \right.\\ &\left.\int_{\Delta A_0^{\alpha-}}\left[\left(\nu+\frac{\nu_T}{\sigma_\omega}\right)g^{\alpha r}\frac{\partial\omega}{\partial\xi^r}H\sqrt{g_0}\right]d\xi^\beta d\xi^\gamma\right\}\\ &+\frac{1}{\Delta V_0\sqrt{g_0}}\int_{\Delta V_0}\left[\left(\frac{\alpha_\omega}{\nu_T}P_k-\beta_\omega\omega^2\right)H\sqrt{g_0}\right]d\xi^1d\xi^2d\xi^3\\ &+\frac{1}{\Delta V_0\sqrt{g_0}}\int_{\Delta V_0}\frac{\sigma_{\omega'}}{\omega}\left[\frac{\partial k}{\partial\xi^r}\vec{g}^{(r)}\frac{\partial\omega}{\partial\xi^r}\vec{g}^{(r)}\right]H\sqrt{g_0}d\xi^1d\xi^2d\xi^3\end{aligned} \tag{6.7}$$

Analogously to k-equation, the terms of Eq. 6.7 can be defined as follow:

- Unsteady term: it is the first term on the left-hand side of Eq. 6.7.
- Advection: it is identified by the first and second terms on the right-hand side of Eq. 6.7.
- Molecular and turbulent diffusion: they are expressed by the third and fourth terms on the right-hand side of Eq. 6.7.
- Production and dissipation: these terms are the fifth terms in Eq. 6.7.
- Cross diffusion term: it is the last term on the right-hand side of Eq. 6.7. The meaning of this term is explained in Section 6.1.1.

The production of ω and k are given by Eq. 5.2 and Eq. 5.4. In Eqs. 6.6 and 6.7, the closure coefficients are the ones given by Wilcox [71]

$$\begin{gathered}\alpha_\omega=\frac{13}{25}\quad\beta^*\equiv C_\mu=0.09\quad\sigma_k=\frac{3}{5}\quad\sigma_\omega=\frac{1}{2}\quad\sigma_{\omega'0}=\frac{1}{8}\\ \sigma_{\omega'}=\begin{cases}0 & \frac{\partial k}{\partial\xi^r}\vec{g}^{(r)}\frac{\partial\omega}{\partial\xi^r}\vec{g}^{(r)}\le 0\\ \sigma_{\omega'0} & \frac{\partial k}{\partial\xi^r}\vec{g}^{(r)}\frac{\partial\omega}{\partial\xi^r}\vec{g}^{(r)}>0\end{cases}\end{gathered} \tag{6.8}$$

In Eq. 6.7, the term multiplied by $\sigma_{\omega'}$ (cross diffusion term) enhances the production of the specific dissipation rate, as explained in Section 6.1.1; the derivation of the cross diffusion term from the ε equation is explained in Appendix C. The

coefficient $\sigma_{\omega'}$, introduced for the first time by Menter [49], activates the additional production term away from the solid boundary. As known, the production of turbulent kinetic energy is mainly located in the oscillating wave boundary layer outside the surf zone, while in the surf zone this production is located both in the oscillating wave boundary layer and on the breaking wave fronts. Near the wall, the cross diffusion term is zero, because k increases while ω decreases. Away from the wall, the cross diffusion term differs from zero, ω increases and, consequently, k decreases.

Some authors [48, 49, 71] demonstrated that the Wilcox model [70] overestimates the production of turbulent kinetic energy. For this reason, some years later Wilcox [71] proposed a new model in which the eddy viscosity is limited by the introduction of a stress limiter. Following this approach, in this thesis an *ad hoc* stress-limiter for the breaking waves is introduced in the eddy viscosity.

$$\begin{gathered} \nu_T = \frac{k}{\tilde{\omega}} \\ \tilde{\omega} = max\left(\tilde{\tilde{\omega}}, C_{\omega 2}\frac{\beta}{\beta^*\alpha}\frac{2S^{lm}S^{lm}}{2\Omega^{lm}\Omega^{lm}}\omega\right) \quad C_{\omega 2} = 0.05 \\ \tilde{\tilde{\omega}} = max\left(\omega, \quad C_\omega\sqrt{\frac{2S^{lm}S^{lm}}{\beta^*}}\right) \end{gathered} \tag{6.9}$$

In Eq. 6.9, Ω^{lm} is the contravariant components of the vorticity tensor. The coefficient C_ω is a function of the ratio between the maximum total water depth at the breaking point and the local maximum water depth. This coefficient varies in the range $[1.0 - 2.0]$.

$$C_\omega = \frac{max(H_{max})}{H_{max}} \tag{6.10}$$

Before the wave breaking point, the value of C_ω is set to 1.0; after the wave breaking point, C_ω increases, because the maximum water depth decreases approaching the shoreline. This coefficient is able to take into account the differences in the production of ω before and after the wave breaking point. $\tilde{\omega}$ is the maximum value between $\tilde{\tilde{\omega}}$ and a specific term that is a function of the strain rate tensor and the vorticity tensor. Where the strain rate tensor has high values, the vorticity tensor has lower values and the ratio on the second term in the definition of $\tilde{\omega}$ increases. By means of $\tilde{\omega}$ and $\tilde{\tilde{\omega}}$, the eddy viscosity is limited in the zones where too small

values of ω would erroneously increase its values.

The coefficient β_ω in the dissipation term of ω is defined by following the suggestion proposed by Yakhot [72], as follow

$$\beta_\omega = \beta_{\omega 1} + C_\mu (2\zeta)^2 \frac{1-(2\zeta)}{1+0.3(2\zeta)^2} \qquad \zeta = \frac{1}{\omega}\sqrt{2S^{lm}S^{lm}} \tag{6.11}$$

in which $\beta_{\omega 1} = 0.1$. β_ω is dynamically defined by the strain rate tensor. Its variation is shown in Fig. 6.1. For high values of the magnitude of the strain rate tensor, the coefficient β_ω decreases and, consequently, the dissipation of ω reduces. By this way, the specific dissipation rate increases and the turbulent kinetic energy is further reduced.

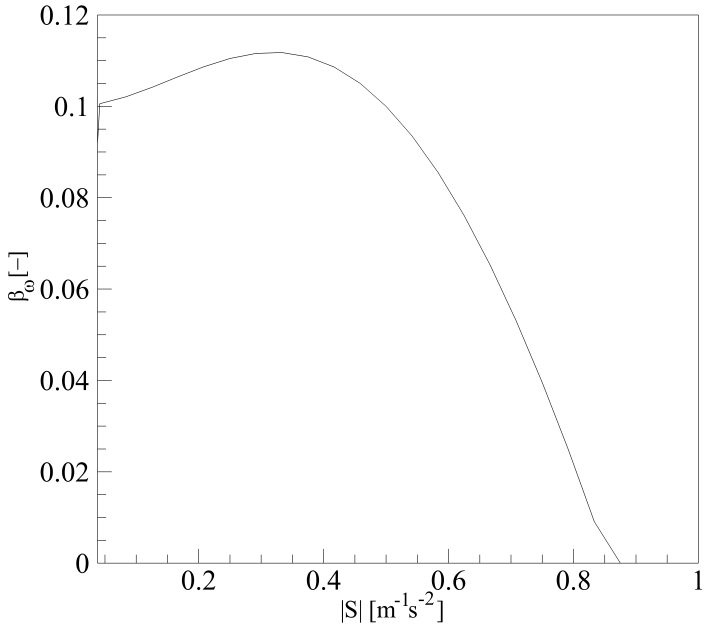

Figure 6.1: Variation of β_ω as a function of the absolute value of the strain rate tensor $|S|$.

6.2.1 Boundary Conditions

The boundary conditions for ω and k is placed directly at the bottom ($z = 0m$).

Wilcox [71] have proposed a boundary condition for ω on the wall as a function of the bottom roughness S_c and the friction velocity u^*. By following his

suggestions, in this thesis the boundary condition for ω is defined as follow

$$\omega_B = \frac{u^{*2}}{\nu} B_C \qquad B_C = \begin{cases} \left(\frac{100}{Sc^+}\right)^2 & S_c^+ \leq 5 \\ \frac{50}{S_c^+} + \left[\left(\frac{100}{S_c^+}\right)^2 - \frac{50}{S_c^+}\right] e^{5-S_c^+} & S_c^+ > 5 \end{cases} \tag{6.12}$$

where $S_c = \frac{S_c u^*}{\nu}$. The boundary condition for the turbulence kinetic energy is set zero at the bottom.

The friction velocity u^* is calculated as follow

$$\begin{aligned} u^* &= \sqrt{u_x^{*2} + u_y^{*2}} \\ u_x^* &= \sqrt{\nu \frac{\partial u}{\partial z}} \\ u_y^* &= \sqrt{\nu \frac{\partial v}{\partial z}} \end{aligned} \tag{6.13}$$

where u and v are horizontal Cartesian velocity components, x and y are the horizontal coordinates and z is the vertical one.

The velocity boundary conditions, u_B and v_B, are placed at the border between the viscous sublayer and the buffer layer; they are calculated as a linear function between the null velocity at the bottom (at $z = 0m$) and the velocity calculated in the first calculation grid cell, in the buffer layer.

6.3 Results and discussion

In this Section, the three experimental test cases, previously presented, are numerically reproduced with the new $k - \omega$ turbulence model. In these numerical simulations, the adopted numerical scheme is the new high-order shock-capturing.

The new $k - \omega$ turbulence model allows to assign directly at the bottom the boundary condition for the specific dissipation rate. Consequently, through this model it is possible to adequately take into account the turbulent phenomena that occur in the oscillating wave boundary layer.

The adopted vertical discretization of the grid cells near the bottom in the oscillating wave boundary layer is shown in Fig. 6.2. In this configuration, there are three grid cells in the buffer layer and four grid cells in the turbulent core.

The bottom boundary conditions for k and ω are placed directly at the bottom,

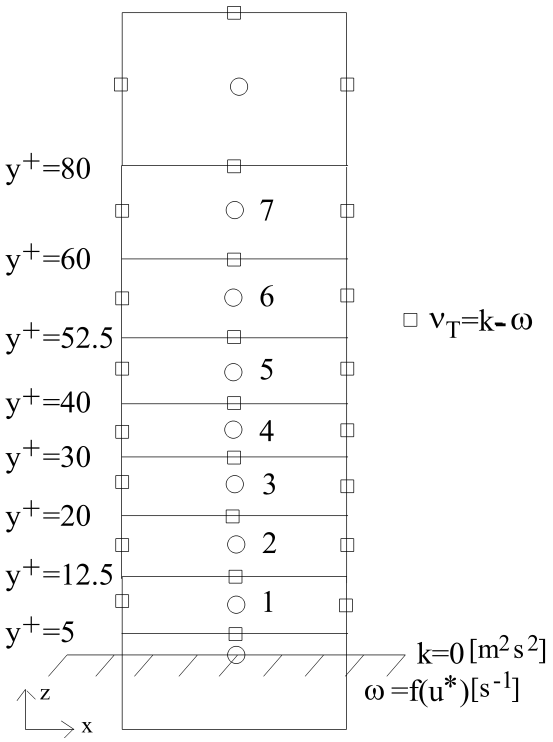

Figure 6.2: Vertical discretization of the grid cells inside the buffer layer and turbulent core for the new $k-\omega$ turbulence model.

$z = 0m$: k is imposed equal to zero; ω is given by Eq. 6.12; the bottom roughness is $Sc = 0.0005m$.

The equations of motion are solved starting from the center of the first calculation grid cell (indicated by number one in Fig. 6.2) that is placed in the buffer layer ($y^+ \simeq 9$). The turbulent equations for k and ω are solved starting from the lower face of the first calculation grid cell, at the border between the viscous sublayer and the buffer layer ($y^+ = 5$).

All the numerical simulations are carried out by a spatial discretization step $\Delta x = 0.05m$ in the wave propagation direction and 22 non uniform layer along the vertical direction.

In Tab. 6.1, a synthetic description of the test cases of this chapter are described.

6.3.1 Ting and Kirby test case of a spilling breaker with a cnoidal wave

A Ting and Kirby's test case [63] for a spilling breaker is numerically reproduced. In Figs. 6.3, 6.4 and 6.5, the numerical results obtained by the new $k-\omega$ turbu-

Test	Name	Turb. model	Numerical Scheme
Ting and Kirby [63]	Ting6	new $k-\omega$	5nd-order (WTENO + Exact Riemann S.)
Stive spilling [60, 61]	Stive4	new $k-\omega$	5nd-order (WTENO + Exact Riemann S.)
Stive spilling-plunging [61]	Stivesp4	new $k-\omega$	5nd-order (WTENO + Exact Riemann S.)

Table 6.1: Test cases with the new $k-\omega$ turbulence model.

lence model are shown.

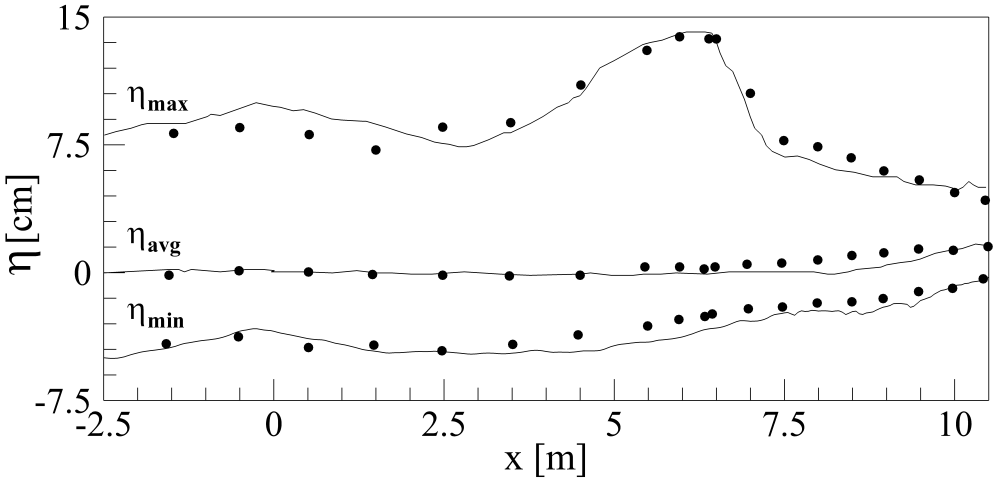

Figure 6.3: Ting6: local minimum, average and maximum water surface elevations. Experimental measurements • [63] and numerical results − with the new $k-\omega$ turbulence model.

The numerical results in terms of the local minimum, maximum and average water surface elevations fit very well the experimental measurements, as shown in Fig. 6.3. The wave breaking point is correctly located, the local maximum water surface elevation at the breaking point and in the surf zone are correctly evaluated.

The time mean vertical distribution of the normalized turbulent kinetic energy, showed in Figs. 6.4(a)-(d), is in good agreement with the experimental measurements, while at $x = 9.67m$ (Figs. 6.4(e)) is slightly overestimated. Concerning the time mean vertical distribution of normalized turbulent kinetic energy (Figs. 6.4), it is possible to make the following considerations in comparison with the same quantity obtained with the new $k-l$ turbulence model (Figs. 5.8). The time mean vertical distribution of the normalized turbulent kinetic energy obtained by the new $k-l$ turbulence model is in good agreement at $x = 7.27m$ (Figs. 5.8(a)),

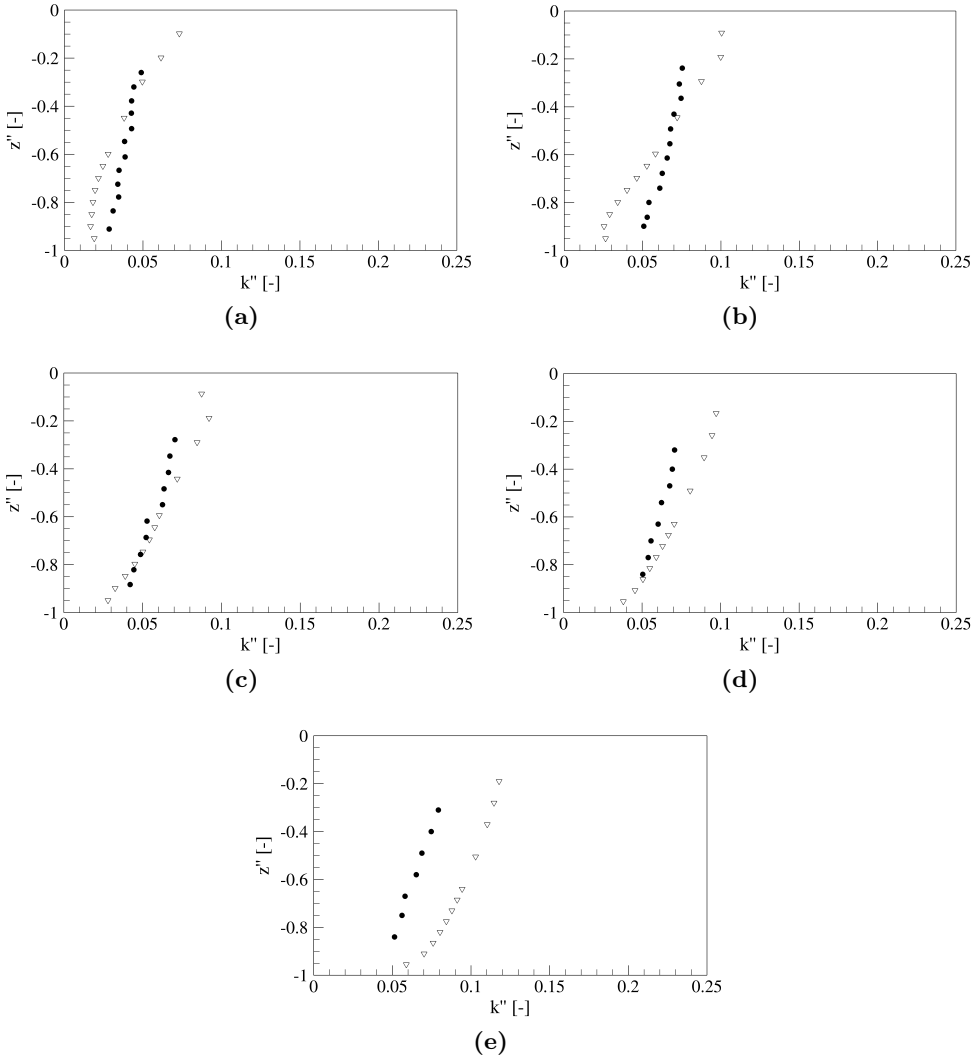

Figure 6.4: Ting6: time mean vertical distribution of the normalized turbulent kinetic energy at (a) $x = 7.27m$, (b) $x = 7.88m$, (c) $x = 8.5m$, (d) $x = 9.07m$ and (e) $x = 9.67m$. Experimental measurements • [63] and numerical results ▽ with the new $k-\omega$ turbulence model.

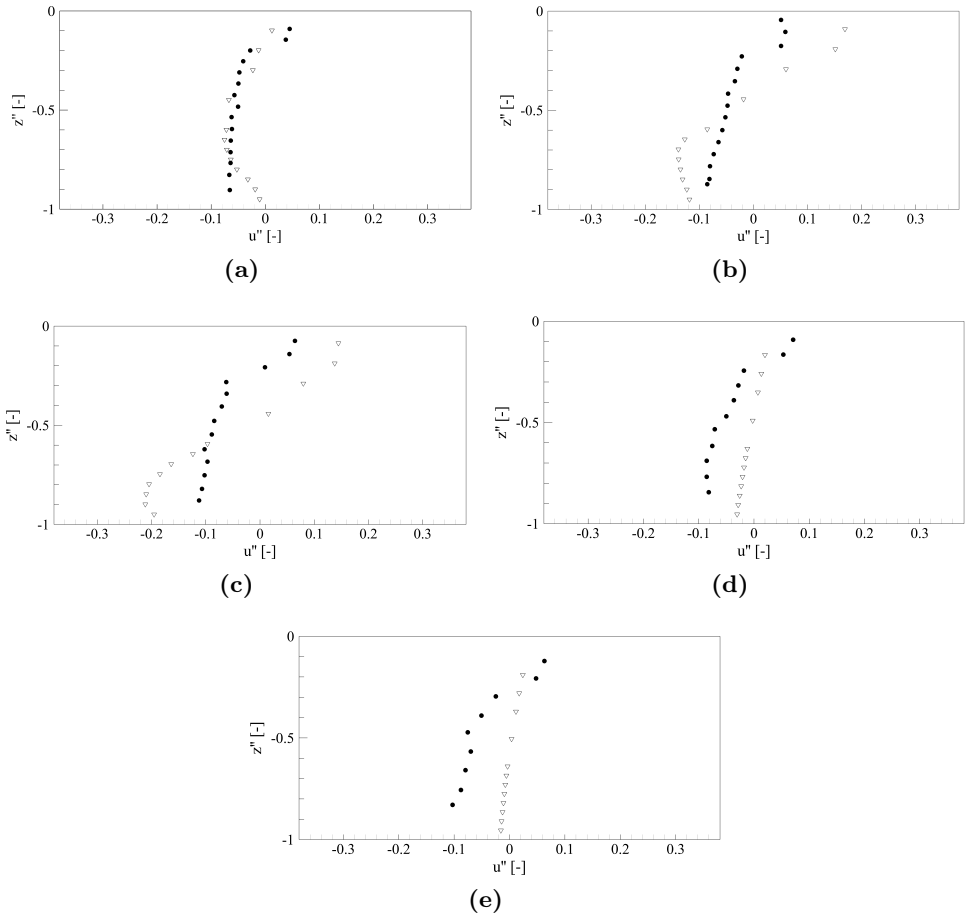

Figure 6.5: Ting6: time mean vertical distribution of the normalized horizontal flow velocity (undertow) at (a) $x = 7.27m$, (b) $x = 7.88m$, (c) $x = 8.5m$, (d) $x = 9.07m$ and (e) $x = 9.67m$. Experimental measurements • [63] and numerical results ▽ with the new $k - \omega$ turbulence model.

slightly overestimated at $x = 7.88m$ (Figs. 5.8(b)), overestimated at $x = 8.50m$ (Fig. 5.8(c)) and underestimated at $x = 9.07m$ and $x = 9.67m$ (Figs. 5.8(d) and (e)). In general, the new $k - \omega$ model is able to better evaluate the distribution of the turbulent kinetic energy in all the surf zone.

The time mean vertical distribution of the normalized horizontal flow velocity, showed in Figs. 6.5(a)-(c), is in good agreement with the experimental measurements, while is slightly underestimated at $x = 9.07m$ and $x = 9.67m$ (Figs. 6.5(d)-(e)). By comparing the numerical results obtained by the new $k - l$ turbulence model, Figs. 5.9, with the ones obtained by the new $k - \omega$ turbulence model Figs. 6.5 in terms of time mean vertical distribution of the normalized horizontal flow velocity, it is possible to notice that the new $k - \omega$ turbulence model gives better agreement with the experimental measurements than the results obtained

by the new $k - l$ turbulence model.

In Figs. 6.6 (a)-(f) are represented respectively five instantaneous fields of turbulent kinetic energy and an instantaneous velocity field, in which one vector every two is drawn. These snapshots are taken after 80 subsequent waves, when the results reach a quasi-steady state ($T_s = 160s$).

As can be seen from Figs. 6.6(a)-(e), most of the turbulent kinetic energy can be found close to the wave breaking fronts and, in minor measure, under the wave toughs, between two subsequent breaking wave fronts. In fact, after the wave breaking point, ($x > 6.40m$) the maximum production of turbulent kinetic energy takes place on the wave breaking front and, in minor measure, inside the oscillating wave boundary layer; the produced turbulent kinetic energy is partly diffused and transported towards the middle part of the water column, between two subsequent breaking wave fronts. In this region, where the production of turbulence is small, the turbulent kinetic energy tends to decrease, until another new breaking wave front and oscillating boundary layer produce new turbulent kinetic energy and a new transport of turbulence towards the middle part of the water column takes place. As can be noticed by the sequence in Figs. 6.6(a)-(e), these phenomena are accompanied by a reduction of the wave height in the surf zone.

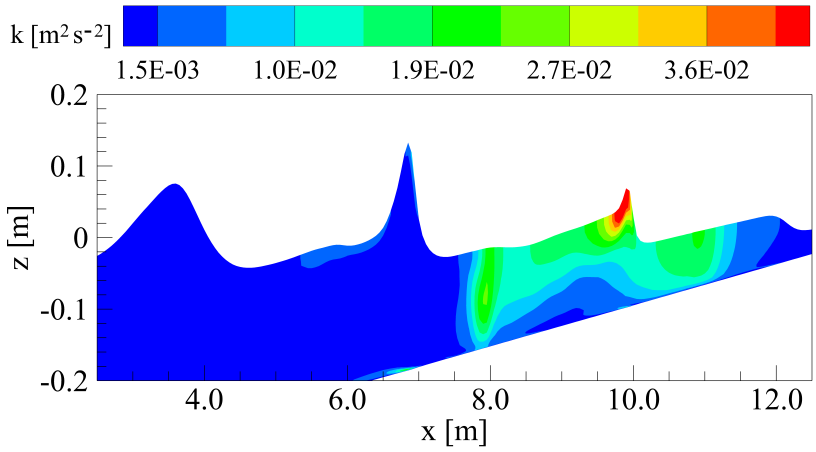

(a)

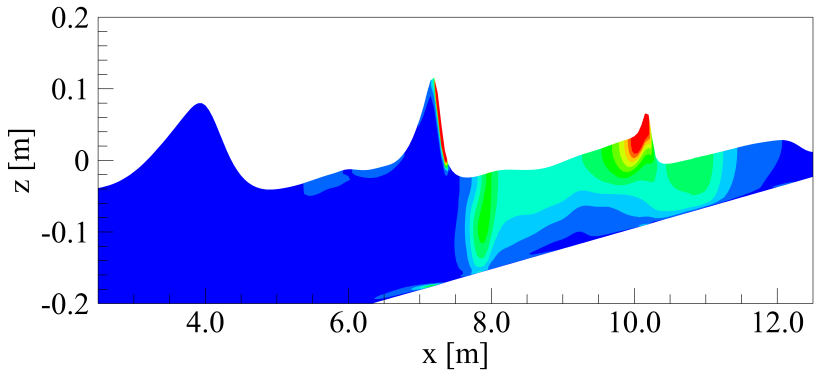
0.2
0.1
0
-0.1
-0.2
z [m]
4.0
6.0
8.0
10.0
12.0
x [m]

(b)

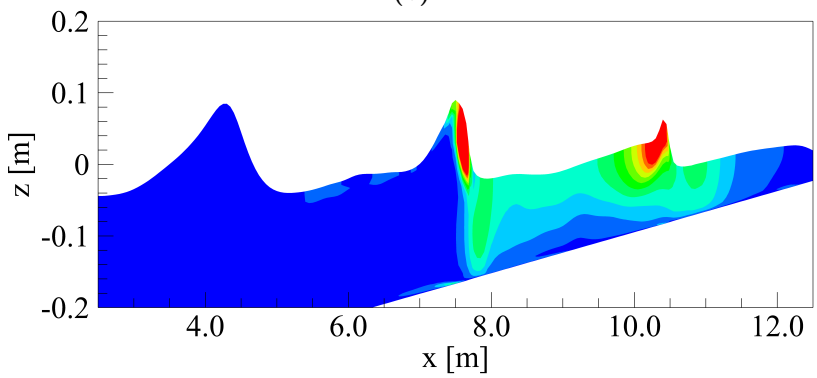
0.2
0.1
0
-0.1
-0.2
z [m]
4.0
6.0
8.0
10.0
12.0
x [m]

(c)

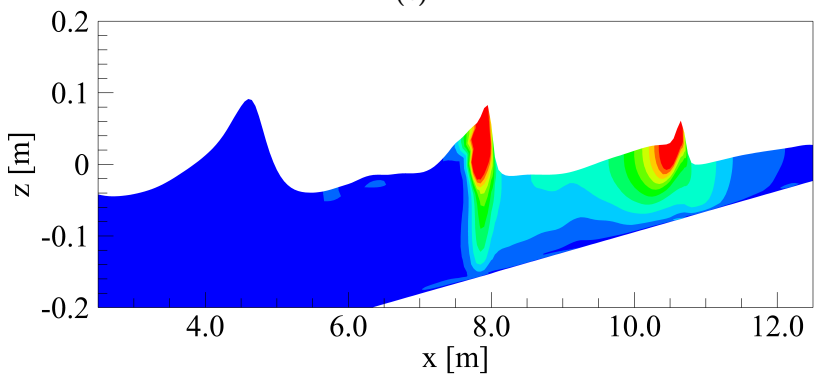
0.2
0.1
0
-0.1
-0.2
z [m]
4.0
6.0
8.0
10.0
12.0
x [m]

(d)

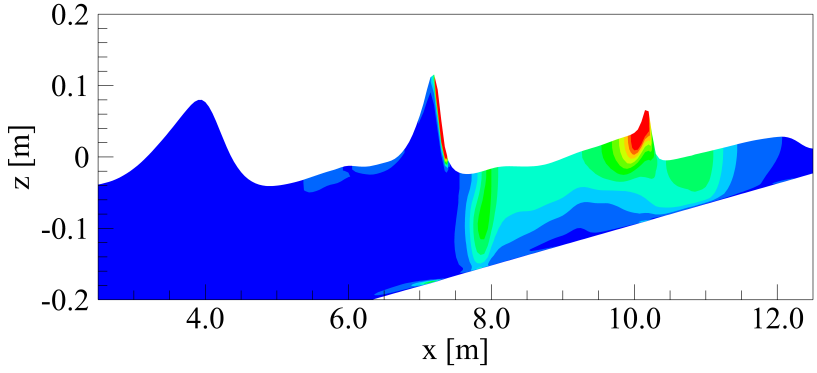
0.2
0.1
0
-0.1
-0.2
z [m]
4.0
6.0
8.0
10.0
12.0
x [m]

(e)

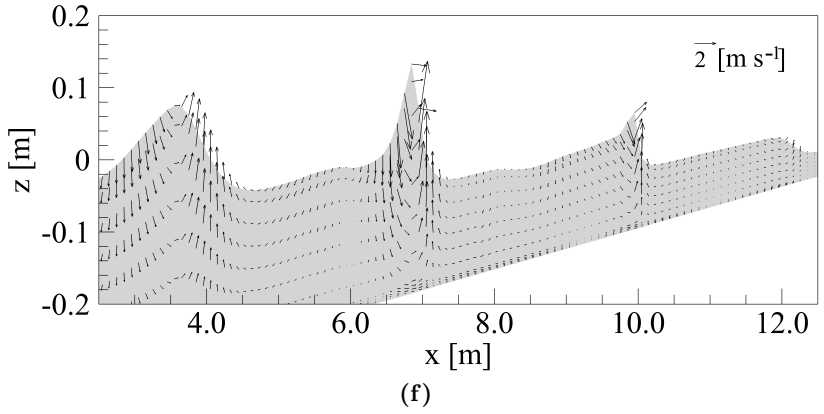

Figure 6.6: Ting6: Instantaneous fields with contours of turbulent kinetic energy at (a) $T_s = 160.2s$, (b) $T_s = 160.4s$, (c) $T_s = 160.6s$, (d) $T_s = 160.8s$, (e) $T_s = 161.0s$. (f) Instantaneous velocity field, one vectors every two is drawn ($T_s = 160.2s$).

6.3.2 Stive test case of a spilling breaker with a monochromatic wave

A Stive test case for a spilling breaker [60, 61] is numerically reproduced by using the new $k - \omega$ turbulence model and the high-order numerical scheme. In Fig. 6.7, the wave height is shown in comparison with the experimental measurements. From Fig. 6.7, it is possible to notice that the wave height is correctly evaluated before and after the wave breaking point. Also the wave breaking point is correctly evaluated.

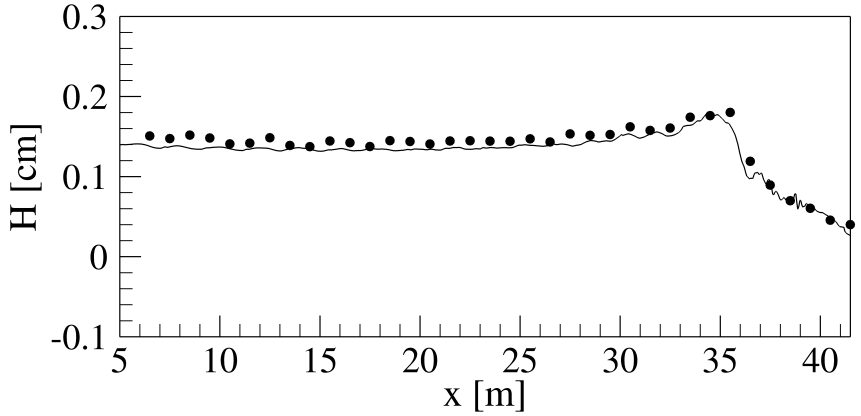

Figure 6.7: Stive4: wave height. Experimental measurements • [60, 61] and numerical results − with the new $k - \omega$ turbulence model.

In Figs. 6.8(a)-(f), five instantaneous fields of turbulent kinetic energy and an instantaneous velocity fields, in which one vector every two in shown, are represented. These wave and velocity fields are taken after about 100 subsequent waves, when the results reach quasi-steady state ($T_s = 180s$).

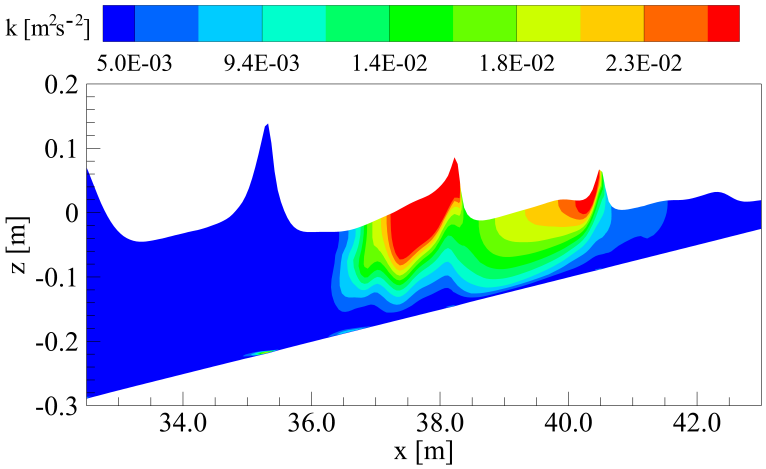
k [m²s⁻²]
5.0E-03
9.4E-03
1.4E-02
1.8E-02
2.3E-02
0.2
0.1
0
-0.1
-0.2
-0.3
z [m]
34.0
36.0
38.0
40.0
42.0
x [m]

(a)

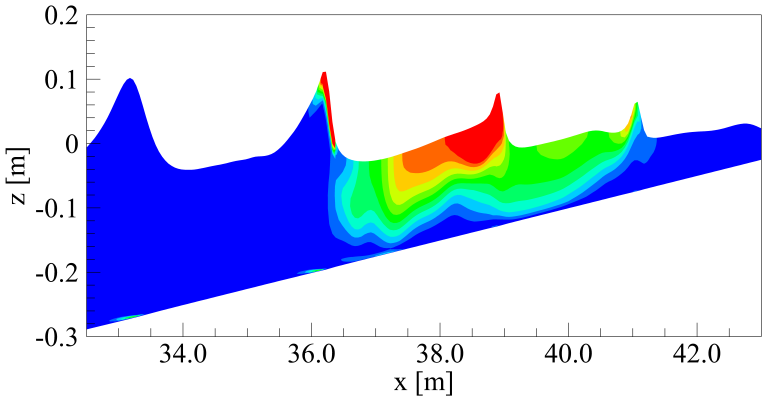
0.2
0.1
0
-0.1
-0.2
-0.3
z [m]
34.0
36.0
38.0
40.0
42.0
x [m]

(b)

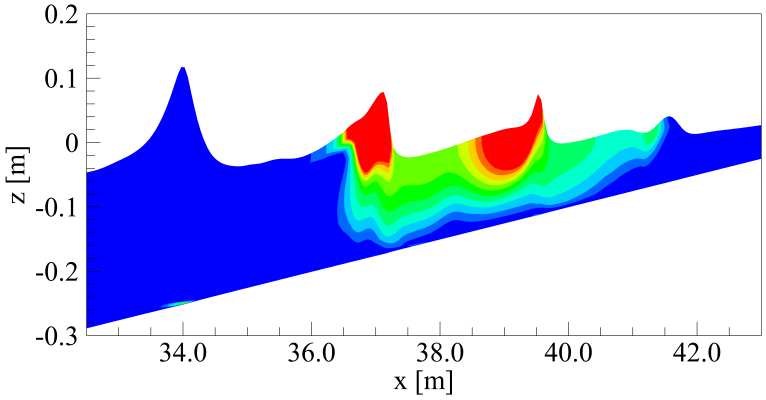
0.2
0.1
0
-0.1
-0.2
-0.3
z [m]
34.0
36.0
38.0
40.0
42.0
x [m]

(c)

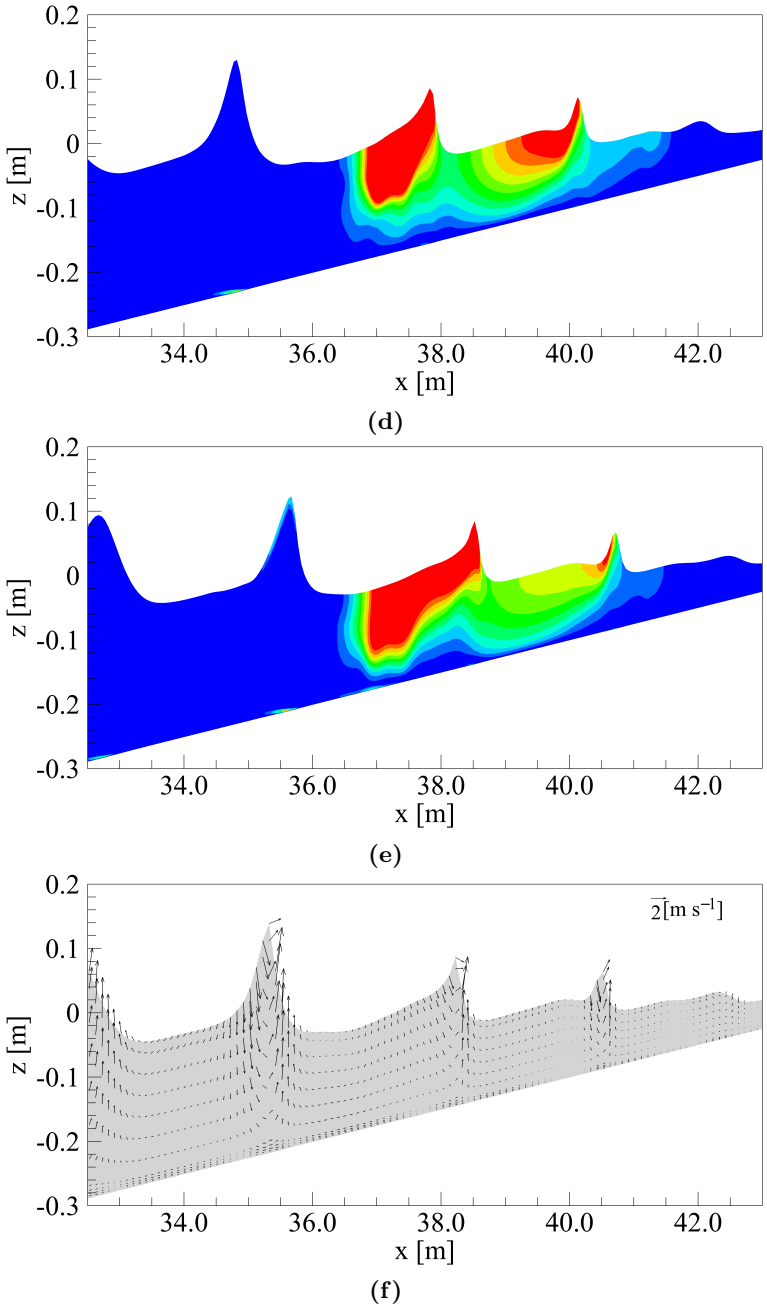

Figure 6.8: Stive4: Instantaneous fields with contours of turbulent kinetic energy at (a) $T_s = 180.0s$, (b) $T_s = 180.5s$, (c) $T_s = 181.0s$, (d) $T_s = 181.5s$ and (e) $T_s = 182.0s$. (f) Instantaneous velocity field, one vectors every two is drawn ($T_s = 180s$).

From Figs. 6.8(a)-(e), it is possible to notice that the maximum values of the turbulent kinetic energy is in the surf zone, in particular around the breaking wave crests and at the bottom. In the other part of the surf zone, the turbulent kinetic energy is not produced, but comes from the one produced on the wave breaking fronts.

6.3.3 Stive test case of a spilling-plunging breaker with a monochromatic wave

A Stive test case for a spilling-plunging breaker [61] is numerically reproduce with the new $k-\omega$ turbulence model and the high-order numerical scheme. In Fig. 6.9, the numerical results are compared with the experimental measurements in terms of wave height.

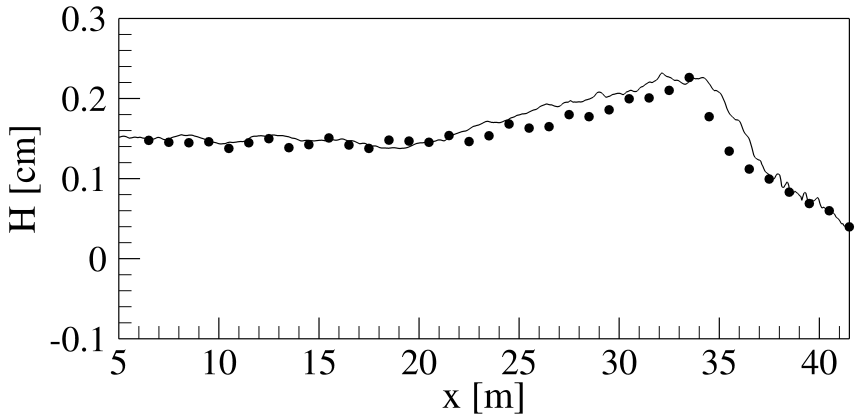

Figure 6.9: Stivesp4: wave height. Experimental measurements • [61] and numerical results − with the new $k-\omega$ turbulence model.

The wave height shown in Fig. 6.9 is quite in accordance with the experimental measurements; it is slightly overestimated after the wave breaking point. The wave height at the wave breaking point is correctly evaluated and also the position of the wave breaking point is correctly evaluated.

In the following figures (Figs. 6.10), six instantaneous fields are shown. In the first five figure, Figs. 6.10(a)-(e), the turbulent kinetic energy contour is represented and in the last figure, Fig. 6.10(f), the velocity field is shown. These fields are taken after about 60 subsequent waves, when the results reach quasi-steady state ($T_s = 179s$).

By looking at Figs. 6.10(a)-(e), it is possible to demonstrated that the waves

break around $x = 33.5m$ and it is possible to remark that, after this point, the maximum values of turbulent kinetic energy is mainly located on the wave breaking fronts. Before the wave breaking point, the production of turbulent kinetic energy is located at the bottom, in correspondence of the wave breaking fronts, as is known. The turbulent kinetic energy is transported and diffused towards the middle part of the water column.

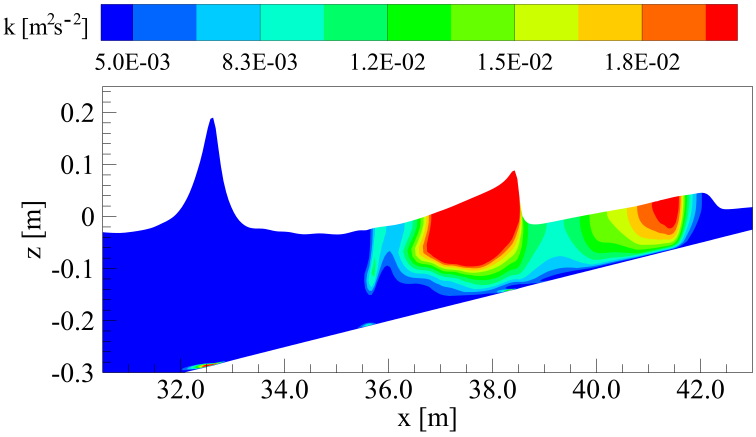

(a)

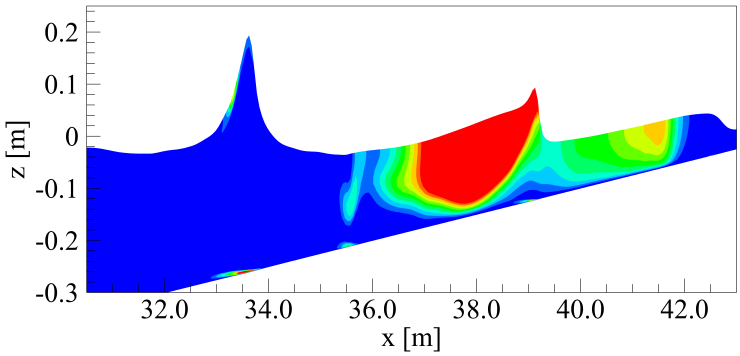

(b)

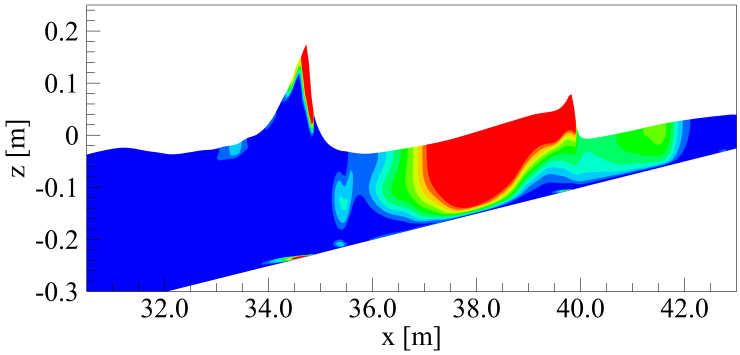

(c)

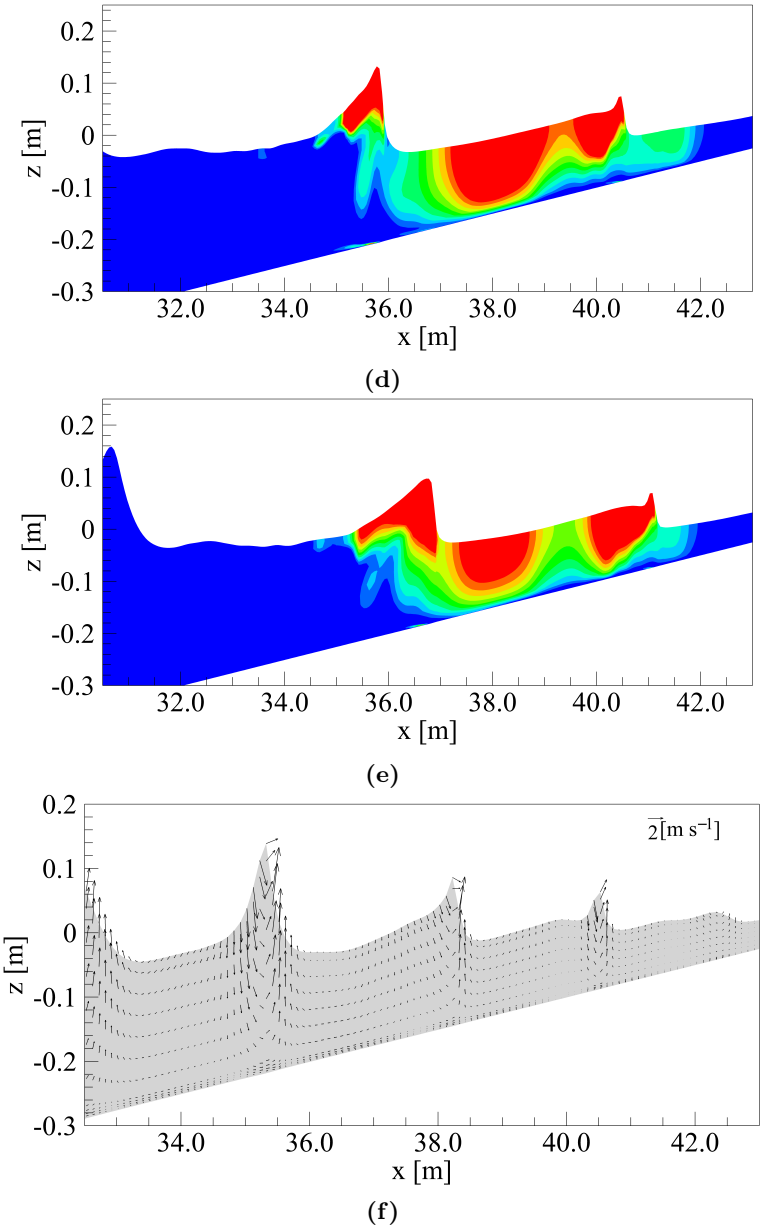

Figure 6.10: Stivesp4: Instantaneous fields with contours of turbulent kinetic energy at (a) $T_s = 179.0s$, (b) $T_s = 179.5s$, (c) $T_s = 180.0s$, (d) $T_s = 180.5s$ and (e) $T_s = 181.0s$. (f) Instantaneous velocity field, one vectors every two is drawn ($T_s = 179s$).

6.4 Conclusions

In this Chapter, the new $k-\omega$ turbulence model is proposed. Three test cases are numerically reproduced by the new $k-\omega$ turbulence model. In the new $k-\omega$ turbulence model, the calculation point nearest to the bottom, in which the equations of motion are solved, is in the buffer layer, in the proximity of the viscous sublayer ($y^+ \simeq 9$); the velocity boundary condition is placed at the border between the buffer layer and the viscous sublayer ($y^+ = 5$) and it is calculated as a function of the velocity of the first grid cell nearest to the bottom. The k-equation and ω-equation are solved starting from the border between the viscous sublayer and the buffer layer ($y^+ = 5$). The boundary condition for the turbulent kinetic energy is zero directly at the bottom. Also the boundary condition for the specific dissipation rate is placed directly at the bottom and it is a function of the friction velocity (that it is not a function of a logarithmic law) and the bottom roughness. The specific dissipation rate ω used in the eddy viscosity is calculated as a function of the maximum value of three different values of ω. The first value is calculated directly by solving the ω-equation. The second value is calculated as a function of the absolute value of the strain rate tensor and the absolute value of the vorticity tensor. Finally, the third value is calculated by the product between the absolute value of the strain rate tensor and a coefficient that is activated as a function of the zone in which it is calculated. This coefficient is determined by the local maximum water depth and is increased in the surf zone, where the local maximum water depth is reduced. In such a way, the behaviour of the model before and after the wave breaking point is differentiated. In the new $k-\omega$ turbulence model, a dynamic coefficient for the dissipation of ω is also introduced to limit the production of the turbulent kinetic energy.

By using the new $k-\omega$ turbulence model, it has been possible to overcome the limits of the $k-l$ turbulence models, such as the hypothesis of the balance between production and dissipation of turbulent kinetic energy in all the turbulent core. Furthermore, the two-equation turbulence models provide not only for solving the k-equation, but also for the dissipation of k. Consequently, these models are complete, i.e., can be used to predict properties of a given turbulent flow with no prior knowledge of the turbulence structures.

The new formulation for the eddy viscosity limits the production of turbulent kinetic energy in the zone between the wave breaking fronts and the oscillating wave boundary layer, the excessive reduction of the wave height and an anticipation of the wave breaking point, as it happens in the standard $k - \omega$ turbulence model.

From the comparison between the experimental measurements and numerical results obtained by the new $k - \omega$ turbulence model and by the new high-order shock-capturing numerical scheme, it is possible to notice that this new model is able to correctly evaluate the wave height in the shoaling zone, the wave breaking point and the wave height in the surf zone. From the numerical results, it is also clear that the new $k - \omega$ turbulence model is able to correctly evaluate the time mean vertical distribution of the turbulent kinetic energy and the horizontal flow velocity. The fitting between the numerical and experimental results has demonstrated the need to solve the equations of motion inside the buffer layer and the k and ω equations starting from the border between the buffer layer and the viscous sublayer, in order to take into account the turbulence phenomena and their effects in oscillating wave boundary layer.

Chapter 7

Interaction between breaking waves and a coastal defence work

Emerged barrier are widely used coastal defense structures. Generally, they are heavy structures resting on the bottom which emerge from the free surface to avoid wave propagation. In most cases, they are placed parallel to the shoreline, isolated or in series. The presence of such barriers, besides modifying the wave fields and coastal currents, can cause local sea bottom erosion produced by unsteady quasi-periodic vortex structures close to the edge of the barrier. The flow velocity field that causes this local sea bottom erosion is fully three-dimensional and is related to the formation of vortexes of various dimensions which interact with each other. In this chapter, the new $k-\omega$ turbulence model is applied to the numerical simulation of the complex free-surface elevation and three-dimensional flow velocity fields produced by the interaction between breaking waves and an emerged vertical coastal barrier, which is placed parallel to the shoreline in the surf zone.

The fluid motion can be called turbulent when large Reynolds number is reached. In this case, the fluid laminar motion becomes unstable, inherently three-dimensional and unsteady and velocity and pressure fluctuations appear. In many cases of engineering interest flows are turbulent: flows past vehicles or objects, river and sea currents, etc. Hinze [29] defined the turbulence as follow: *Turbulent fluid motion is an irregular condition of flow in which the various quantities show a random variation with time and space coordinates, so that statistically distinct*

average values can be discerned.

Some authors described the turbulent fluid motion in terms of turbulent eddies that give rise to a vigorous mixing and effective turbulent stresses. The scale of turbulence ranges from large eddies to small eddies. The kinetic energy transfer (turbulence decay) takes place from large eddies to small eddies, this phenomena is called energy cascade [38–40]. The smallest eddies are dissipated into heat by the action of the molecular viscosity. The largest eddies are responsible for enhancing diffusivity.

As well explained by Wilcox [71], the main physical process that spreads the fluid motion over a wide range of wavelenghts is vortex stretching. The turbulence gains energy, if the vortex elements are primarily oriented in a direction in which the mean velocity gradients can stretch them. Consequently, the larger-scale turbulent motion carries most of the energy and is mainly responsible for the enhanced diffusivity and increasing stresses. In turn, the larger eddies randomly stretch the vortex elements that comprise the smaller eddies, cascading energy to them. Energy dissipated by viscosity in tho shortest wavelenghts, although the rate of dissipation of energy is set by long-wavelenght motion at the start of the cascade. The shortest wavelenght simply adjust accordingly.

The vortex stretching is a characteristic of motion properly three-dimensional, indeed the vortex lines in the flow are non parallel, but they are skewed. In general, in turbulent flow, there is vorticity. The vortex stretching is associated to an increment of the vorticity in the stretching direction. The energy cascade is due to the vortex stretching because, during the stretching, the dimension of the vortexes decreases and the large eddies are split in small eddies.

The vortexes are coherent structures of the turbulent flow. According to Robinson [57] a vortex is defined as a characteristic of the flow such that *the streamlines mapped onto plane normal to the vortex core exhibit a roughly circular or spiral pattern, when viewed form a reference frame moving with the center of the vortex core.* Theodorsen [62] presented a hypothesis to explain the formation of some particular vortexes in the boundary layer. The velocity away from the wall is higher than the one near the wall, the middle part of the vortex line is stretched into an elongated structure. At low Reynolds numbers, the vortexes behave as vortex with much less elongation; in buffer layer the vortexes are parallel

to the current (quasi-streamwise vortexes [27, 57]). At high Reynolds numbers, the vortexes are strongly elongated.

The presence of coastal defence works in nearshore areas influence and modify the wave propagation and wave-induced currents. The interaction between waves and coastal works can produce local erosion phenomena due to the occurrence of unsteady quasi-periodic vortex structures.

In this chapter, the proposed numerical model is applied to simulate the hydrodynamic phenomena produced by the interaction between waves and an emerged barrier, located in the surf zone parallel to the coastline. According to the URANS approach, the complete spectrum of the stochastic turbulent motion is represented by the proposed $k-\omega$ turbulence model. The adoption of this turbulence model, in conjunction with the new high-order shock-capturing numerical scheme allows to directly simulate both the large-scale circulation patterns downstream of the barrier and the onset of quasi-periodic vortex structures close to the edge of the barrier.

7.1 Results and discussion

In this section, the numerical results of the simulation of the interaction between an emerged barrier parallel to the shoreline and breaking waves, obtained with the new $k-\omega$ turbulence model and the high-order numerical scheme, is presented.

The numerical simulation is made on a domain that is a portion of a coastal area $20m$ long, $6m$ wide and $1m$ high. The undisturbed water depth is $h = 0.40m$; before $x = 0.0m$ the sea bottom is flat and after the bottom has a slope $1 : 35$. An emerged barrier is placed between $7.1m \leq x \leq 7.6m$ and $-1.0m \leq y \leq 1.0m$. In Figs. 7.1, a plan view and a vertical section of the domain are shown; the emerged barrier is indicated in black in the figures.

The computational domain has a spatial discretization step that range between $\Delta x = 0.050m$ and $\Delta y = 0.050m$ away from the barrier and $\Delta x = 0.025m$ and $\Delta y = 0.025m$ around the barrier. In the vertical direction, 22 non-uniform layers are adopted. As it is possible to notice from Fig. 7.2, the domain is symmetric with respect to x-axis and for this reason the numerical simulations are made in half of the original domain in order to save the computational time. A three-

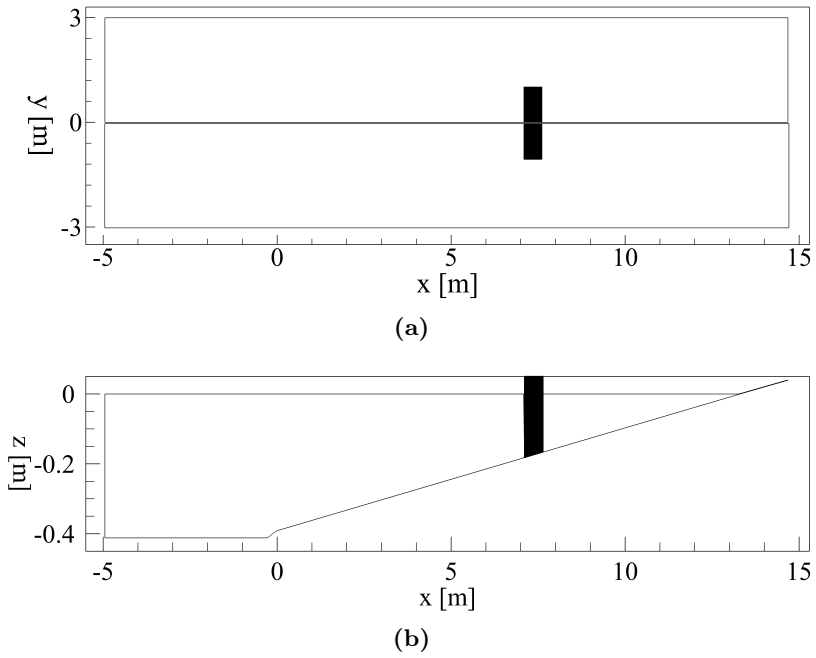

Figure 7.1: Domain of a portion of coastal area. (a) Plan view; (b) vertical section.

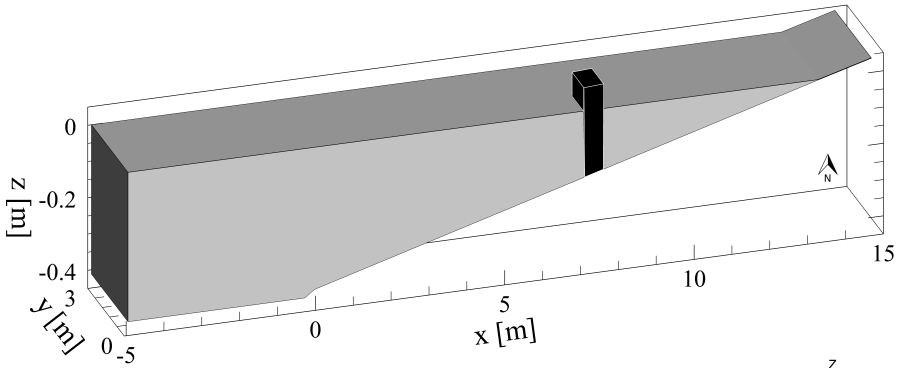

Figure 7.2: Half domain of a portion of coastal area. Three-dimensional view.

dimensional view of the computational domain is represented in Fig. 7.2. A plan view and a vertical section of the computational domain are shown in Figs. 7.3, in which one line every four is drawn in the horizontal directions and one line every two is drawn in vertical direction.

On the west side boundary of the computational domain $x = -5.0m$, cnoidal wave trains with wave height $H = 0.125m$, wave period $T = 2.0s$ and wavelenght $L = 6.35m$ are numerically reproduced. On the east side boundary, a wet and dry technique is adopted. On the south side boundary $y = 0.0m$, a closed boundary condition is imposed with null gradient of the free-surface elevation and tangential flow velocity components and zero normal velocity. On the north side boundary $y = 3.0m$, an open boundary condition is imposed with null gradient of free-

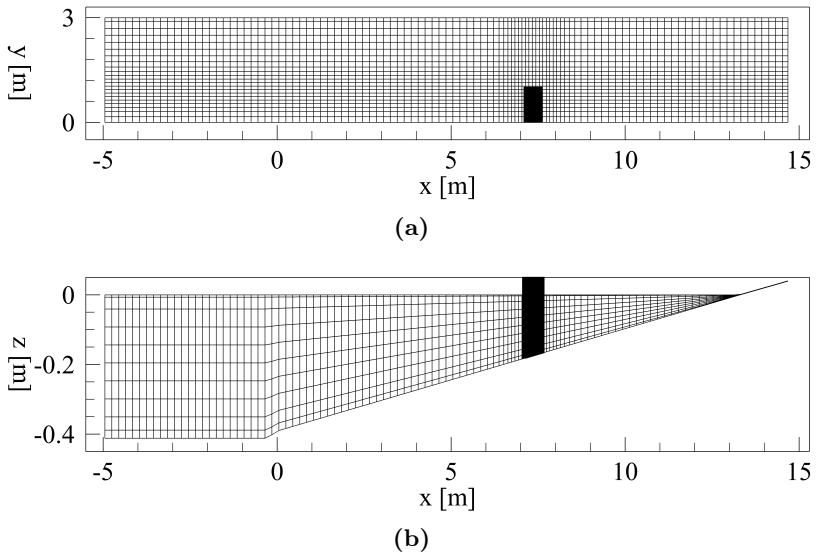

Figure 7.3: Computational domain. (a) Plan view; (b) vertical section (one line every four is drawn in the horizontal directions and one line every two is drawn in vertical direction).

surface and flow velocity components. At the bottom $z = 0.0m$, no-slip condition of the velocity is imposed.

According to Ting and Kirby test case [63], the wave breaking point, with this particular geometry and these initial conditions, is at $x = 6.4m$ and so the emerged barrier is in the breaking zone. For this reason, the new $k-\omega$ turbulence model is adopted to numerically simulate the interaction between the emerged barrier and the breaking waves.

Instantaneous wave fields are shown in Figs. (the barrier is represented in the figures through rectangles in which only the perimeter is represented). This wave fields are taken after about 47 subsequent waves, when the results reach quasi-steady state ($T_s = 95.7s$). From these figures, it is possible to see the wave breaking before the barrier, the increase of the wave height due to the impact with the barrier, the propagation of the wave breaking front along the side of the barrier, the diffraction and the reflection of the wave front due to the presence of the barrier.

In Fig. 7.4(a), the wave front has not yet reached the surf zone in which the emerged barrier is placed. Behind the barrier, the previous wave front has undergone a diffraction due precisely to the presence of the emerged barrier. In Fig. 7.4(b), the wave height increases because of the shoaling. At around $x =$

6.5m, the wave breaks and the reduction of the wave height due to the wave breaking is shown in Fig. 7.4(c). In Fig. 7.4(c), it is possible to notice that the wave height does not reach the maximum value. In Figs. 7.4(d) and (e), the wave front impacts on the barrier and the wave height increases a lot. Meanwhile, the wave breaking front passes along the side of the barrier. In Fig. 7.4(f), the wave front before the barrier is reflected in the direction opposite to the wave propagation direction. In Figs. 7.4(g) and (h), it is possible to see the diffraction of the wave front behind the barrier, in the region in front of the coastline.

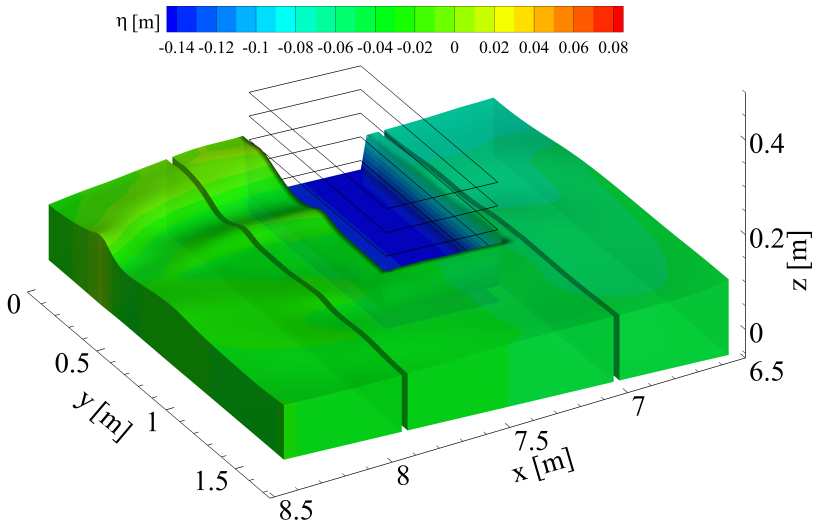

(a)

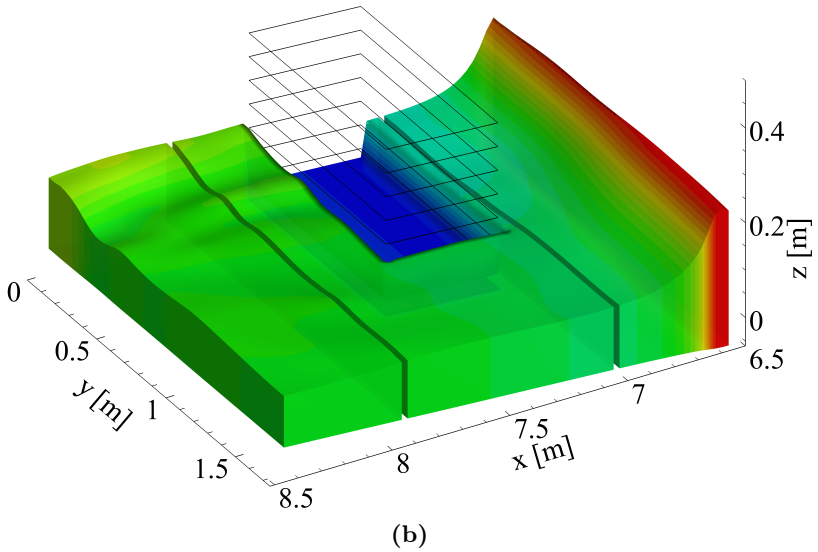

(b)

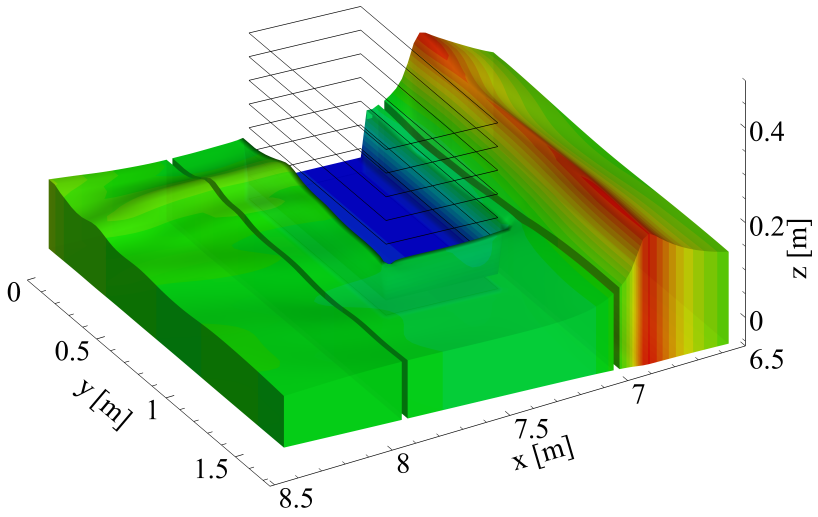
0.4
0.2
z [m]
0
6.5
0
0.5
y [m]
1
1.5
8.5
8
7.5
7
x [m]

(c)

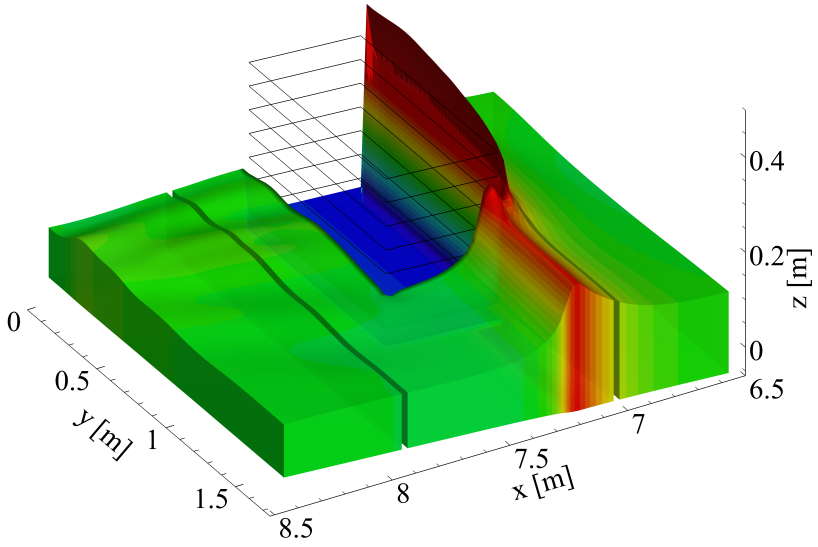
0.4
0.2
z [m]
0
6.5
0
0.5
y [m]
1
1.5
8.5
8
7.5
7
x [m]

(d)

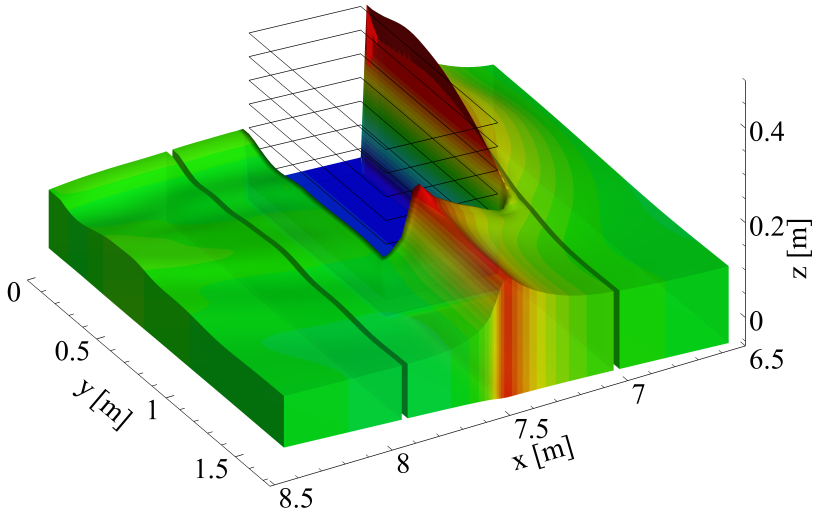
0.4
0.2
z [m]
0
6.5
0
0.5
y [m]
1
1.5
8.5
8
7.5
7
x [m]

(e)

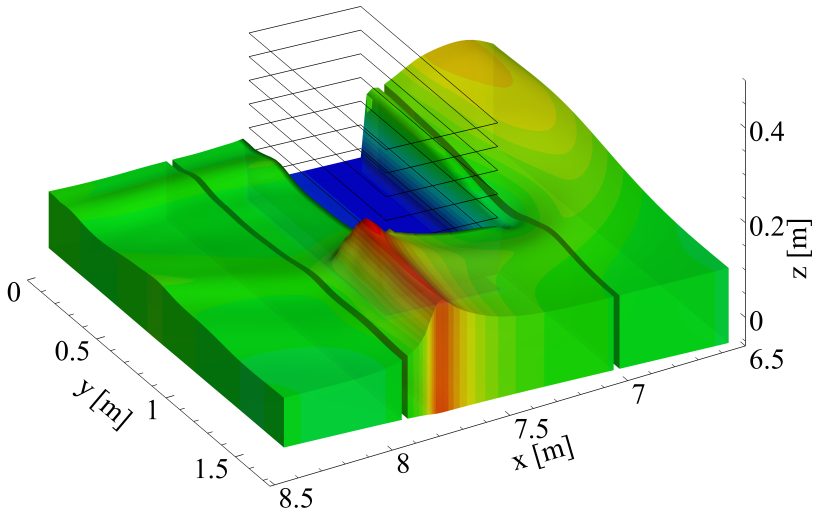

(f)

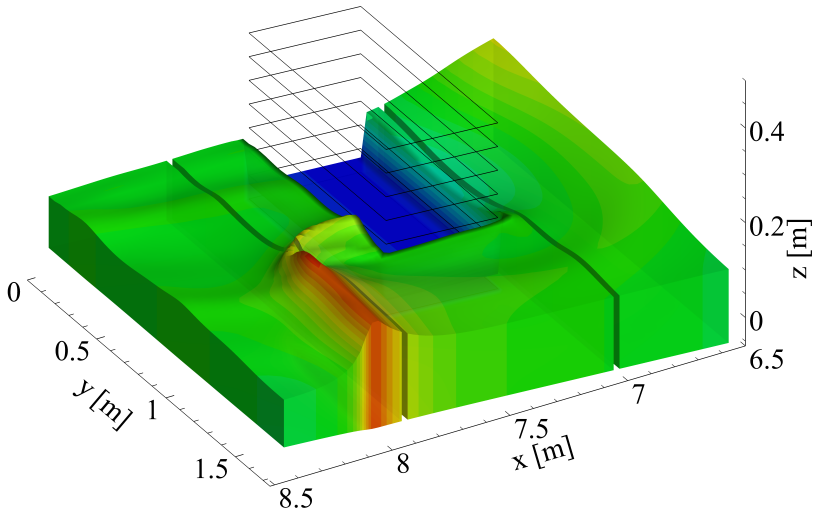

(g)

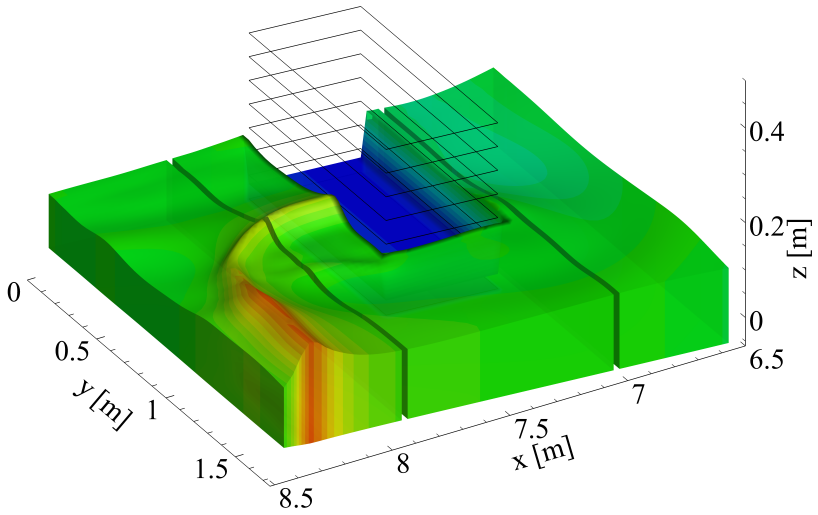

(h)

Figure 7.4: Instantaneous wave fields. (a) $T_s = 95.9s$; (b) $T_s = 96.1s$; (c) $T_s = 96.3s$; (d) $T_s = 96.5s$; (e) $T_s = 96.7s$;(f) $T_s = 96.9s$; (g) $T_s = 97.1s$; (h) $T_s = 97.4s$.

In Figs. 7.5, the circulation patterns are shown at different vertical distances from the bottom: near the bottom, in the intermediate water depth and near the free surface. The velocities are averaged over time. Upstream of the barrier near the bottom, the wave trains impact against the barrier and induced a mean gradient of the free-surface elevation. In this zone, the velocity is offshore directed near the bottom, as shown from Fig. 7.5(a), while near the free surface, the velocity is onshore directed, Fig. 7.5(c). This particular phenomena is called undertow. Along the lateral boundary (north-side boundary) of the barrier, the flow velocity is onshore directed. Close to this lateral boundary, a small clockwise vortex can be seen near the bottom and in intermediate water depth. Downstream of the barrier, a mean gradient of the free-surface elevation induces flow velocities that are directed to the sheltered area. In the zone behind the barrier, a clockwise vortex is generated ($8.0m < x < 8.5m$ and $0.0m < y < 1.0m$) and its intensity increases upon approaching the intermediate water depth (Fig. 7.5(b)). Near the free surface, the velocity before the barrier is onshore directed (Fig. 7.5(c)).

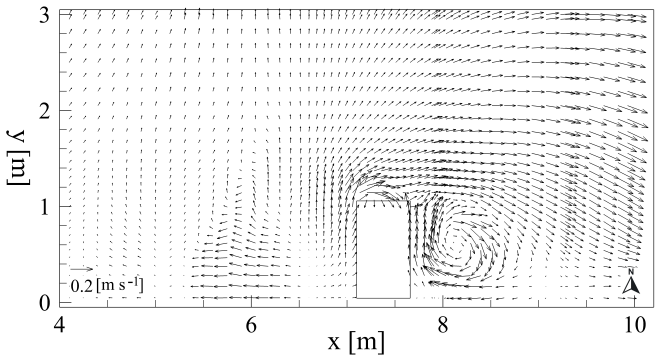

(a)

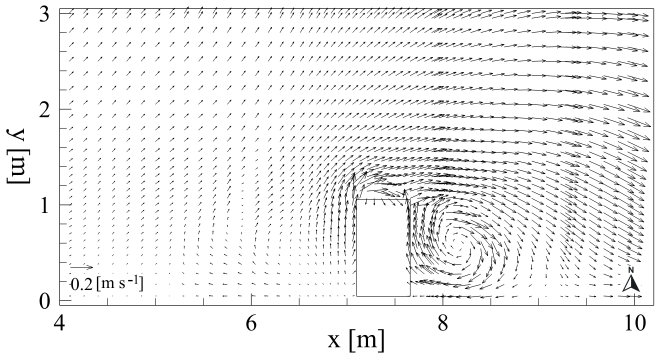

(b)

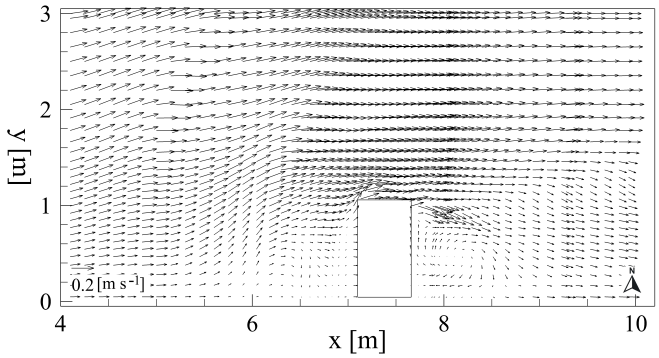

(c)

Figure 7.5: Circulation pattern. (a) At the bottom; (b) intermediate depth; (c) near the free surface. Only one out of every three vectors are drawn.

In order to study the interaction between waves and coastal works, it is necessary to simulate the unsteady quasi-periodic vortex structures that occur near the coastal works.

Figs. 7.6 show the instantaneous local vortex structures close to the boundaries of the emerged barrier (the barrier is represented in the figures through rectangles in which only the perimeter is represented). Q-criterion is used to visualized the vortex structures. In this method, a vortex is identified by the three-dimensional contours of the second invariant of the velocity gradient tensor (in Appendix D, Q-method [15, 35] is explained). All the instantaneous fields showed in this thesis are taken when the results reach quasi-steady state.

The presence of the emerged barrier causes, near the edge, the onset of quasi-periodic vortex structures. In Fig. 7.6(a), the wave front has not yet reached the surf zone. Near the two corners of the emerged barrier, two vortexes with a vertical axis arise. Downstream of the emerged barrier, other vortexes generated at the upstream edge of the barrier arise and are characterized by almost horizontal axes (x-axis). Behind the barrier in the sheltered area, an horizontal vortex (y-axis) is generated near the bottom and it is permanent during all the simulations. In Figs. 7.6(b) and (c), the vortexes with vertical axis are still near the corners of the emerged barrier. In Fig. 7.6(d), the wave front impacts against the barrier and after that the vortex near the first corner ($y = 7.1m$) is stretched along the north edge of the barrier (Fig. 7.6(e)). When the wave front arrives near the second corner, also the second vortex with vertical axis is stretched in the wave propagation direction, as it is possible to see by Figs. 7.6(f)-(h). The vortexes that

are stretched on the north edge of the emerged barrier ($y = 1.0m$) are near the free surface and break into smaller vortexes. In all the figures, the vortex behind the barrier in the sheltered area ($y = 8.0m$), is present near to the bottom.

The three-dimensional quasi-periodic vortex structures shown in Figs. 7.6(a)-(h) can produce local erosion phenomena at the toe of barrier and the breaking of the emerged barrier.

Some vertical and horizontal sections (represented by red lines in Fig. 7.7) are shown in the following figures to better understand how these vortex structures can interact with the emerged barrier.

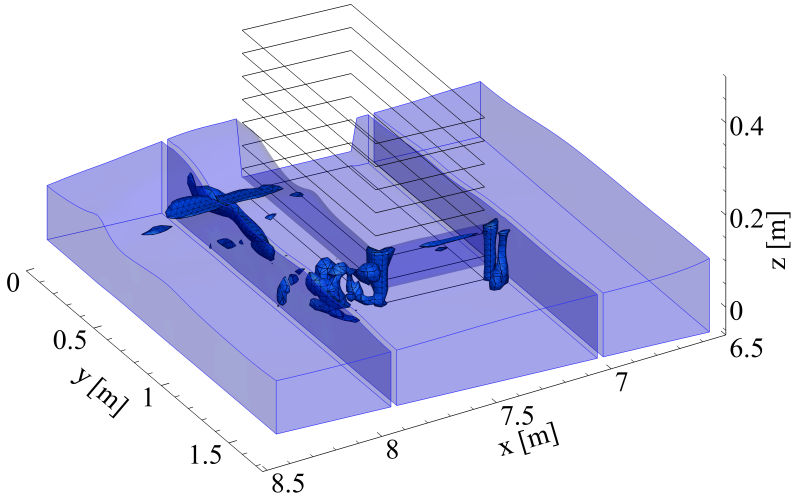

(a)

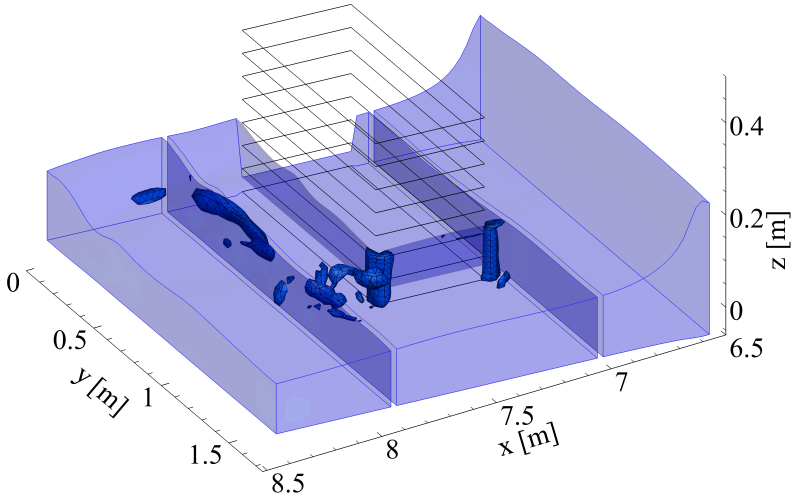

(b)

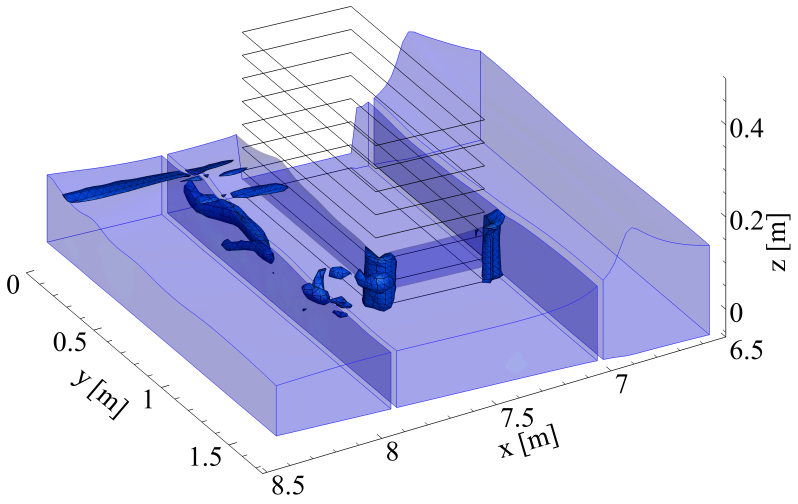
0
0.5
y [m]
1
1.5
8.5
8
7.5
x [m]
7
6.5
0
0.2
0.4
z [m]

(c)

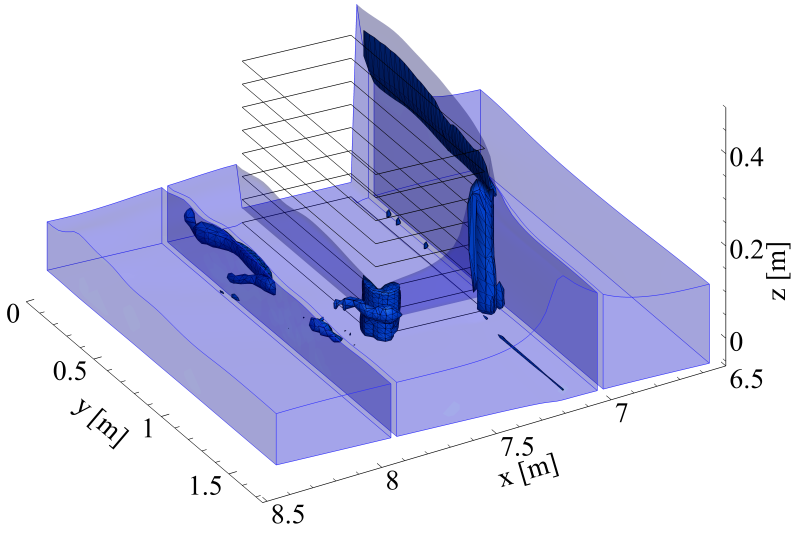
0
0.5
y [m]
1
1.5
8.5
8
7.5
x [m]
7
6.5
0
0.2
0.4
z [m]

(d)

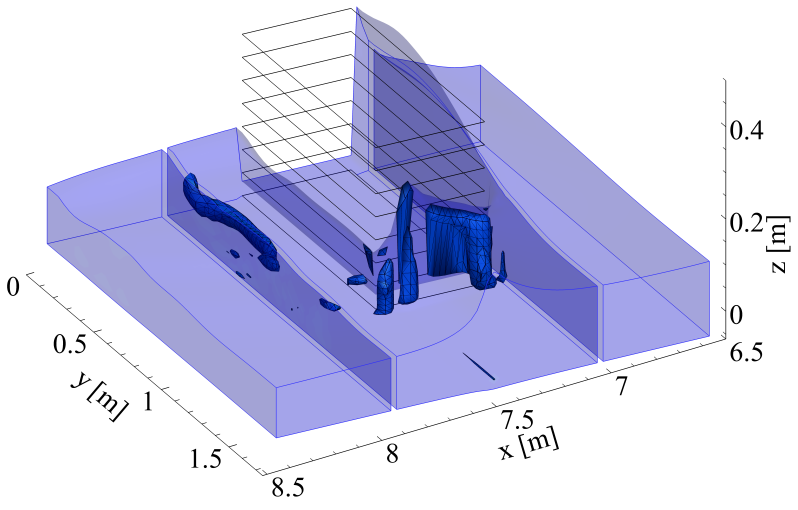
0
0.5
y [m]
1
1.5
8.5
8
7.5
x [m]
7
6.5
0
0.2
0.4
z [m]

(e)

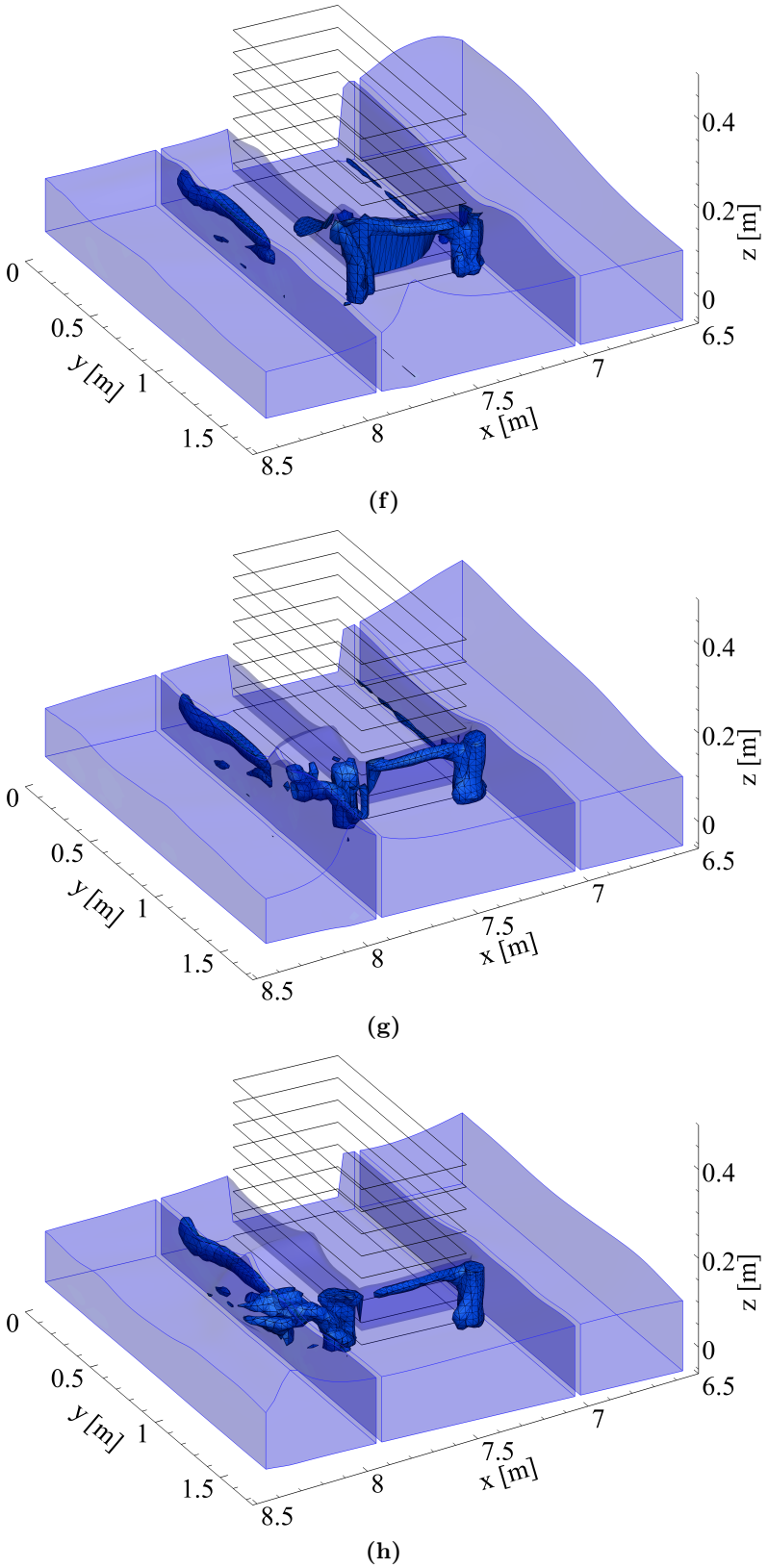

Figure 7.6: Instantaneous vortex structures visualized using Q-criterion (three-dimensional contours of the second invariant of the velocity gradient tensor). (a) $T_s = 95.9s$; (b) $T_s = 96.1s$; (c) $T_s = 96.3s$; (d) $T_s = 96.5s$; (e) $T_s = 96.7s$; (f) $T_s = 96.9s$; (g) $T_s = 97.1s$; (h) $T_s = 97.4s$. The emerged barrier is inside thin black lines.

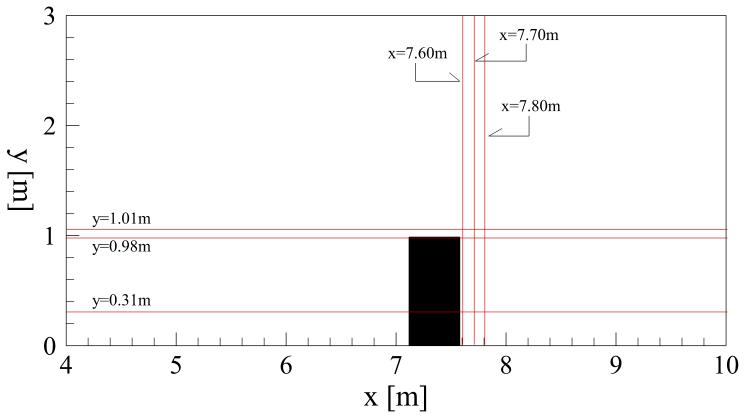

Figure 7.7: Vertical sections.

In Figs. 7.8, a sequence of four plan view of the instantaneous vortex structures near the bottom are shown. The four instants are taken during the propagation of the braking wave from deep water to the coastline, at (a) $T_s = 95.9s$, (b) $T_s = 96.3s$, (c) $T_s = 96.9s$ and (d) $T_s = 97.4s$.

In these figures at every instants, it is possible to notice two principal vortexes with vertical axes near the two corners of the emerged barrier. These vortexes can produce the undermining of the foundations of the emerged barrier. The permanent vortex in the sheltered, behind the barrier, can be observed in all the figures.

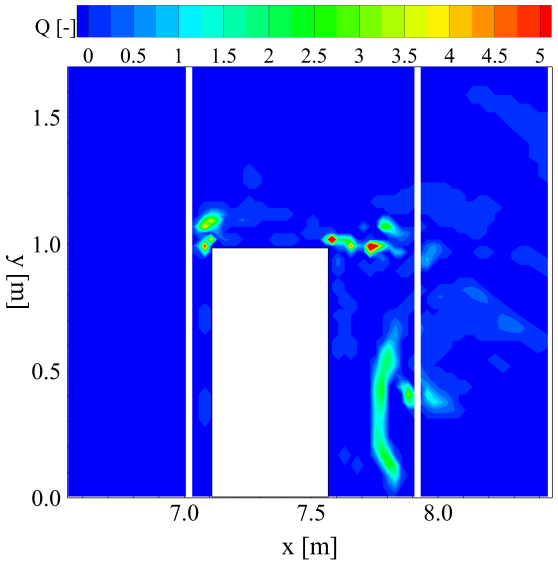

(a)

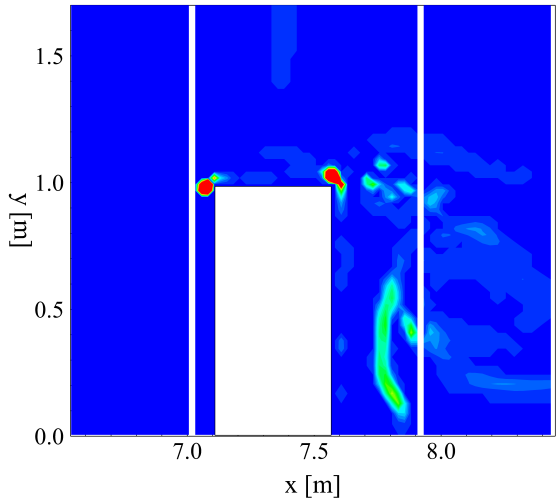

(b)

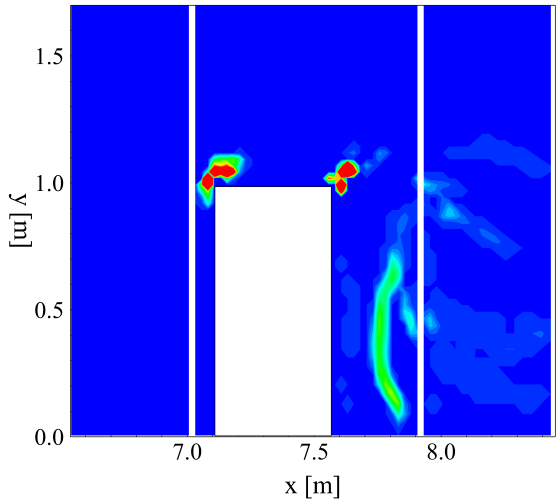

(c)

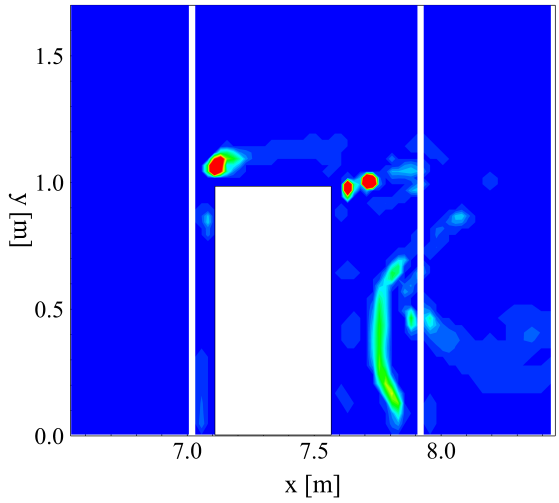

(d)

Figure 7.8: Plan sections of instantaneous vortex structures visualized by Q-criterion near the bottom at (a) $T_s = 95.9s$, (b) $T_s = 96.3s$, (c) $T_s = 96.9s$ and (d) $T_s = 97.4s$.

In Figs. 7.9, the same sequence of four plan view of the instantaneous vortex structures, presented above, are shown in the intermediate water depth.

In the intermediate water depth, the vortex near the two corners of the emerged barrier is still present. The incoming wave produces the stretching of the vortexes in the wave propagation direction. The stretching is evident in Figs. 7.9(a) and (b), because the wave front is already passed away the barrier and the new incoming wave front is still in deep water. In Figs. 7.9(d), the wave front is near the east side boundary of the emerged barrier: the stretching of vortexes generated near the corner is evident. The vortex behind the barrier, at intermediate water depth, is not present at this distance from the bottom.

By comparing Figs. 7.8 and Figs. 7.9 at the same instants, it is possible to notice that the vortexes, that have vertical axes and are generated at the bottom near the barrier, are stretched in the wave propagation direction and reached the intermediate water depth.

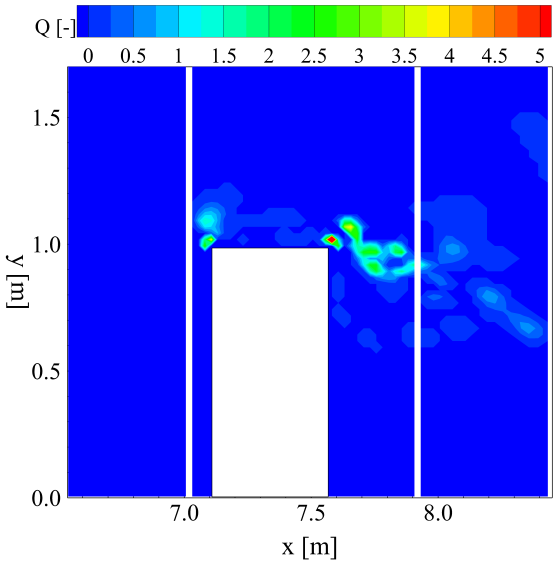

(a)

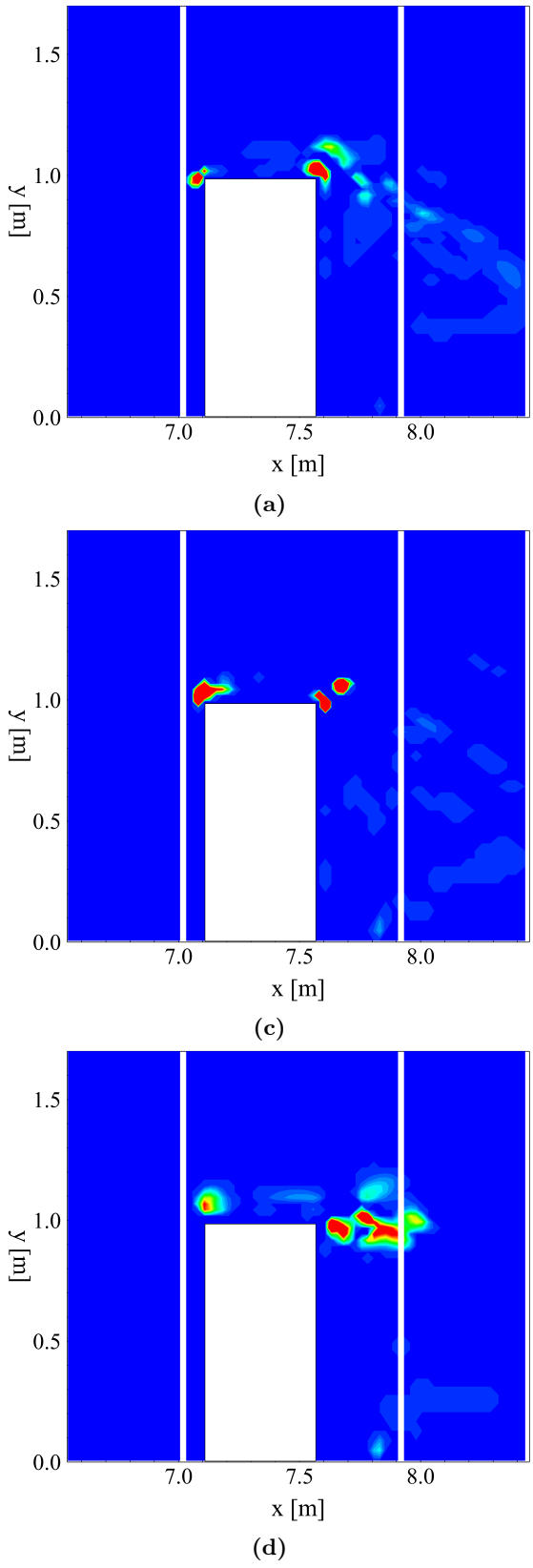

Figure 7.9: Plan sections of instantaneous vortex structures visualized by Q-criterion at the intermediate water depth at (a) $T_s = 95.9s$, (b) $T_s = 96.3s$, (c) $T_s = 96.9s$ and (d) $T_s = 97.4s$.

In Figs. 7.10, three vertical sections (at $x = 7.60m$ behind the barrier in the sheltered area) of the instantaneous vortex structures are shown. The sequence is taken at (a) $T_s = 96.5s$, (b) $T_s = 96.9s$ and (c) $T_s = 97.4s$. In all the following figures, the emerged barrier is not represented. It is possible to see from the figures that the vortex with vertical axis that is generated at the corner of the barrier ($y = 1.0m$). When the wave passes over the barrier, this vortex is stretched in the wave propagation direction, indeed in Fig. 7.10(c), the vortex has low intensity. These vortexes near the bottom corner of the barrier can undermine the foundations of the emerged barrier.

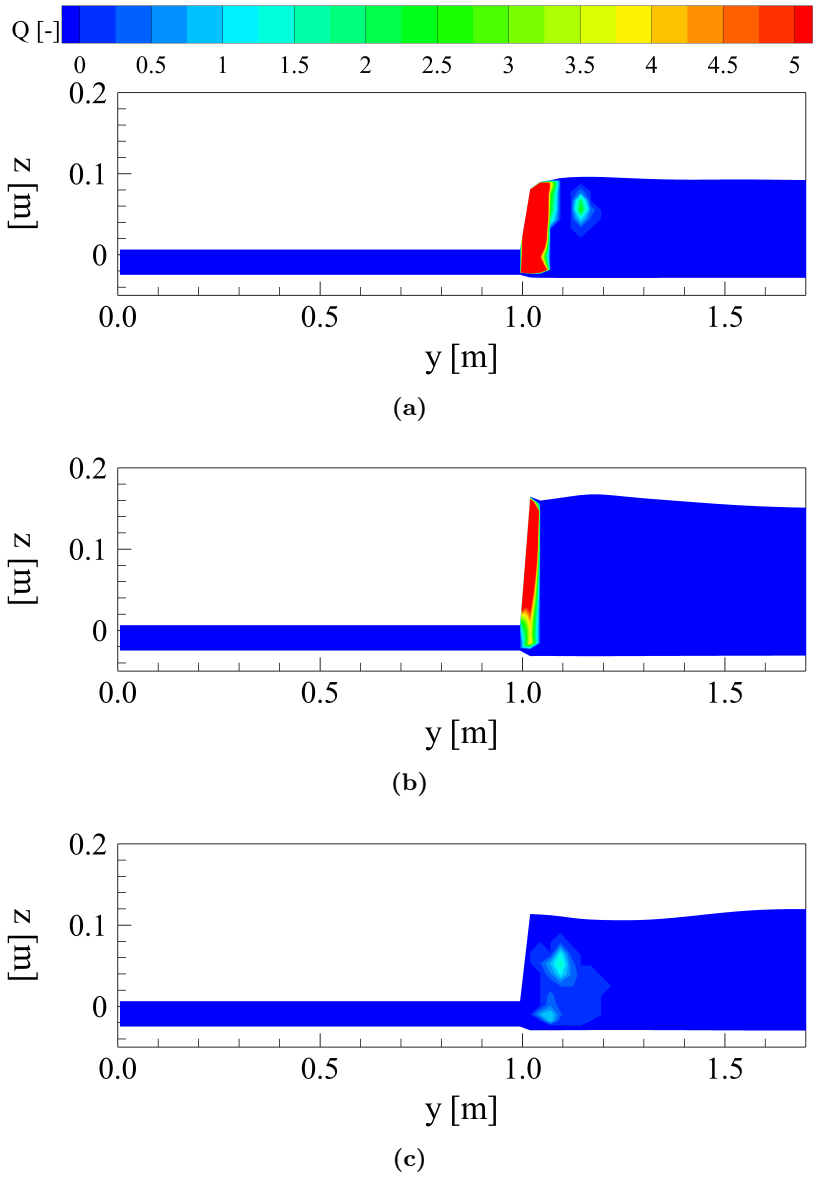

Figure 7.10: Vertical sections of instantaneous vortex structures visualized by Q-criterion at $x = 7.60m$: (a) $T_s = 96.5s$, (b) $T_s = 96.9s$ and (c) $T_s = 97.4s$.

In Figs. 7.11, three vertical sections (at $x = 7.70m$ behind the barrier in the sheltered area) of the instantaneous vortex structures are shown. The sequence is taken at the same time of the previous figures (Figs. 7.10) (a) $T_s = 96.5s$, (b) $T_s = 96.9s$ and (c) $T_s = 97.4s$.

At $T_s = 96.5s$ (Fig. 7.11(a)), the incoming wave has not reached the area behind the barrier. The vortex structures present at this time are stretched by the previous wave. Some vortexes are in correspondence of the corner of the barrier. At $T_s = 96.9s$ (Fig. 7.11(b)), the wave comes from deep water and stretches the vortex that was at the corner of the barrier. This vortex is stretched in the wave propagation direction and moves away from the bottom. In the last snapshot (Fig. 7.11(c)), the vortexes are located in all the water column, because the wave fronts reached the sheltered area and stretched all the vortexes that were generated by the interaction between the waves and the barrier.

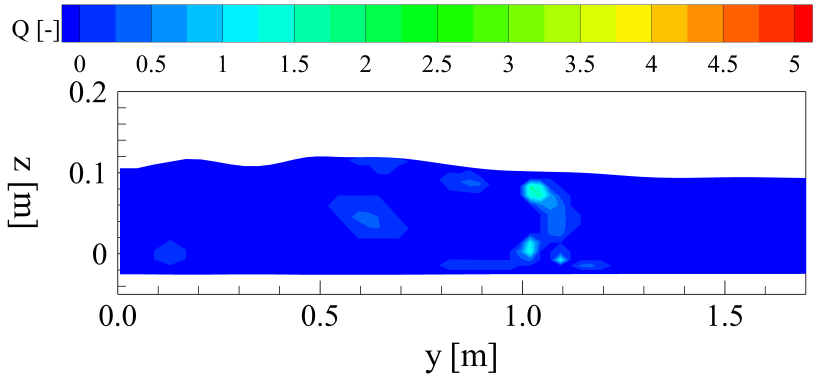

(a)

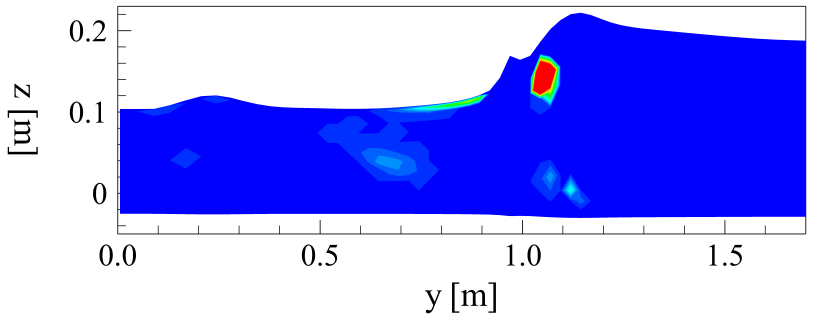

(b)

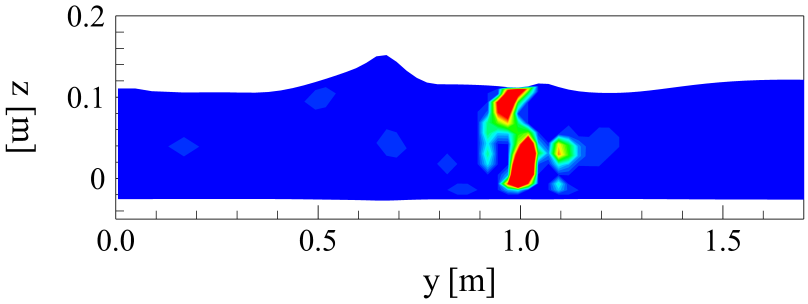

(c)

Figure 7.11: Vertical sections of instantaneous vortex structures visualized by Q-criterion at $x = 7.70m$: (a) $T_s = 96.5s$, (b) $T_s = 96.9s$ and (c) $T_s = 97.4s$.

In Figs. 7.12, three vertical sections (at $x = 7.78m$ behind the barrier in the sheltered area) of the instantaneous vortex structures are shown. The sequence is taken at the same time of the previous figures (Figs. 7.10 and Figs. 7.11) (a) $T_s = 96.5s$, (b) $T_s = 96.9s$ and (c) $T_s = 97.4s$.

In the sheltered area at $x = 7.78m$, in all the snapshots in Figs. 7.12, the big horizontal long vortex near the bottom can be seen. The vortexes in correspondence of the corner of the barrier ($y = 1.0m$) have been stretched along the structures by the passage of the wave front on the north side boundary. The stretched vortexes are shown in Fig. 7.12(c).

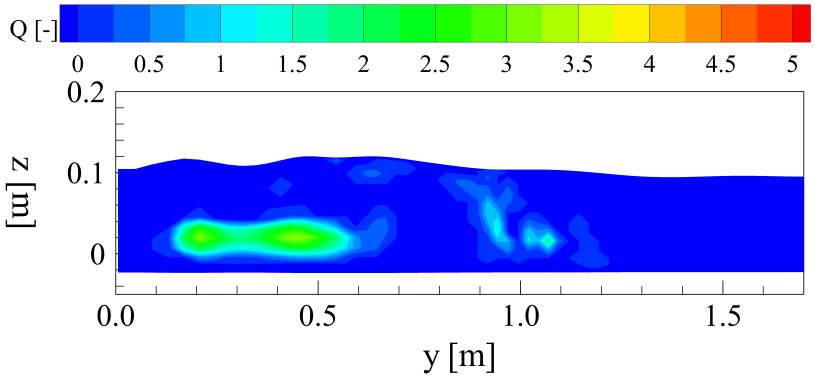

(a)

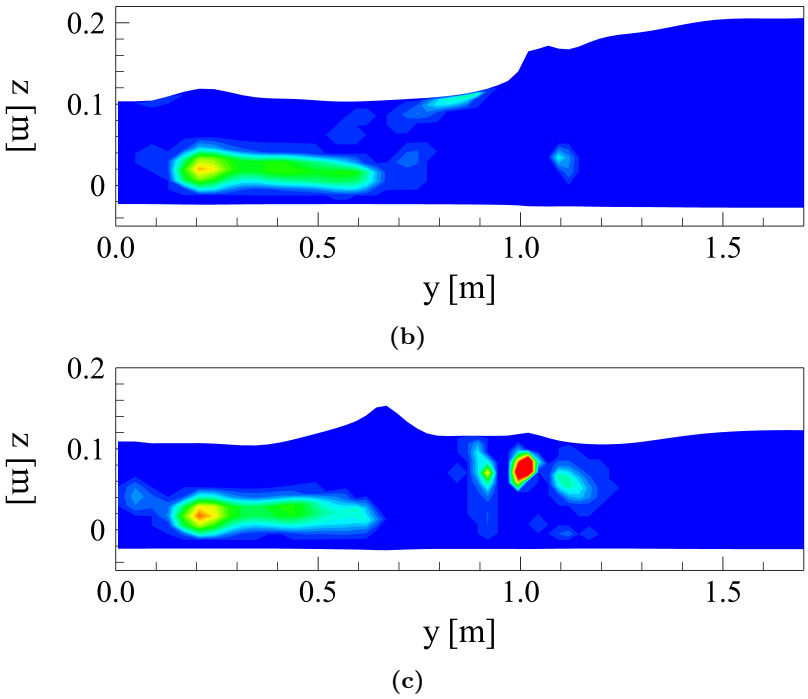

Figure 7.12: Vertical sections of instantaneous vortex structures visualized by Q-criterion at $x = 7.78m$: (a) $T_s = 96.5s$, (b) $T_s = 96.9s$ and (c) $T_s = 97.4s$.

In Figs. 7.13, three vertical sections (at $y = 0.31m$) of the instantaneous vortex structures are shown. The sequence is taken at (a) $T_s = 95.9s$, (b) $T_s = 96.7s$ and (c) $T_s = 97.4s$. In all the following figures, the emerged barrier is not represented.

In this sections, it is possible to notice the coherent vortex behind the barrier at $y = 7.80m$. The intensity of the vortex grows, when the wave passes away from the barrier (Fig. 7.13(c)). In Fig. 7.13(b), the wave front that impacts against the barrier can be seen.

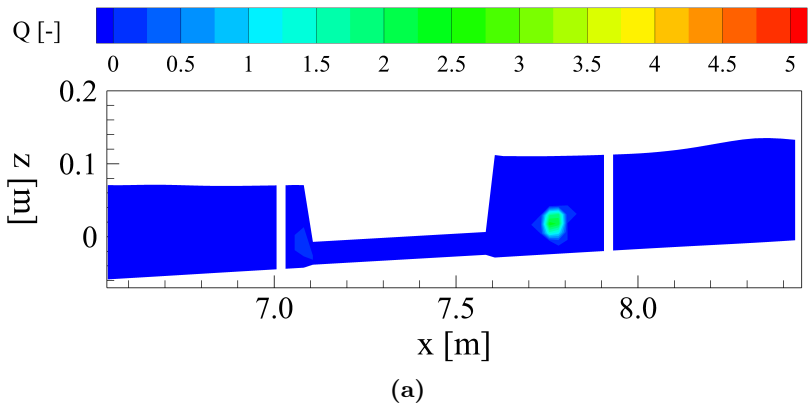

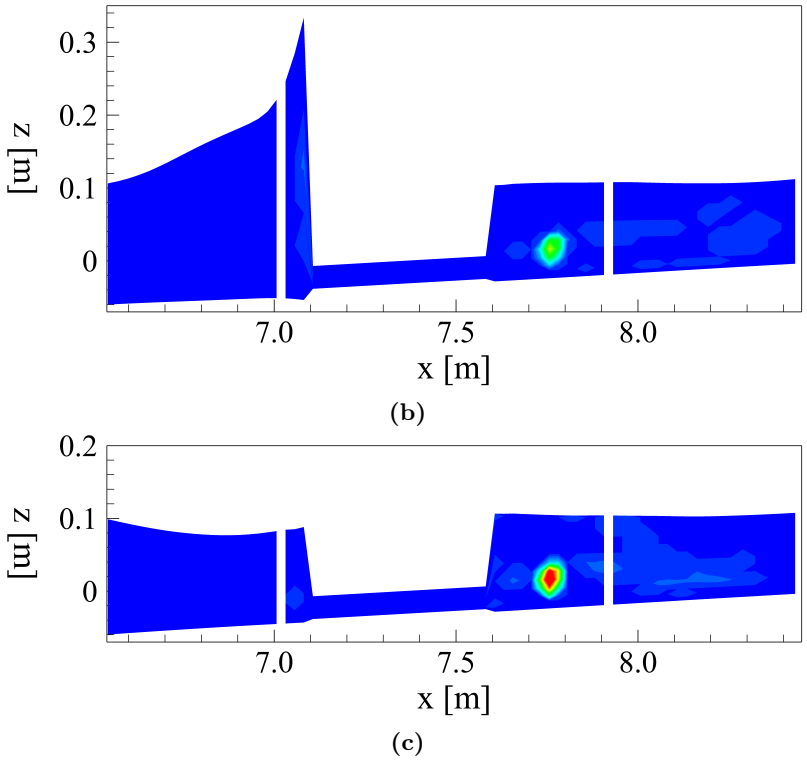

Figure 7.13: Vertical sections of instantaneous vortex structures visualized by Q-criterion at $y = 0.31m$: (a) $T_s = 95.9s$, (b) $T_s = 96.7s$ and (c) $T_s = 97.4s$.

In Figs. 7.14, three vertical sections (at $y = 0.98m$) of the instantaneous vortex structures are shown. The sequence is taken at the same time of the previous figures (Figs. 7.14) (a) $T_s = 95.9s$, (b) $T_s = 96.7s$ and (c) $T_s = 97.4s$.

The vortexes, generated by the interaction between the structures and the waves, at the north-east corner ($7.80m < x < 7.90m$) of the barrier can be seen in Figs. 7.14(a) and (c). These vortexes are generated near the bottom, in the oscillating wave boundary layer, and are stretched by the wave passage, as shown in Fig. 7.14(c). In this figure, the vortexes are stretched in the wave propagation direction from the bottom to the free surface. In Fig. 7.14(b), in the sheltered area, there are no vortexes, because the wave behind the barrier reached the coastline and the new wave, coming from deep water has already impacted the barrier.

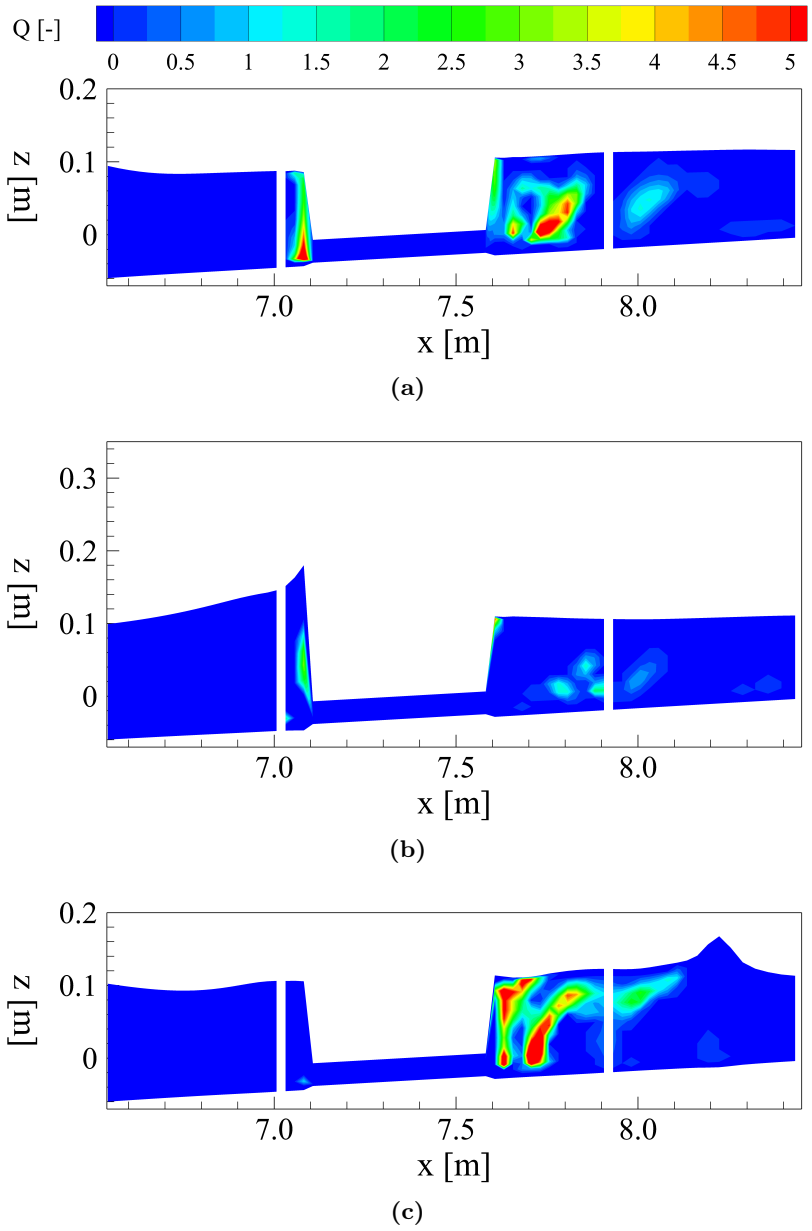

Figure 7.14: Vertical sections of instantaneous vortex structures visualized by Q-criterion at $y = 0.98m$: (a) $T_s = 95.9s$, (b) $T_s = 96.7s$ and (c) $T_s = 97.4s$.

The numerical results demonstrate that, by using the new 5^{th}-order shock-capturing numerical scheme and the new $k - \omega$ turbulence model, it is possible to simulate both the large-scale circulation patterns downstream of the barrier and the onset of quasi-periodic vortex structures close to the edge of the barrier. The simulation of these hydrodynamic phenomena can be a useful tool for coastal engineering problems.

Chapter 8

Conclusions

In this thesis, a new model for the simulation of the breaking waves is proposed. This model is based on the solution of the three-dimensional equations of motion expressed in contravariant formulation. These equations are in integral form and are expressed in terms of the conserved variables H and $H\vec{u}$ (H is the total water depth and $\vec{u}$ is fluid velocity vector).

The three-dimensional ensemble-averaged motion equations are solved by a new high-order shock-capturing numerical schemes. The elements of novelty in this new numerical scheme are two. The first element of novelty consists in the proposal of a new reconstruction technique of the point values of the conserved variables on the cell faces of the computational grid (starting from the cell-averaged values of the same variables). This reconstruction technique is named WTENO and it is specifically designed for the three-dimensional simulation of breaking waves. The second element of novelty consists in the use of an exact solution for the Riemann problem to advancing in time the point values of the conserved variables at the cell faces.

In this thesis, it is demonstrated that the new high-order shock-capturing numerical scheme limits the numerical dissipation, leaving the task of dissipating the kinetic energy of the ensemble-averaged motion to the turbulence model. The numerical results obtained by the high-order numerical scheme (with the Smagorinsky turbulence model) are in better agreement with the experimental measurements than the ones obtained by the low-order numerical scheme.

In this thesis, two turbulence models, $k-l$ and $k-\omega$ (k is the turbulent kinetic

energy, l is the mixing length and ω is the dissipation of the turbulent kinetic energy per unit of turbulent kinetic energy, hereinafter called specific dissipation rate), are proposed. These models are collocated in the context of the URANS models and intervene in the ensemble-averaged momentum equation in order to directly simulate the largest part of the unsteady quasi-periodic vortex structures, leaving the task of dissipating the complete spectrum of the stochastic motion to the statistical turbulence model.

In the new $k-l$ turbulence model, the k-equation is written in a new integral contravariant form on a generalized time-dependent curvilinear coordinate system. In this model, a new formula of the mixing length outside the oscillating wave boundary layer is proposed. The mixing length is calculated as a function of the first and second spatial derivatives of the local maximum water surface elevation. In the oscillating wave boundary layer, the mixing length is calculated by the hypothesis of the balance between production and dissipation of turbulent kinetic energy.

The numerical results demonstrates that the new $k-l$ turbulence model is able to represent in different way the turbulence phenomena before and around the wave breaking point and in the surf zone. In particular, it is demonstrated that by solving the equations of motion also in the buffer layer and the k-equation also in the proximity of the viscous sublayer, it is possible to better take into account the effects that the turbulent phenomena have in the dissipation of the kinetic energy of the ensemble-averaged motion in the oscillating wave boundary layer.

The numerical results show that the equations of motion and the turbulent kinetic energy equation must be necessary solved also in the buffer layer of the oscillating wave boundary layer and consequently, they show the necessity to develop turbulence models that are able to overcome the limits of the $k-l$ turbulence model.

In the new $k-\omega$ turbulence model, the k and ω equations are written in a new integral contravariant form on a generalized time-varying curvilinear coordinate system. The new $k-\omega$ turbulence model admits the possibility to assign the boundary condition for the specific dissipation rate directly at the bottom. The production of turbulent kinetic energy in the zone between the breaking wave

fronts and the oscillating wave boundary layer is reduced by a dynamic coefficient for the dissipation of ω and by introducing a limiter in the eddy viscosity.

The new $k-\omega$ turbulence model overcomes the limits of the $k-l$ turbulence models: indeed, the hypothesis of the balance between production and dissipation of turbulent kinetic energy in all the turbulent core is removed.

The new formulation for the eddy viscosity limits the production of turbulent kinetic energy in the zone between the wave breaking fronts and the oscillating wave boundary layer, the excessive reduction of the wave height and an anticipation of the wave breaking point, as it happens in the standard $k-\omega$ turbulence model.

From the comparison between the experimental measurements and numerical results obtained by the new $k-\omega$ turbulence model and by the new high-order shock-capturing numerical scheme, it is possible to notice that this new model is able to correctly evaluate the wave height in the shoaling zone, the wave breaking point and wave height in the surf zone. From the numerical results, it is also clear that the new $k-\omega$ turbulence model is able to correctly evaluate the time mean vertical distribution of the turbulent kinetic energy and the horizontal flow velocity.

In this thesis, it is demonstrated that, by using the new 5^{th}-order shock-capturing numerical scheme and the new $k-\omega$ turbulence model, it is possible to simulate both the large-scale circulation patterns downstream of the barrier and the onset of quasi-periodic vortex structures close to the edge of the barrier. The simulation of these hydrodynamic phenomena can be a useful tool for coastal engineering problems. By using the contravariant formulation of the equations on a time dependent curvilinear coordinate system, it is possible to reproduce the complex geometries of the coastal areas with no limitation on the the applicability for real-scale numerical simulations. In the case of a real-scale numerical simulation, to save the computational time, the computational domain requires the use of grid cells refined only around the coastal defence works and at the bottom in order to correctly simulate the unsteady quasi-periodic vortex structure, bearing in mind the coastal engineering problems.

Bibliography

[1] R. Aris. *Vectors, Tensors and the Basic Equations of Fluid Mechanics*. Dover, New York USA, 1989.

[2] Battjes. Surf similarity. *Coastal Engineering Proceedings*, 1(14):466—-480, 1974.

[3] E. Berberović, N. van Hinsberg, and I. V. Jakirlić. Drop impact onto a liquid layer of finite thickness: dynamics of the cavity evolution. *Physical Review E*, 79:036306, 2009.

[4] R. Borges, M. Carmona, B. Costa, and W. S. Don. An improved weighted essentially non-oscillatory scheme for hyperbolic conservation laws. *Journal of Computational Physics*, 227:3191–3211, 2008.

[5] G. Bosh and W. Rodi. Simulation of vortex shedding past a square cylinder with different turbulence models. *International Journal of Numerical Methods and Fluids*, 28:601–616, 1998.

[6] S. F. Bradford. Numerical simulation of surf zone dynamics. *Journal of Waterway, Port, Coastal, and Ocean Engineering*, 126(1):1–13, 2000.

[7] S. F. Bradford. Godunov-based model for non-hydrostatic wave dynamics. *Journal of Waterway, Port, Coastal, and Ocean Engineering*, 131:226–238, 2005.

[8] S. F. Bradford. Non-hydrostatic model for surf zone simulation. *Journal of Waterway, Port, Coastal, and Ocean Engineering*, 137:163–174, 2011.

[9] S. F. Bradford. Improving the efficiency and accuracy of a nonhydrostatic surf zone model. *Journal of Waterway, Port, Coastal, and Ocean Engineering*, 65:1–10, 2012.

[10] G. Cannata and F. Gallerano. A dynamic two-equations sub grid scale model. *Continuum Mechanics and Thermodynamics*, 17:101–123, 2005.

[11] G. Cannata, F. Palleschi, B. Iele, and F. Cioffi. A three-dimensional numerical study of wave induced currents in the cetraro harbour coastal area (italy). *Water*, 12:935–954, 2020.

[12] G. Cannata, F. Palleschi, B. Iele, and F. Gallerano. A modified $k-\varepsilon$ turbulence model for a wave breaking simulation. *Water*, 11:2285–2295, 2019.

[13] G. Cannata, F. Palleschi, B. Iele, and F. Gallerano. A wave-targeted essentially non-oscillatory 3d shock-capturing scheme for breaking wave simulation. *Journal of Marine Science and Engineering*, 10(6):810–845, 2022.

[14] G. Cannata, C. Petrelli, L. Barsi, and F. Gallerano. Numerical integration of the contravariant integral form of the navier-stokes equations in time-dependent curvilinear coordinate systems for three-dimensional free surface flow. *Continuum Mechanics and Thermodynamics*, 31:491–519, 2019.

[15] P. Chakraborty, S. Balachandar, and R. Adrian. On the relationship between local vortex identification schems. *Journal of Fluid Mechanics*, 353:189–214, 2005.

[16] Q. Chen, J. T. Kirby, F. Dalrympe, R A ans Shi, and E. B. Thornton. Boussinesq modeling of longshore currents. *Coastal Engineering*, 108:1–18, 2003.

[17] M. S. Chong, A. E. Perry, and B. J. Cantwell. A general classification of three-dimensional flow fields. *Physics of Fluids*, 2:765–777, 1990.

[18] R. Deigaard, J. Fredsøe, and I. B. Hedegaard. Suspended sediment in the surf zone. *Journal of Waterway, Port, Coastal, and Ocean Engineering*, 112(1):115–128, 1986.

[19] R. Deigaard, P. Justesen, and J. Fredsøe. Modelling of undertow by a one-equation turbulence model. *Coastal Engineering*, 15(5-6):431–458, 1991.

[20] M. Derakhti, J. T. Kirby, F. Shi, and G. Ma. Nhwave: Consistent boundary conditions and turbulence modeling. *Ocean Modelling*, 106:121–130, 2016.

[21] R. Franke and G. Bosh. Calculation of vortex shedding past a square cylinder with various turbulence models. *Turbulent Shear Flows, Springer*, 8:189–204, 1993.

[22] L. Fu, X. Y. Hu, and A. N. A. A family of high-order tageted eno scheme for compressible-fluid simulations. *Journal of Computational Physics*, 305:333–359, 2016.

[23] F. Gallerano, G. Cannata, L. Barsi, F. Palleschi, and B. Iele. Simulation of wave motion and wave breaking induced energy dissipation. *WSEAS Transaction on Fluid Mechanics*, pages 1–8, 2019.

[24] F. Gallerano, F. Palleschi, and B. Iele. Numerical study over the effects of a designed submerged breakwater on the coastal sediment transport in the pescara harbour (italy). *Journal of Marine Science and Engineering*, 8:487–510, 2020.

[25] F. Gallerano, F. Palleschi, and B. Iele. Three-dimensional simulation of wave breaking. *Proceeding of Italian Conference on Integrated River Basin Management, University of Calabria*, 41:325–332, 2020.

[26] F. Gallerano, F. Palleschi, B. Iele, and G. Cannata. A three-dimensional high-order numerical model for the simulation of the interaction between waves and an emerged barrier. *WSEAS Transaction on Fluid Mechanics*, 17:128–139, 2022.

[27] M. R. Head and P. Brandyopadhyay. New aspects of turbulent boundary-layer structure. *Journal of Fluid Mechanics*, 107:297–338, 1981.

[28] P. Higuera, J. L. Lara, and I. J. Losada. Simulating coastal engineering processes with openfoam®. *International Journal of Numerical Methods and Fluids*, 71:119–134, 2013.

[29] J. O. Hinze. *turbulence*. McGraw-Hill, New York, USA, 1975.

[30] J. C. R. Hunt, A. A. Wray, and P. Moin. Eddies, stream, and convergence zones in turbulent flows. *Center for Turbulence Research Report CTR-S88*, pages 193–208, 1998.

[31] B. Iele and F. Palleschi. Boundary condition in the oscillating turbulent boundary layer for the simulation of wave breaking. *ACM International Conference Proceeding Series*, pages 115–121, 2020.

[32] B. Iele, F. Palleschi, G. Cannata, and F. Gallerano. A new turbulence model for breaking wave simulations. *Water*, 14:2050–2073, 2022.

[33] B. Iele, F. Palleschi, and F. Gallerano. Boundary conditions for the simulation of wave breaking. *WSEAS Transaction on Fluid Mechanics*, pages 1–13, 2020.

[34] C. R. Iribarren and M. Casto Nogales. Protection des ports. *Proceeedings XVII International Navigation Congress, Section II, Communication*, 4:31—-80, 1979.

[35] J. Jeong and F. Hussain. On the identification of a vortex. *Journal of Fluid Mechanics*, 285:69–94, 1995.

[36] G. Jiang and C. Shu. Efficient implementation of weighted eno schemes. *Journal of Computational Physics*, 126:202–228, 1996.

[37] A. B. Kennedy, Q. Chen, J. T. Kirby, and D. R. A. Boussinesq modelling of wave transforamtion, breaking and runup. i: 1d. *Journal of Waterway, Port, Coastal, and Ocean Engineering*, 126:39–47, 2000.

[38] A. N. Kolmogorov. Dissipation of energy in the locally isotropic turbulence. *Doklady Akademiia Nauk SSSR*, 32:19–21, 1941.

[39] A. N. Kolmogorov. The local structure of turbulence in incompressible viscous fluid for very large reynolds' numbers. *Doklady Akademiia Nauk SSSR*, 30:301–305, 1941.

[40] A. N. Kolmogorov. Equations of turbulent motion of a incompressible fluid. *Proceedings of the Izvestia Academy of Sciences USSR*, 6:299–303, 1942.

[41] B. E. Launder and B. I. Sharma. Application of the energy dissipation model of turbulence to the calculation of flow near a spinning disc. *Letters in Heat and Mass Transfer*, 1(2):131—-138, 1974.

[42] C. M. Lemos. A simple numerical technique for turbulent flows with free surfaces. *International Journal Numerical Methods and Fluids*, 15(2):127—-146, 1992.

[43] P. Lin and C. W. Li. A σ-coordinate three-dimensional numerical model for surface wave propagation. *International Journal of Numerical Methods and Fluids*, 38:1045–1068, 2002.

[44] P. Lin and C. W. Li. A σ-coordinate three-dimensional numerical model for surface wave propagation. *International Journal Numerical Methods and Fluids*, 38:1048—-1068, 2002.

[45] P. L. F. Liu and P. Lin. A numerical model for breaking waves: the volume of fluid method. *Research Report No. CACR-97-02. Journal of Fluid Mechanics*, 359:1–56, 1997.

[46] H. Luo and T. R. Bewley. On the contravariant form of the navier-stokes equations in time-dependent curvilinear coordinate system. *Journal of Computational Physics*, 199:355–375, 2004.

[47] G. Ma, F. Shi, and J. T. Kirby. Shock-capturing non-hydrostatic model for fully dispersive surface wave processes. *Ocean Modelling*, 43-44(9):22–35, 2012.

[48] S. Mayer and P. A. Madsen. Simulations of breaking waves in the surf zone using a navier-stokes sover. *Proceeding 25th International Conference of Coastal Engineering*, ASCE:928–941, 2000.

[49] F. R. Menter. Improved two-equation $k - \omega$ turbulence models for aerodynamic flows. *NASA TM-108854*, 1992c.

[50] S. Ogawa and T. A. Ishiguro. A method for computinf flow fields aruond moving bodies. *Journal of Fluid Mechanics*, 69:49–68, 1987.

[51] F. Palleschi. Simulazione tridimensionale di onde e correnti. Master's thesis, Sapienza University of Rome, May 2022.

[52] F. Palleschi and B. Iele. Gallerano, integral contravariant form of the navier-stokes equations. *WSEAS Transaction on Fluid Mechanics*, pages 1–13, 2019.

[53] F. Palleschi, B. Iele, and M. Tamburrino. Wave fields and nearshore currents in the coastal region opposite san mauro cilento (italy). *WSEAS Transaction on Fluid Mechanics*, pages 1–9, 2020.

[54] J. Peng, S. Liu, S. Li, K. Zhang, and Y. Shen. An efficient targheted eno scheme with local adaptive dissipation for compressible flow simulation. *Journal of Computational Physics*, 425:109902–109932, 2021.

[55] N. A. Philips. A coordinate system having special advantages for numerical forecasting. *Journal of the Atmospheric Sciences*, 14:184–185, 1957.

[56] L. Prandtl. *Über ein neues Formelsystem für die ausgebildete Turbulenz*. Nachrichten der Akademie der Wissenschaften zu Göttingen, Mathematisch-Physikalische Klasse, Gottinga, Germany, 1945.

[57] S. K. Robinson. Coherent motions in the turbulent boundary layer. *Annual Reviews Fluid Mechanics*, 23:601–639, 1991.

[58] W. Rodi. Experience with two-layer models combining the $k-\varepsilon$ model with a one-equation model near the wall. *AIAA, Aerospace Sciences Meeting, 29th*, 7-10:1—-13, 1991.

[59] C. G. Speziale, R. Abib, and E. C. Anderson. A critical evaluation of two-equation models for near wall turbulence. *AAIA Journal*, 30(2):324–353, 1990.

[60] M. J. F. Stive. Velocity and pressure field of a spilling breakers. *Proceedings of the 17th International Conference on Coastal Engineering*, pages 547–566, 1980.

[61] M. J. F. Stive. Two-dimensional breaking of waves on a beach;laboratory report. pt. 2. pressure field in waves shoaling and breaking on a plane beach. *In Report on Laboratory Investigation*, http://resolver.tudelft.nl/uuid:8042de7c-0a63-47ec-9d9e-bdcdc8d70276, 1983.

[62] T. Theodorsen. Mechanism of turbulence. *Proceedings of the 2nd Midwestern Conference on Fluid Mechanics*, pages 1–18, 1952.

[63] F. C. K. Ting and J. T. Kirby. Observation of undertow and turbulence in a laboratory surf zone. *Coastal Engineering*, 24:51–80, 1994.

[64] F. C. K. Ting and J. T. Kirby. Dynamics of surf-zone turbulence in a strong plunging breaker. *Coastal Engineering*, 24:177–204, 1995.

[65] F. C. K. Ting and K. J. T. 'dynamics of surf-zone turbulence in a spilling breaker. *Coastal Engineering*, 27:131–160, 1996.

[66] G. Tonelli and M. Petti. Shock-capturing boussinesq model for irregular wave propagation. *Coastal Engineering*, 64:8–19, 2012.

[67] E. Toro. *Shock-capturing methods for free-surface shallow flows*. Wiley, New York, USA, 2001.

[68] R. Weigel. A presentation of cnoidal wave theory for practical application. *Journal of Fluid Mechanics*, 7:273–286, 1960.

[69] Wikipedia. Breaking wave — wikipedia, l'enciclopedia libera, 2022. [Figure of breaker types].

[70] D. C. Wilcox. Reassessment of the scale determining equation for advanced turbulence model. *AAIA Journal*, 28(7):1194, 1988a.

[71] D. C. Wilcox. *Turbulence modeling for CFD*. DCW Industries, USA, 2006.

[72] V. Yakhot, S. Thangam, T. B. Gatski, S. A. Orszag, and S. C. G. Development of turbulence models for shear flows by a double expansion technique. *NASA Contractor Report 187611*, ICASE Report No. 91-65:1–28, 1991.

[73] Q. Zhao, S. Armfield, and K. Tanimoto. Numerical simulation of breaking waves by a multi-scale turbulence model. *Coastal Engineering*, 51:53—-80, 2004.

Appendix A

Appendix A: Rankine-Hugoniot condition

Rankine-Hugoniot condition is applicable to discontinuous solutions of hyperbolic conservation laws

$$\begin{cases} \mathbf{A}_t + \mathbf{F}(\mathbf{A})_x = 0 \\ \mathbf{A}(x,0) = \mathbf{A}_0(x) \end{cases} \tag{A.1}$$

where $\mathbf{A}$ is the vector of the unknown variables expressed by

$$\mathbf{A} = [a_1, a_2, ..., a_m]^T \tag{A.2}$$

and $\mathbf{F}(\mathbf{A})$ is the vector of the fluxes.

The integral form of a conservation equation (Eq. A.1) is given by

$$\frac{d}{dt}\int_{x_L}^{x_R} a(x,t)dx = f(a(x_L,t)) - f(a(x_R,t)) \tag{A.3}$$

Let be $a(x,t)$ one of the solutions of Eq. A.3 so that $a(x,t)$ and $f(a)$ and their derivatives are continuous except on the line $s = s(t)$. On this line $a(x,t)$ has a discontinuity. x_R and x_L are chosen on x-coordinate so that $x_L < s(t) < x_R$. The integral form of Eq. A.3 on a control volume $[x_L, x_R]$ is given by

$$\begin{aligned} f(a(x_L,t)) - f(a(x_R,t)) = \frac{d}{dt}\left[\int_{x_L}^{s(t)} a(x,t)dx + \int_{s(t)}^{x_R} a(x,t)dx\right] = \\ [a(s_L,t) - a(s_R,t)]S + \int_{x_L}^{s(t)} a(x,t)dx + \int_{s(t)}^{x_R} a(x,t)dx \end{aligned} \tag{A.4}$$

where $a(s_L, t)$ and $a(s_R, t)$ are the limits of $a(s(t), t)$ respectively for $x \to s(t)$ from left and right; $S = ds/dt$ is the speed by which the discontinuity travels[1]. The sum of the integrals on the right-hand side of Eq. A.4 is zero because a is limited.

$$\begin{gathered} f(a(x_L, t)) - f(a(x_R, t)) = [a(s_L, t) - a(s_R, t)]S \\ \Delta f = S\Delta a \end{gathered} \tag{A.5}$$

The expression that relates Δf and Δu to the discontinuity velocity S is called Rankine-Hugoniot condition. The solution of the partial differential equations (PDEs) can be determined both where the solution is regular and where the solution has a discontinuity through this condition.

[1] $\frac{d}{dy}\int_{x_1(y)}^{x_2(y)} f(x,y)dx = \int_{x_1(y)}^{x_2(y)} \frac{\partial f}{\partial y}dx + f(x_2,y)\frac{dx_2}{dy} - f(x_1,y)\frac{dx_1}{dy}$

Appendix B

Appendix B: Riemann Invariants

Riemann invariants are constant along the characteristic curves of a PDEs and are formulated to simplify the study and the solution of conservation equations.

By using the Jacobian matrix[1], any system of conservation law can be expressed in quasi-linear form. A system of quasi-linear hyperbolic PDEs can be expressed by

$$\mathbf{A}_t + \mathbf{F}(\mathbf{A})\mathbf{A}_x = \mathbf{0} \tag{B.1}$$

where $\mathbf{A}$ is the vector of the unknown conserved variables expressed by

$$\mathbf{A} = [a_1, a_2, ..., a_m]^T \tag{B.2}$$

Let be $\lambda_i(\mathbf{A})$ the characteristic field associated with a wave in which the eigenvalue is λ_i and $\mathbf{R}^{(1)}(\mathbf{A})$ is the corresponding right eigenvector

$$\mathbf{R}^{(i)} = [r_1^{(i)}, r_2^{(i)}, ..., r_m^{(i)}] \tag{B.3}$$

Eq. B.1 is simplified by using the components of the vector $\mathbf{R}^{(i)}$ trough the *Riemann invariants* that lead to the following $m-1$ ordinary differential equations

$$\frac{da_1}{r_1^{(i)}} = \frac{da_2}{r_2^{(i)}} = ... = \frac{da_m}{r_m^{(i)}} \tag{B.4}$$

Eqs. B.4 relate the variation of a quantity a_m to respective components of the

[1] A differential conservation law $\mathbf{A}_t + \mathbf{F}(\mathbf{A})_x = \mathbf{0}$ expressed in conserved variables can be expressed in quasi-linear form as follow $\mathbf{A}_t + \mathbf{G}(\mathbf{A})\mathbf{A}_x = \mathbf{0}$, where $\mathbf{G}(\mathbf{A}) = \partial\mathbf{F}/\partial\mathbf{A}$ is the Jacobian matrix corrispondig to the flux $\mathbf{F}(\mathbf{A})$.

right eigenvector that corresponds to a $\lambda_i(\mathbf{A}^{(i)})$ wave family.

Appendix C

Appendix C: Derivation of ω -equation

The equation for the dissipation rate can be obtained from the equation for the dissipation of turbulent kinetic energy.

Firstly the equations for the standard $k-\varepsilon$ model [41] should be presented

$$\frac{\partial k}{\partial t}+u_j\frac{\partial k}{\partial x_j}=\tau_{ij}\frac{\partial u_i}{\partial x_j}-\varepsilon+\frac{\partial}{\partial x_j}\left[\left(\nu+\frac{\nu_T}{\sigma_k}\right)\frac{\partial k}{\partial x_j}\right] \tag{C.1}$$

$$\frac{\partial \varepsilon}{\partial t}+u_j\frac{\partial \varepsilon}{\partial x_j}=C_{\varepsilon 1}\frac{\varepsilon}{k}\tau_{ij}\frac{\partial u_i}{\partial x_j}-C_{\varepsilon 2}\frac{\varepsilon^2}{k}+\frac{\partial}{\partial x_j}\left[\left(\nu+\frac{\nu_T}{\sigma_\varepsilon}\right)\frac{\partial \varepsilon}{\partial x_j}\right] \tag{C.2}$$

in which the closure relation are given by

$$\begin{gathered} C_{\varepsilon 1}=1.44 \quad C_{\varepsilon 2}=1.92 \quad C_\mu=0.09 \quad \sigma_k=1.0 \quad \sigma_\varepsilon=1.3 \\ \nu_T=C_\mu\frac{k^2}{\varepsilon} \end{gathered} \tag{C.3}$$

The dissipation of turbulent kinetic energy, $\varepsilon=C_\mu k\omega$, can be replaced in Eq. C.2

$$\begin{aligned} \frac{\partial (C_\mu k\omega)}{\partial t}+u_j\frac{\partial (C_\mu k\omega)}{\partial x_j}&=C_{\varepsilon 1}\frac{(C_\mu k\omega)}{k}\tau_{ij}\frac{\partial u_i}{\partial x_j}-C_{\varepsilon 2}\frac{(C_\mu k\omega)^2}{k} \\ &+\frac{\partial}{\partial x_j}\left[\left(\nu+\frac{\nu_T}{\sigma_\varepsilon}\right)\frac{\partial (C_\mu k\omega)}{\partial x_j}\right] \end{aligned} \tag{C.4}$$

By dividing Eq. C.4 by C_μ and re-writing the derivative, it is obtained the

following expression

$$\begin{aligned}\left(k\frac{\partial\omega}{\partial t}+\omega\frac{\partial k}{\partial t}\right)+u_jk\frac{\partial\omega}{\partial x_j}+u_j\omega\frac{\partial k}{\partial x_j}=C_{\varepsilon1}\frac{(k\omega)}{k}\tau_{ij}\frac{\partial u_i}{\partial x_j}\\ -C_{\varepsilon2}\frac{C_\mu(k\omega)^2}{k}+k\frac{\partial}{\partial x_j}\left[\left(\nu+\frac{\nu_T}{\sigma_\varepsilon}\right)\frac{\partial\omega}{\partial x_j}\right]+\left(\nu+\frac{\nu_T}{\sigma_\varepsilon}\right)\frac{\partial\omega}{\partial x_j}\frac{\partial k}{\partial x_j}\\ +\omega\frac{\partial}{\partial x_j}\left[\left(\nu+\frac{\nu_T}{\sigma_\varepsilon}\right)\frac{\partial k}{\partial x_j}\right]+\left(\nu+\frac{\nu_T}{\sigma_\varepsilon}\right)\frac{\partial\omega}{\partial x_j}\frac{\partial k}{\partial x_j}\end{aligned}\tag{C.5}$$

Eq. C.5 is divided by k

$$\begin{aligned}\left(\frac{\partial\omega}{\partial t}+\frac{\omega}{k}\frac{\partial k}{\partial t}\right)+u_j\frac{\partial\omega}{\partial x_j}+\frac{u_j\omega}{k}\frac{\partial k}{\partial x_j}=C_{\varepsilon1}\frac{\omega}{k}\tau_{ij}\frac{\partial u_i}{\partial x_j}\\ -C_{\varepsilon2}C_\mu\omega^2+\frac{2}{k}\left(\nu+\frac{\nu_T}{\sigma_\varepsilon}\right)\frac{\partial\omega}{\partial x_j}\frac{\partial k}{\partial x_j}\\ +\frac{\partial}{\partial x_j}\left[\left(\nu+\frac{\nu_T}{\sigma_\varepsilon}\right)\frac{\partial\omega}{\partial x_j}\right]+\frac{\omega}{k}\frac{\partial}{\partial x_j}\left[\left(\nu+\frac{\nu_T}{\sigma_\varepsilon}\right)\frac{\partial k}{\partial x_j}\right]\end{aligned}\tag{C.6}$$

Eq. C.1 is multiplied by ω/k

$$\frac{\omega}{k}\frac{\partial k}{\partial t}+u_j\frac{\omega}{k}\frac{\partial k}{\partial x_j}=\frac{\omega}{k}\tau_{ij}\frac{\partial u_i}{\partial x_j}-\frac{\omega}{k}\varepsilon+\frac{\omega}{k}\frac{\partial}{\partial x_j}\left[\left(\nu+\frac{\nu_T}{\sigma_k}\right)\frac{\partial k}{\partial x_j}\right]\tag{C.7}$$

Eq. C.7 is subtracted from C.6. The subtraction of each term is below

1. $\frac{\partial\omega}{\partial t}+\cancel{\frac{\omega}{k}\frac{\partial k}{\partial t}}+u_j\frac{\partial\omega}{\partial x_j}+\cancel{\frac{u_j\omega}{k}\frac{\partial k}{\partial x_j}}-\cancel{\frac{\omega}{k}\frac{\partial k}{\partial t}}-\cancel{\frac{\omega u_j}{k}\frac{\partial k}{\partial x_j}}$

2. $C_{\varepsilon1}\frac{\omega}{k}\tau_{ij}\frac{\partial u_i}{\partial x_j}-C_{\varepsilon2}C_\mu\omega^2-\frac{\omega}{k}\tau_{ij}\frac{\partial u_i}{\partial x_j}+\frac{\omega}{k}\varepsilon=$
   $\frac{\omega}{k}\tau_{ij}\frac{\partial u_i}{\partial x_j}(C_{1\varepsilon}-1)-C_{2\varepsilon}C_\mu\omega^2+C_\mu k\omega\frac{\omega}{k}=$
   $\frac{\omega}{k}\tau_{ij}\frac{\partial u_i}{\partial x_j}(C_{1\varepsilon}-1)-\omega^2(C_{2\varepsilon}C_\mu-C_\mu)$

3. $\frac{2}{k}\left(\nu+\frac{\nu_T}{\sigma_\varepsilon}\right)\frac{\partial\omega}{\partial x_j}\frac{\partial k}{\partial x_j}+\frac{\partial}{\partial x_j}\left[\left(\nu+\frac{\nu_T}{\sigma_\varepsilon}\right)\frac{\partial\omega}{\partial x_j}\right]+\frac{\omega}{k}\frac{\partial}{\partial x_j}\left[\left(\nu+\frac{\nu_T}{\sigma_\varepsilon}\right)\frac{\partial k}{\partial x_j}\right]$
   $-\frac{\omega}{k}\frac{\partial}{\partial x_j}\left[\left(\nu+\frac{\nu_T}{\sigma_k}\right)\frac{\partial k}{\partial x_j}\right]=$
   $\frac{2}{k}\left(\nu+\frac{\nu_T}{\sigma_\varepsilon}\right)\frac{\partial\omega}{\partial x_j}\frac{\partial k}{\partial x_j}+\frac{\partial}{\partial x_j}\left[\left(\nu+\frac{\nu_T}{\sigma_\varepsilon}\right)\frac{\partial\omega}{\partial x_j}\right]+\frac{\omega}{k}\frac{\partial}{\partial x_j}\left(\left(\frac{1}{\sigma_\varepsilon}+\frac{1}{\sigma_k}\right)\nu_T\frac{\partial k}{\partial x_j}\right)$ [1]

[1] $\frac{\omega}{k}\frac{\partial}{\partial x_j}\left[\left(\nu+\frac{\nu_T}{\sigma_\varepsilon}\right)\frac{\partial k}{\partial x_j}\right]-\frac{\omega}{k}\frac{\partial}{\partial x_j}\left[\left(\nu+\frac{\nu_T}{\sigma_k}\right)\frac{\partial k}{\partial x_j}\right]=\cancel{\frac{\omega}{k}\frac{\partial}{\partial x_j}\left(\nu\frac{\partial k}{\partial x_j}\right)}-\cancel{\frac{\omega}{k}\frac{\partial}{\partial x_j}\left(\nu\frac{\partial k}{\partial x_j}\right)}+$
$\frac{\omega}{k}\frac{\partial}{\partial x_j}\left(\left(\frac{\nu_T}{\sigma_\varepsilon}\right)\frac{\partial k}{\partial x_j}\right)-\frac{\omega}{k}\frac{\partial}{\partial x_j}\left(\left(\frac{\nu_T}{\sigma_k}\right)\frac{\partial k}{\partial x_j}\right)$

This three terms are getting together and the final ω-equation is obtained

$$\begin{aligned}\frac{\partial \omega}{\partial t}+u_j\frac{\partial \omega}{\partial x_j}&=(C_{1\varepsilon}-1)\frac{\omega}{k}\tau_{ij}\frac{\partial u_i}{\partial x_j}-(C_{2\varepsilon}-C_\mu)\omega^2\\ &+\frac{\partial}{\partial x_j}\left(\left(\nu+\frac{\nu_T}{\sigma_\varepsilon}\right)\frac{\partial \omega}{\partial x_j}\right)+\frac{2}{k}\left(\nu+\frac{\nu_T}{\sigma_\varepsilon}\right)\frac{\partial \omega}{\partial x_j}\frac{\partial k}{\partial x_j}\\ &+\frac{\omega}{k}\frac{\partial}{\partial x_j}\left(\left(\frac{1}{\sigma_\varepsilon}-\frac{1}{\sigma_k}\right)\nu_T\frac{\partial k}{\partial x_j}\right)\end{aligned} \tag{C.8}$$

The closure coefficients are the ones used for $k-\varepsilon$ model. The last term on the right hand side of Eq. C.8 is deleted for sake of simplicity. The forth term on the right hand side of Eq. C.8 is the cross diffusion term that some authors missed in several $k-\omega$ model, while Speziale et al [59], Menter [49] and Wilcox [71] introduced in their model.

Appendix D

Appendix D: Q-method

Robinson [57] states: *A vortex exists when instantaneous streamlines mapped onto a plane normal to the vortex core exhibit a roughly circular or spiral pattern, when viewed from a reference frame moving with the centre of the vortex core.*

The vortex identification criteria are based on point-wise (or local) analysis of the velocity gradient tensor. The local analysis for the identification of a vortex defines a function that can be evaluated point-by-point. According a criterion based on the point values, this function classifies each point as being inside or outside a vortex. One of the most popular criteria are: Q-method [30], λ_2-method [15] and Δ-method [17].

Q-method [30] is based on the local analysis of the velocity gradient. A vortex is identified as low region with positive second invariant of the velocity gradient ($Q > 0$). The second invariant, Q, is defined as

$$Q = \frac{((\nabla \cdot \vec{u})^2 - tr(\nabla \vec{u}^2)}{2} \tag{D.1}$$

where $tr(\quad)$ indicates a trace of a square matrix, ∇ is the nabla operator and $\vec{u}$ is the Cartesian velocity vector.

For an incompressible flow ($\nabla \cdot \vec{u} = 0$), the second in invariant is given by

$$Q = \frac{1}{2}(|\underline{\Omega}|^2 - |\underline{S}|) \tag{D.2}$$

where $\underline{\Omega}$ and $\underline{S}$ are, respectively, the antisymmetric (vorticity tensor) and symmetric (strain rate tensor) components of the velocity gradient $\nabla \vec{u}$; $|\underline{\Omega}| = tr[\underline{\Omega}\underline{\Omega}^t]^{1/2}$

and $|\underline{\Omega}| = tr[\underline{S}\underline{S}^t]^{1/2}$.

The symmetric and antisymmetric components of the velocity gradient are given by

$$\begin{aligned} \underline{\Omega} &= \frac{1}{2}(\nabla\vec{u} - (\nabla\vec{u})^t) \\ \underline{S} &= \frac{1}{2}(\nabla\vec{u} + (\nabla\vec{u})^t) \end{aligned} \tag{D.3}$$

Q is a local measure of the excess rotation rate relative to the strain rate, represents the local balance between shear strain rate and vorticity magnitude.

Considerate la vostra semenza:
fatti non foste a viver come bruti,
ma per seguir virtute e canoscenza.
(Inferno, Canto XXVI *Dante Alighieri*)

Benedetta Iele, Roma, 17 maggio 2023